# Development and implementation of automated interferometric microscope for study of MEMS inertial sensors

A Dissertation
Submitted to the Faculty
Of the

**Worcester Polytechnic Institute**

in partial fulfillment of the requirements for the
Degree of Doctor of Philosophy
in
Mechanical Engineering

by

_____
Ryan T. Marinis

April 7$^{th}$, 2009

Approved:

_____
Prof. Ryszard J. Pryputniewicz, Major Advisor

_____
Prof. Gretar Tryggvason, Member, Dissertation Committee

_____
Prof. John M. Sullivan, Member, Dissertation Committee

_____
Mr. David S. Willits, Honeywell, Minneapolis, MN
Member, Dissertation Committee

_____
Prof. Yiming Rong, Graduate Committee Representative

**ABSTRACT**

Microelectromechanical systems (MEMS) are quickly becoming ubiquitous in commercial and military applications. As the use of such devices increases their reliability becomes of great importance. Although there has been significant research in the areas of MEMS errors, there is a lack of work regarding long term reliability of packaged systems. Residual thermomechanical stresses might relax over time which affects physical distances within a package, ultimately influencing the performance of a device. One reason that there has not been sufficient work performed on the long-term effects on structures might be the lack of a tool capable of characterizing the effects.

MEMS devices have been measured for shape and its changes using interferometric techniques for some time now. Commercially available systems are able to make high resolution measurements, however they might lack loading options. To study aging effects on components a test might need to run continuously for days or weeks, with systematic operations performed throughout the process. Such a procedure is conducive to an automated data acquisition system. A system has been developed at WPI using a Twyman-Green interferometer and a custom software suite.

The abilities of this system are demonstrated through analysis performed on MEMS tuning fork gyroscope (TFG) sensors. Specifically, shape is recorded to investigate die bond relaxation as a function of time and thermal cycle. Also presented are measurements made using stroboscopic illumination on operating gyroscopes, in situ. The effect of temperature on the performance of the sensors is investigated using a customized precision rate table.

## ACKNOWLEDGMENTS

# TABLE OF CONTENTS

# LIST OF FIGURES

# LIST OF TABLES

# NOMENCLATURE

| | |
|---|---|
| $a_c$ | Coriolis acceleration |
| $A$ | constant coefficient of the 2nd order surface, cross sectional area |
| $A_{LPM}$ | area between left proof mass and substrate |
| $ASME$ | American Society of Mechanical Engineers |
| $B$ | $y$ coefficient of the 2nd order surface |
| $c$ | linear coefficient for PZT, speed of light |
| $C$ | $y^2$ coefficient of the 2nd order surface, capacitance |
| $c_0$ | speed of light |
| $CHSLT$ | Center for Holographic Studies and Laser micro-mechaTronics |
| $CMOS$ | complementary metal oxide semiconductor |
| $CTE$ | coefficient of thermal expansion |
| $d$ | quadratic coefficient for PZT |
| $d_{gap}$ | sense gap distance |
| $D$ | $x$ coefficient of the 2nd order surface |
| $DLP$ | digital light processor |
| $DMD$ | digital micromirror device |
| $E$ | $xy$ coefficient of the 2nd order surface, modulus of elasticity, EM wave amplitude |
| $E_0$ | real amplitude of an electromagnetic wave |
| $E_0^*$ | complex conjugate of real amplitude of an electromagnetic wave |
| $EM$ | electromagnetic wave |
| $f_{LPM}$ | the 2nd order equation for left proof mass |
| $f_{sub}$ | the 2nd order equation for substrate |
| $F$ | $x^2$ coefficient of the 2nd order surface, shear force on die bond |
| $F_c$ | Coriolis force |
| $FEA$ | finite element analysis |
| $FWHM$ | full width at half maximum |
| $GPS$ | global positioning system |
| $GUI$ | graphical user interface |
| $h$ | height of bump bond |
| $HDVSI$ | high definition vertical scanning interferometry |
| $He\text{-}Ne$ | Helium-Neon laser |
| $I$ | intensity |
| $I_n$ | image of phase step increment $n$ |
| $I_b$ | background intensity |
| $I_m$ | modulation intensity |
| $IMU$ | inertial measurement unit |
| $INS$ | inertial navigation system |
| $k$ | wave number, spring stiffness |
| $\mathbf{K}$ | sensitivity vector |
| $L$ | maximum distance between gold bump die bonds |
| $l_c$ | coherence length |

| | |
|---|---|
| $L_O$ | object arm length of an interferometer |
| $L_R$ | reference arm length of an interferometer |
| LED | light emitting diode |
| $m$ | mass of proof mass, slope, tilt of proof mass, total number of phase steps |
| MEMS | microelectromechanical system |
| $n$ | image phase step number |
| $nm$ | nanometer |
| OEH | optoelectronic holography |
| OELIM | optoelectronic laser interferometric microscope |
| $p_1$ | reference point on proof mass analysis |
| $p_2$ | reference point on substrate analysis |
| $P$ | probability |
| PC | host computer |
| PID | proportional, integral, derivative closed loop control settings |
| $ppm$ | part per million |
| PSI | phase shifting interferometry |
| PV | peak to valley amplitude |
| PZT | piezoelectric transducer |
| $Q$ | quality factor |
| $r^2$ | coefficient of determination |
| RMS | root mean square |
| $S$ | sum of quadratic errors |
| SEM | scanning electron microscopy |
| SNL | Sandia National Laboratories |
| SOI | silicon on insulator |
| $t$ | time, test statistic for t-test |
| $T$ | temperature, absolute temperature |
| TEC | thermo electric cooler |
| TFG | tuning fork gyroscope |
| TPMI | temporal phase measurement interferometer |
| USP | upper sense plate |
| $v$ | frequency of light wave, linear velocity |
| VI | virtual instrument |
| VSI | vertical scanning interferometry |
| $w$ | thickness of MEMS chip |
| $x_1$ | left edge of proof mass |
| $x_2$ | right edge of proof mass |
| $\dot{y}$ | the 1$^{\text{st}}$ derivative of $y$ |
| $\ddot{y}$ | the 2$^{\text{nd}}$ derivative of $y$ |
| $Z$ | the 2$^{\text{nd}}$ order surface fit to substrate |
| $z$ | position in space of propagating EM wave |
| ZRO | zero rate output |
| $\alpha$ | coefficient of thermal expansion |

| | |
|---|---|
| $\delta\tau$ | coherence time |
| $\Delta d_{gap}$ | average gap distance change |
| $\Delta L$ | path length difference |
| $\Delta x$ | shear displacement of die bond, magnitude of stroke of TFG proof mass |
| $\Delta\lambda$ | wavelength bandwidth |
| $\Delta\phi$ | phase difference, phase step |
| $\epsilon_0$ | permittivity of free space |
| $\epsilon_r$ | relative permittivity |
| $\kappa$ | curvature along a trace |
| $\kappa_x$ | principal curvature along x trace |
| $\kappa_y$ | principal curvature along y trace |
| $\lambda$ | wavelength |
| $\mu m$ | micrometer |
| $\rho$ | Gaussian curvature of a surface |
| $\phi$ | phase term |
| $\phi_{uw}$ | unwrapped phase |
| $\omega$ | angular frequency |
| $\omega_d$ | drive frequency |
| $\Omega$ | scaled shape, fringe-locus function |
| $\Omega_I$ | rotational input to gyroscope |
| $\%\Delta\rho$ | percent change in Gaussian curvature |

## OBJECTIVES

In all mechanical systems the use of different materials and assembly procedures causes stress in the components.  As the size scale for systems has decreased, so had the magnitude of these stresses.  One particular example is in microelectronics.  Using MEMS technology it is now possible to fabricate completely functional mechanical devices with a length scale of 10's of micrometers.  The deformations present in such devices might be large, relative to the device itself, yet extremely small when compared to conventional devices.  As size decreases, accurately measuring fundamental properties of these devices, such as size or shape as stress changes due to fundamental loads, becomes difficult.  Adding complexity is measuring changes in the shape, or strains.  Methods such as strain gauges are not compatible due to size constraints, and any physical contact with the devices might cause deformations larger than those that are to be measured.

Non-invasive measurements are extremely advantageous for measurements of mechanical strain on this scale.  The strain results from many different loads, such as thermal loading, force input, or residual deformation.  Using optical techniques it is possible to accurately measure shapes and deformations while not disturbing the object under investigation.  Commercially available systems use interferometric techniques to make extremely accurate shape or deformation measurements, however these systems are not always sufficient.  In particular, investigation into thermal loading, let alone thermal cycling, is not always possible.

A system is to be developed for use in the Center for Holographic Studies and Laser micro-mechaTronics (CHSLT) at Worcester Polytechnic Institute (WPI) which uses interferometric principles, along with custom mechanical and software design, to meet many of the requirements for the accurate characterization of MEMS devices. The custom system is to be capable of shape measurements over a temperature range of 0-100ºC, and is to possess scripting capabilities to autonomously perform thermal cycling and data acquisition. All components of the measurement system are to be controlled by a host PC, allowing for remote operation or monitoring of a long term script. In addition to long-term experiments, the scripting capabilities will be extended to dynamic measurements. A strobe illumination is used to make measurements throughout a motion cycle at various phase positions to investigate dynamic systems.

The capabilities of this new tool will be demonstrated through analysis of tuning fork gyroscope (TFG) components. Inertial sensors are one of the most commercially successful devices, and are currently striving for increased performance while reducing size to produce a complete inertial navigation system (INS). The analysis will include representative results on the direct measurement of die curvature as a result of the packaging process. The effects of temperature on this deformation will be presented through shape measurement as well as laboratory testing on a rate table. Further investigation of this effect will be performed by examination of a functioning gyroscope, in situ, directly measuring a quadrature error. The effects of temperature, and perhaps die curvature, on quadrature error will be presented and discussed.

# 1. INTRODUCTION

In the years since Richard Feynman's famous talk, *There's plenty of room at the bottom*, made to the American Physical Society in 1959 (Feynman, 1992), there has been an underlying theme of the miniaturization in engineering. In this talk Feynman discussed the current size limit for fabrication of components, as well as the theoretical limits for size reduction and the implications the small scale might have on technology. The effect of this talk is still seen today by miniaturization of mechanical components and sensors until they are fabricated on silicon wafers in a similar fashion to integrated circuits. These components, commonly referred to as microelectronics, or MEMS are the basis for many current technologies, completely transparent to the end user. Some such devices are the accelerometers which deploy airbags on impact in an automobile collision, the inertial sensors that detect/monitor the motion of video game remote controls, or an array of micro mirrors that provide high definition television.

With the ability to fabricate devices on a small scale comes the need for tools to characterize the components. Often the mechanical operation of the component is not directly measured; rather the electrical signals out of the devices are monitored. The size of components may be measured using scanning electron microscopy (SEM) or other similar methods. The three-dimensional shape may be measured by using an interferometric microscope, employing interference of light waves to make high accuracy shape measurements. Deformations caused by mechanical loading, actuation, packaging, or other means, may be determined experimentally using such techniques. The results are obtained by comparing measurements made in the initial and deformed states.

The following sections in this chapter briefly present the concepts of MEMS devices and interferometry, while greater detail on each topic is presented in subsequent chapters.

## 1.1. MEMS devices

Microelectromechanical devices are fabricated in various ways, although most common is using photolithographic techniques with silicon wafers, also referred to as micromachining. Batch processing enables a large number of components to be produced at a relatively low cost. Photosensitive materials are used to mask off regions of a substrate, which are then etched to produce mechanical components. Structural layers are added by growing or depositing conformal coatings of different materials. Layers are processed in subsequent steps to obtain a true multi-level device. The in-plane resolution of the micromachining process is dictated by the diffraction limit of the light used while exposing the masks. By implementing deep ultraviolet wavelengths features on the order of a single micrometer (µm) are possible. Examples of MEMS devices, as produced at Sandia National Laboratories (SNL), are shown in Fig. 1.
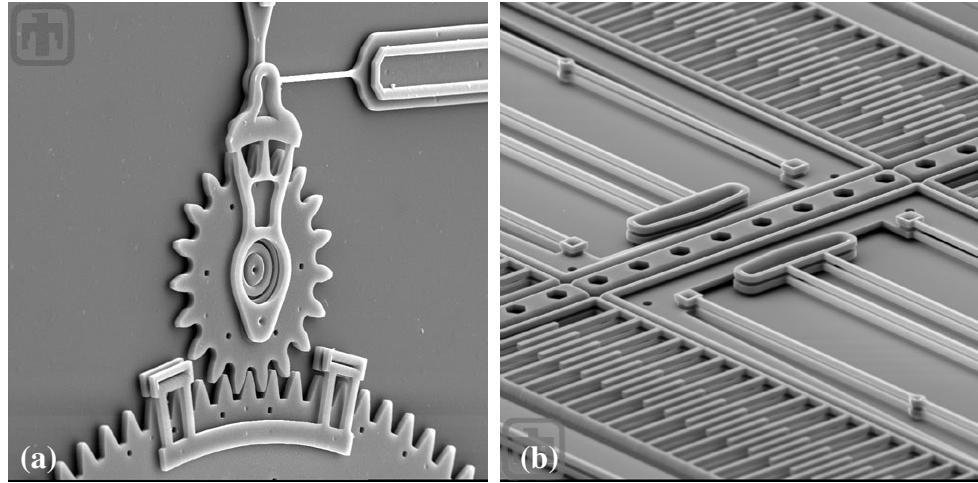
Fig. 1. MEMS devices from SNL: (a) meshed gears, (b) electrostatic comb drive microengine.

Sandia has optimized a fabrication processing using five structural layers to build complex MEMS components, allowing for the mechanical systems such as the meshed gears, with a diameter of approximately 20 µm, shown in Fig. 1(a). Scaling principles lead to advantages associated with miniaturization, for example, as the length scale decreases body (inertial) forces decrease to the third power. This allows gear systems to operate at speeds in excess of 1,000,000 revolutions per minute.

Extremely complex devices may be reproduced rapidly using MEMS technology, one example being the Texas Instruments digital micromirror device (DMD) which is a critical component to many high definition displays and projectors, Fig. 2. A large array of independently controlled mirrors is fabricated, with each mirror displaying a single pixel. The pixels are controlled by rapidly rocking the mirrors between an on and off positions.
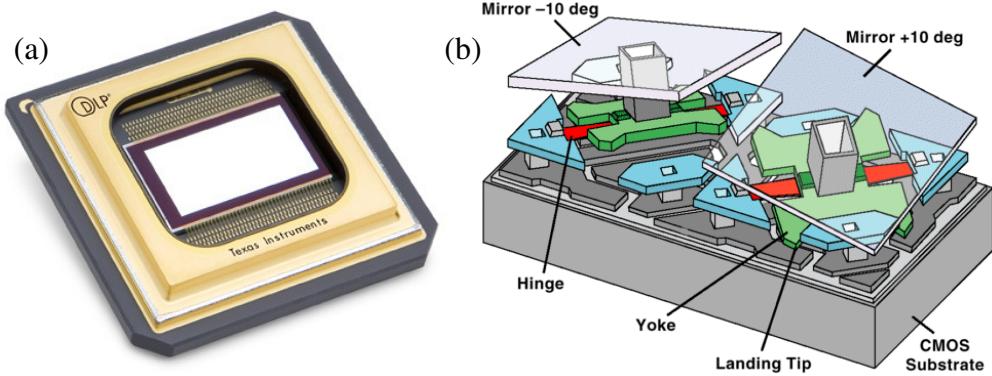
Fig. 2. Texas Instruments DMD used for the digital light processor (DLP): (a) packaged MEMS chip, (b) schematic of two pixels.

The degrees of freedom, when considering each pixel motion to be a separate degree, makes this display microchip one of the most complex mechanical devices currently produced. In 2008 the American Society of Mechanical Engineers (ASME) recognized the DMD as a historical mechanical engineering landmark, the first such landmark for a MEMS based concept.

Perhaps the strongest market to date for MEMS devices however is in sensing (Marinis, 2007). Due to the small size and low power requirements MEMS sensors may be used more generously than other, macro size, sensors. Also, the small feature size enables a very accurate sensor. For example, a hydrogen sensor cantilevers are coated with Palladium-Nickel alloy, which absorbers $H_2$. The absorption of the atoms increases the resistance of the system, allowing for the sensing of the combustible gas (Allen, 2005).

Inertial forces are commonly measured with MEMS sensors. One example of an inertial sensor is an accelerometer, which consists of a proof mass suspended by a compliant spring structure. When subjected to acceleration, differential motion between

the reference frame and the supported mass occurs, as described by Newton's second law. The differential motion is detected by capacitive means, which allow for the electrical sensing of a mechanical behavior, to determine the magnitude of the acceleration. Accelerometers of this type are commonplace in the automotive industry where sensing a sudden deceleration, such as in an accident, deploys airbags. An example of a two-axis accelerometer manufactured by Analog Devices is shown in Fig. 3.
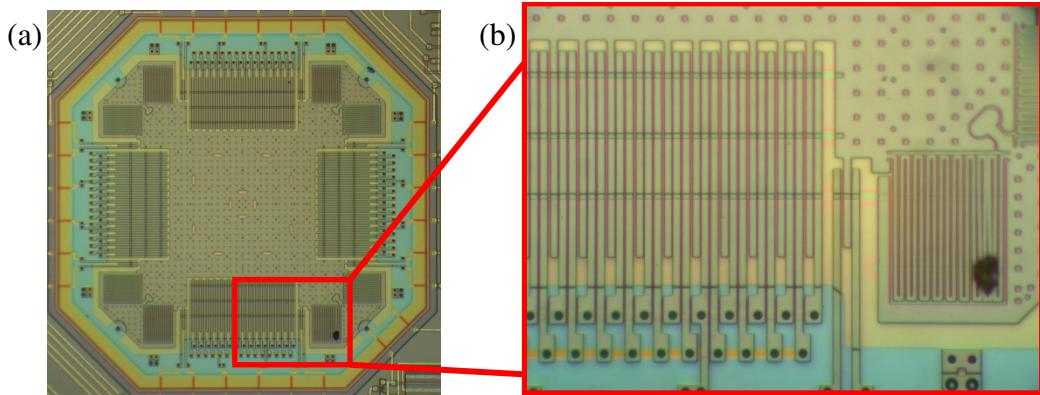


Fig. 3. Analog Devices ADXL-202 two-axis accelerometer: (a) overall MEMS structure, (b) capacitive combs and folded spring.

The folded springs that support the center proof mass allow for in-plane motion of the MEMS. The tolerances for the mass of the proof mass and the spring stiffness are small, resulting in a dynamic system with well known properties. There are fingers protruding off each edge of the proof mass, forming a capacitor with the fingers that are fixed on the substrate. An in-plane acceleration causes a force which displaces the proof mass. The amount of the displacement is measured by the change in the gap distance

separating the capacitor fingers.  The measured proof mass displacement, along with the

spring stiffness, is used for the calculation of the input acceleration.

Another form of inertial sensing is the gyroscope.  A tuning fork gyroscope (TFG)

uses a Coriolis principle to detect rotational rates.  Sensors such as these are also found in

the automotive industry, for functions such as stability control and anti-rollover systems.

An example of a TFG is shown in Fig. 4.
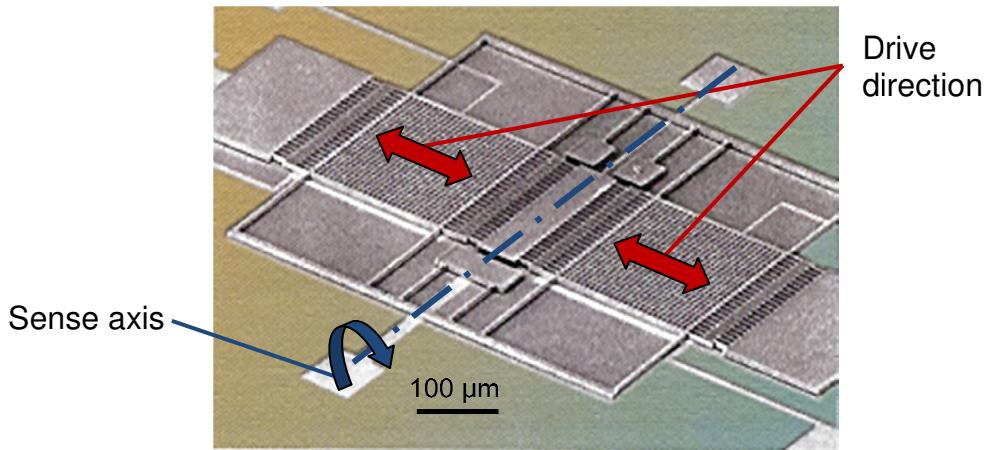


Fig. 4.  MEMS tuning fork gyroscope.

The two proof masses, supported by spring flexures, are excited by electrostatic

comb drives on the outer edge to excite the masses in-plane, in opposite directions.  Upon

the introduction of a rotation about the sense axis, a Coriolis effect causes the proof

masses to move in a non-planar motion.  A capacitor, formed by the bottom surface of the

proof mass and the substrate below the gyroscope, measures any changes in the gap

distance.  The capacitance, modulated by drive frequency, contains information on rate at

which the sensor is rotating.  Details of TFG operation are presented in Chapter 5 of this

dissertation.

By combining three accelerometers (one for each axis $x$, $y$, and $z$) along with three gyroscopes (roll, pitch, and yaw) it is possible to track all the motions of a single system, creating an inertial navigation system (INS). Although theoretically possible, an INS is not yet practical when compared to industry standards such as global positioning systems (GPS), or when comparing to traditional, non MEMS, sensors, such as ring laser gyroscopes.

There are a number of factors that limit performance (Woodman, 2007), however there has been little investigation into a mechanical error due to substrate deformations which might be introduced during the packaging process. In precision applications, where a high vacuum environment is required, the die attachment is performed by gold thermocompression bonding or brazing with AuSn. In both die attachment methods the system (comprising the package and sensor) is heated to a temperature in excess of 300ºC for bonding, and then cooled to ambient conditions. The differences in coefficients of thermal expansion (CTE) result in residual stresses, causing a curvature in the die (Marinis et al., 2006). This curvature is observed on the chip substrate, which acts as the bottom plate of the capacitor when measuring sense gap distance, leading toward the determination of rotational rate. The curvature is not constant with temperature, where the stress from the CTE difference changes, or time, where die bond relaxation might occur. In order to improve the design of components and minimize the effects of substrate curvature a tool is required to characterize topography of the MEMS.

## 1.2. Interferometry

As the size of components decreases, new methods of characterizing the end result must be developed. Any physical contact with a MEMS itself might damage the device, creating a need for non-contact, non-invasive measurement techniques, such as interferometric microscopy. Sizes of objects may be measured using scanning electron or traditional microscopes, however shape and strain are not as easily obtained. One method which has been demonstrated to work well on the shape and deformation measurements on MEMS devices is interferometry.

The basic concepts of an interferometer are described with a Michelson configuration, schematically shown in Fig. 5. A single light source, in this case a laser, is split such that a portion of the light travels to the fixed mirror, while the remaining light travels to a movable mirror. The difference in the paths traveled ($L_O$ and $L_R$) affects relative phase of the object and reference beam. Once recombined in the beam splitter the two light beams interfere. The resulting intensity is dependent on not only the light source intensity, but also on the path length difference.
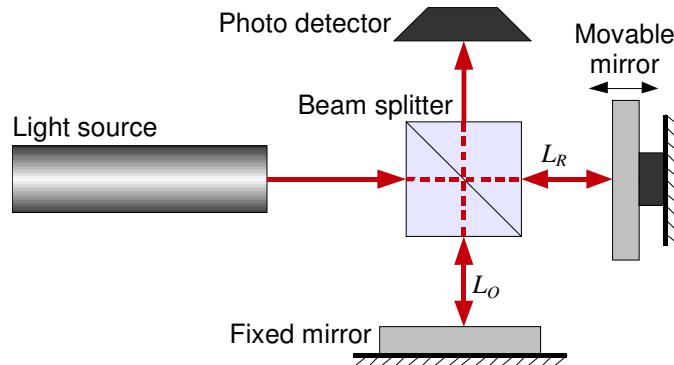


Fig. 5. Schematic representation of a Michelson interferometer.

The interference might be in varying degrees of constructive or destructive states. The degree of the interference is based on the relative phase of the reference and object beams when superimposed on one another. The intensity of the light observed by the photo detector can be adjusted by slightly moving the reference mirror (i.e., the moveable mirror). If the photo detector is replaced by a camera, acting as an array of photo detectors, and the light source is expended to view a finite area, full field shape can be measured. Each pixel will possess an intensity that is related to shape, producing a fringe pattern on the object, Fig. 6. The fringes in this case represent shape, normal with respect to the viewing plane, similar to contour lines on a topographical map. The magnitude of each fringe (i.e., change in elevation) is half the wavelength used in the interferometer, for a retro reflective configuration such as the Michelson interferometer shown in Fig. 5.
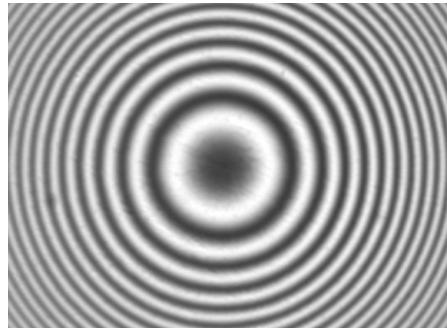


Fig. 6. Fringe pattern produced by a concave mirror.

The maximum difference between $L_O$ and $L_R$ for which interference is able to occur is known as the coherence length. This length is inversely related to the frequency bandwidth of the illumination source. As the path length mismatch increases, the fringe contrast decreases until a point at which no fringes are observed.

There are many methods for recording quantitative information from interferometry, one of which is phase shifting interferometry (PSI). To extract information by using a PSI system a small number of images (generally between three and five) are recorded with the path length of the reference mirror adjusted a known amount between each recording. The details of this process are described in detail in Chapter 2. This method of interferometric measurement is extremely accurate, with achievable accuracy on the order of $\lambda/1000$, where $\lambda$ is the wavelength of the light (Schwider et al., 1983).

An alternative method for data recording that has been recently become more prominent in the field is that of vertical scanning interferometry (VSI) (Harasaki et al., 2000). This method incorporates a short coherence length illumination such as a white light. With a broadband source, fringes are only visible when the path length difference between the object and reference is less than a few micrometers (Klempner et al., 2006). Image frames are recorded while scanning one arm (either the reference or object path) of the interferometer. Post processing is performed to find the scan position at which the fringe contrast (modulation) is a maximum. A sample trace of the modulation of a single pixel while scanning the reference mirror is shown in Fig. 7, where (a) represents the trace with monochromatic ($\lambda = 640$ nm) illumination while (b) represents a halogen white light illumination. The peak of the envelope of a trace such as these determines the scan position at which the two arms of the interferometer are matched to within the resolution of the measurement. This process is repeated for each pixel to obtain a full field of view shape.
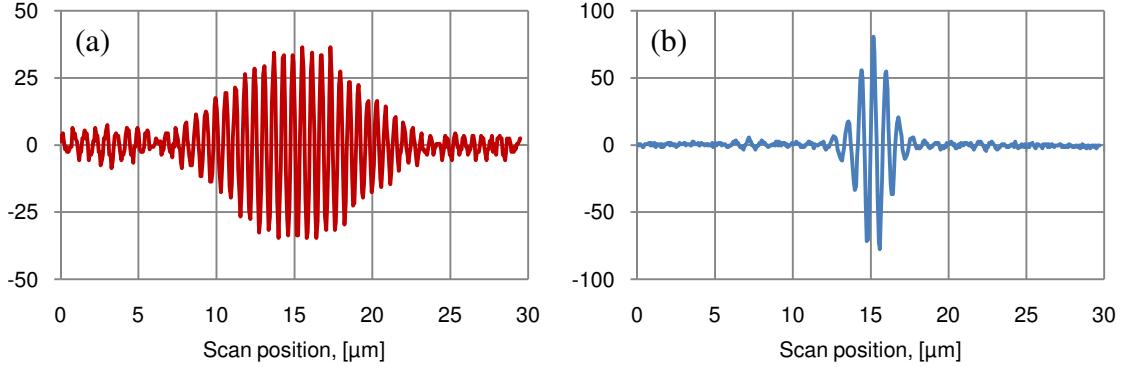
Fig. 7. Modulation of a single pixel in VSI: (a) monochromatic, (b) broadband source.

The resolution of VSI is less than that of PSI, however this technique is able to measure steps greater than $\lambda/2$. The step height limitation is dictated by the maximum length of the scan, while maintaining accuracy close to that of PSI. The measurement time is significantly longer for VSI, due to the constant image recording during an image scan. The duration of a recording is dependent on the scan length and image size.

The optoelectronic laser interferometric microscope (OELIM) developed for this dissertation implements the PSI technique. The shorter data acquisition time, along with higher accuracy, outweigh the advantage of the VSI, namely the ability to measure large steps. Most commercially available measurement systems currently incorporate the VSI technique. These systems are quite capable for many metrology applications, however may not be able to perform several of the measurements required for the analysis and development of inertial sensors.

### 1.3. Current industry standards

Commercially available interferometric measurement systems are available by several companies, including Veeco, Zygo, and Polytech, among others. Each of these systems functions primarily in a VSI mode. The experimental setup for VSI and PSI is identical. A recent trend has been the hybridization of the two technologies, demonstrated in the high-definition vertical scanning interferometry (HDVSI) by Veeco. The systems produced by Veeco and Zygo are microscope based, utilizing interferometers which have been built within microscope objectives, similar to those shown in Fig. 8.



Fig. 8. Interferometric microscope objectives.

The low magnification objectives (2.5x and 5x) are a Michelson configuration, while the higher magnification objectives (10x, 20x, and 50x) are Mirau configuration.

The objectives are mounted onto scanning microscope, allowing for scan lengths of tens of micrometers.

There are limitations to the measurements capable with the microscope based systems. The working distance under the objective is less than 10 mm for standard objectives, and 22 mm for long working distance objectives, which makes imaging through a window into an environmental chamber difficult. Furthermore, when placing a glass (such as a chamber window, or package lid) in the object path of an interferometer a compensation glass of the same material and thickness is required in the reference path to maintain modulation. The Michelson objectives have the ability to place a thin compensation glass in the reference path (on the order of 2 mm) however the Mirau objectives cannot accept such a glass. The thin compensation in the Michelson may be sufficient for a glass package lid, but will not be able to also compensate for a chamber window, which might be 12.5 mm thick.

Also, no commercial system is available with thermal loading capabilities. The challenges associated with convective instabilities during data acquisition, along with difficulties in imaging components inside a chamber, prevent thermal loading modules directly from the manufacturer of these systems at this time. It is possible to customize the systems by utilizing a thermo electric cooler (TEC) as a heating element under the microscope, however with no chamber to limit convective currents at elevated temperature significant noise is added to the measurements.

The interferometer developed for this work uses a telescope lens to obtain high magnification while maintaining a working distance of several inches. This allows for

the interferometer to be built below imaging optics, rather than contained within them. Environmental chambers are possible by placing compensation windows in the reference path. The implementation of thermal loading within a chamber has been performed, at WPI, for some time now, however all such systems relied on manual operation. The new system has been developed with a software interface which allows for creation and execution of scripts which consist of thermal cycling and data acquisition; the system developed during this dissertation is capable to operate autonomously for days, or even weeks at a time.

A complete description of the developed interferometer, including description of pertinent hardware components and an introduction to the software environment, are presented in this dissertation. The capabilities are demonstrated through representative investigation into MEMS components. These results show behaviors of the MEMS systems which are not possible to monitor without the OELIM system developed herein.

## 2. INTERFEROMETRIC METHODOLOGY

Interferometric measurements are possible due to the wave nature of light. By comparing the phase differences between a contoured object and a known (flat) shape, it is possible to make measurements that have a high precision and accuracy (<1 nm) in the direction normal to the viewing plane. In-plane resolution is limited, by the diffraction of light, to approximately 300 nm, for the visible spectrum. The shape variations, and deformations, of MEMS components is often less than 1 µm. The interferometric technique is well suited to the measurement of MEMS due to the ability to accurately characterize shape and deformation on this size scale.

Using interferometric techniques it is possible to measure absolute and relative shapes or curvatures. This ability is valuable for characterizing the mechanical behavior of MEMS devices, specifically when concerned with stresses induced during the packaging process. A mathematical description of an electromagnetic wave is introduced to develop the equations of interferometry. Once a fundamental understanding of light is obtained further concepts, such as requirements and quantitative analysis, are discussed.

### 2.1. Electromagnetic waves

The real amplitude of an electromagnetic (EM) wave, propagating in the $z$ direction is described mathematically as a harmonic wave by the equation

$$E(z, t) = E_0 \cos\left(\frac{2\pi z}{\lambda} - 2\pi v t\right) \tag{1}$$

where $E_0$ is the real amplitude, $\lambda$ is the wavelength, $v$ is the frequency, $z$ is the position in space, and $t$ is the time. These parameters are labeled on the sinusoidal wave shown in Fig. 9.
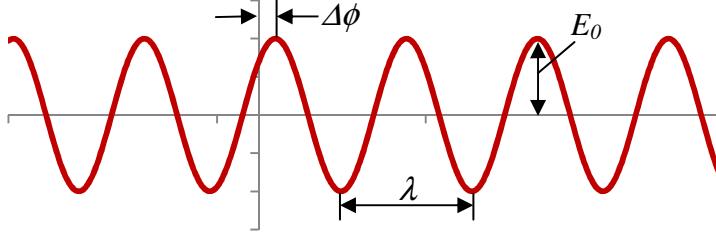


Fig. 9.  Graphical depiction of a harmonic wave.

In Eq. 1 we can substitute the wave number, $k$, and the angular frequency, $\omega$, defined as

$$k = \frac{2\pi}{\lambda}, \text{ and} \tag{2}$$

$$\omega = 2\pi v . \tag{3}$$

When Eqs 2 and 3 are combined with Eq. 1,

$$E(z, t) = E_0 \cos(kz - \omega t) \tag{4}$$

is obtained.  In general, we consider the entire argument of the cosine function as a single phase term, $\phi$.  Thus we are able to rewrite Eq. 4 as

$$E(z, t) = E_0 \cos(\phi) . \tag{5}$$

With a mathematical model of an EM wave it is possible to examine the superposition of two waves.  During amplitude division interferometry a light wave is split, with half the amplitude traveling to the reference mirror and the remaining part

illuminating the object. The light is often divided using a beam splitter. The same beam splitter combines the light after reflecting back from the object and reference mirrors. When the waves are combined there might be a phase difference between them caused by the independent path lengths. This phase difference causes some degree of interference between the added EM waves. It should be noted that $E_0$ is not directly measured, rather the intensity, $I$, is the property recorded by a photo detector or camera. Intensity is proportional to the square of the EM wave amplitude, $E$. The derivation of the interference equation is outlined in Appendix A, resulting in the observed intensity of two superimposed light waves, with a phase difference $\Delta\phi$ between them. Based on Eq. A-17

$$I = I_b + I_m \cos(\phi + \Delta\phi) \tag{6}$$

is obtained, where $I$ is the intensity measured by a detector, or camera at each pixel, $I_b$ is the background intensity, and $I_m$ is the modulation intensity. Graphical representations of states near complete destructive and constructive interference are shown in Figs. 10 (a) and 10 (b), respectively.
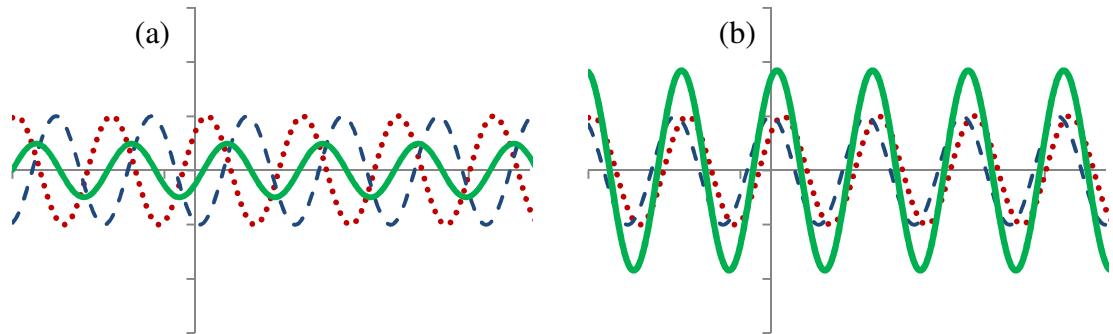


Fig. 10. Superposition of light waves: (a) destructive interference, (b) constructive interference, where dotted and dashed lines represent two interfering waves and solid line displays a result of interference.

## 2.2. Basic configuration

A relatively simple interferometer is ideal for the determination of shape or deformation of MEMS components. Such a configuration of the interferometer is introduced in the following sections along with details on the extraction of quantitative data.

### 2.2.1. Michelson interferometer

The fundamental configuration of an amplitude division interferometer is the Michelson interferometer, which has been introduced in Fig. 5 (Gåsvik, 2002). Although currently the most common optical interferometer, this configuration was initially assembled by Albert Michelson and Edward Morely to prove the non-existence of luminous either in their 1887 experiment.

A light beam, typically from a laser, is split by a beam splitter and sent to two mirrors: one fixed and one moveable. After reflecting off the mirrors the light is recombined in the same beam splitter. The superposition of the light that has been reflected off the two mirrors causes either constructive or destructive interference. The intensity, which contains the interference information, is observed by a photo detector.

The path length difference, $\Delta L$, is described as

$$\Delta L = 2|L_O - L_R|,$$ (7)

where $L_O$ and $L_R$ are the distances from the beam splitter to the fixed mirror and reference mirror, respectively. The factor of two is to account for light traveling to and from the

mirrors.  To relate the path length difference to the wave equation we require the wave

number, $k$, defined by Eq. 2.

The phase difference, in terms of physical values, is obtained by combining Eqs 2

and 7,

$$\Delta\phi = 2k|L_0 - L_R| \, . \tag{8}$$

Based on Eq. 8 it is shown that to achieve a $\Delta\phi$ of $2\pi$ (one fringe) that a path length

difference of $\lambda/2$ is required, confirming that one fringe of an interferogram corresponds

to elevation change of half the wavelength.  By precisely positioning the movable mirror

it is possible to alter the intensity observed by the photo detector.

### 2.2.2.  Twyman-Green interferometer

The Michelson interferometer has been based on a single point, with a single

detector.  The illumination is expanded to cover a finite area, with an array of detectors

used.  Expansion of the Michelson interferometer results in the Twyman-Green

configuration, Fig. 11.
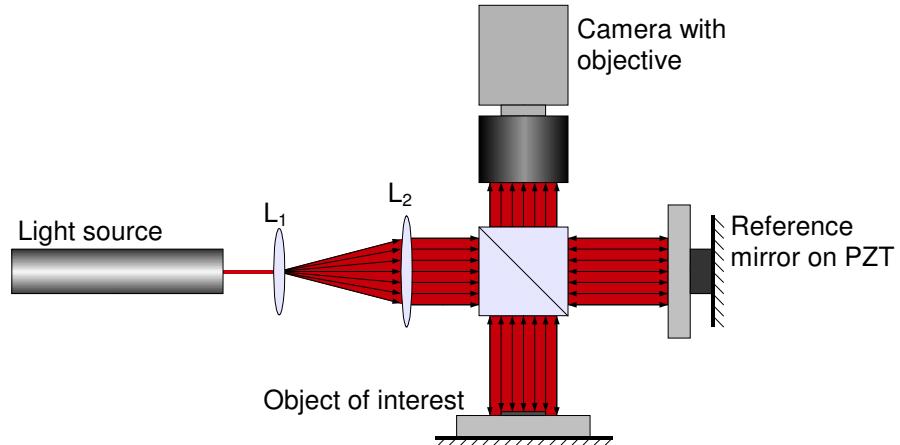
Fig. 11.  Schematic of Twyman-Green interferometer configuration.

A series of lenses are incorporated to expand, and then collimate, the illumination. A single photo detector is replaced with a camera, functioning as an array of photo detectors. A full surface of an object may now be imaged at once. If the surface of interest is continuous, there will be gradual changes in the intensity from pixel to pixel, resulting in fringes overlaying the object, as shown in Fig. 6. At this point directionality is ambiguous. The fringes represent shape normal to the viewing plane, but it is unknown if the direction is into, or out of, the plane. Quantitative analysis is performed by phase stepping the reference arm of the interferometer with a piezoelectric transducer (PZT). An objective is used on the camera to focus the object of interest, in this case the MEMS component.

## 2.3. Interference requirements

To extract quantitative information out of interferometric measurements several considerations are made. Primarily, the light source itself must be coherent for interference to occur. Secondly, phase stepping is performed, leading to quantitative analysis which may be completed in a variety of ways. Finally, environmental conditions should be controlled, with error sources minimized.

### 2.3.1. Coherence

A fundamental requirement for interference of light waves is the coherence of the source (Kuhn, 1998). A monochromatic light source, such as a laser, is often thought to

be emitting all photons at an identical frequency. This is not always the case, as demonstrated by the spectral plot of a red light emitting diode (LED), Fig. 12. This is a typical spectral output provided by LED vendors which is critical for selection of an illumination source.
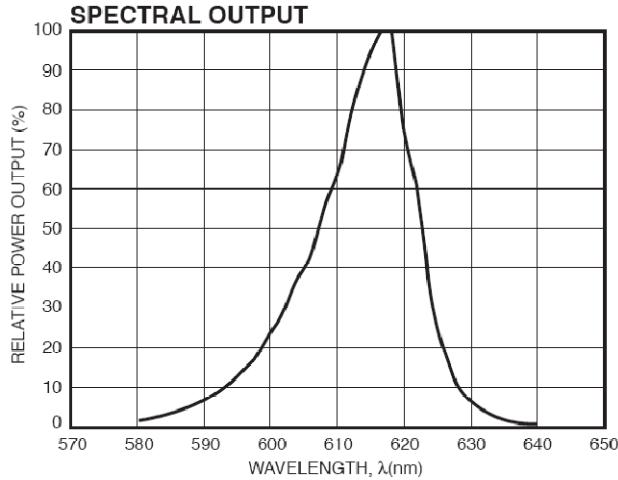


Fig. 12. Spectral output of Opto-Diode OD-620L LED (Opto Diode, 2008).

The frequency and the wavelength are related through the speed of light $c_0$,

$$\lambda = \frac{c_0}{v} ,$$  (9)

where $v$ is the frequency of the light source. It can be assumed that the incoherence of a light source is due to the lack of perfect monochromicity. The monochromicity may be modeled as a function of wavelength bandwidth, $\Delta\lambda$ (Kuhn, 1998),

$$\Delta v = v_1 - v_2 = \frac{c_0}{\lambda_1} - \frac{c_0}{\lambda_2} = c_0 \left(\frac{\lambda_2 - \lambda_1}{\lambda_2 \lambda_1}\right) \approx c_0 \left(\frac{\Delta\lambda}{\lambda^2}\right) .$$  (10)

We further examine the coherence by investigating the amount of time required for different oscillations to become out of phase by one cycle; approximately $1/\Delta v$. This time is generally referred to as the coherence time, $\delta\tau$.

A practical parameter for determining the quality of interference, or for consideration while selecting a light source, is the coherence length, $l_c$, which is the maximum mismatch between the reference and object paths of an interferometer for which modulation is still observed. Based on the assumption that coherence will not occur after the oscillations are out of phase by one cycle, we see that

$$l_c = \frac{c_o}{\Delta\nu} .$$ (11)

When combined with Eq. 10 we obtain

$$l_c = c_0 \cdot \left[\frac{c_o \Delta\lambda}{\lambda^2}\right]^{-1} = \frac{\lambda^2}{\Delta\lambda} ,$$ (12)

which provides the coherence length as a function of $\lambda$, and allows for determination of $l_c$ based solely on spectral output plots such as that shown in Fig. 12.

In order to calculate $l_c$ from a spectral output the full width at half maximum (FWHM) is used for approximation of $\Delta\lambda$. The application for which the interferometer will be used should be considered while selecting an appropriate illumination source. For example, if performing VSI analysis an extremely short coherence length is preferred. This would allow modulation only when the reference and object paths are nearly identical. A white LED might result in a coherence length on the order of 1 $\mu$m. In the event that an optoelectronic holography (OEH) system is to be used for measuring deformations of large, diffuse, objects using speckle interferometry a laser source with a long coherence length is desired.

For the use of PSI to characterize MEMS topography it is desirable to have an intermediate coherence length. The coherence length should be long enough such that

fringes are observed over the entire object, even if height varies by several microns, yet not so long that speckles are observed on the object. Also, it is advantageous to only observe fringes on one surface at a time, limiting the desired coherence length. Typically, monochromatic LED sources suit the requirements well. The spectral profile presented in Fig. 12 is for a red LED, and upon inspection of the plot it is possible to approximate the coherence length. The peak wavelength, $\lambda$ is 618 nm, while the FWHM is 15 nm. These parameters used in Eq. 12 lead to a coherence length of about 25 μm. This length should allow the visualization of approximately 75 fringes at once, yet still allow for aligning the interferometer such that only one surface of the MEMS has fringes visible.

### 2.3.2. Phase shifting

To extract quantitative information from the interferometric techniques employed in this study a temporal phase measurement interferometer (TPMI) is used. Basically, known changes in phase are introduced by stepping the reference mirror a known amount between image recordings. The temporal term refers to the fact that phase is varied in time, generally on the order of the camera (or detector) frame rate. The equation describing the interference of two light waves has been introduced as Eq. 6. In this equation $I$ is measured at each pixel position. Three unknowns are present: $I_b$, $I_m$, and $\phi$. To solve for the shape, which is contained in the phase term $\phi$, there must be at least three equations of the type of Eq. 6. By applying a known phase shift, $\Delta\phi$, it is possible to generate a system of as many equations, in the form of

43

$$I_n(x, y) = I_b(x, y) + I_m(x, y) \cos[\phi(x, y) + \Delta\phi_n].$$ (13)

The coordinates $x$ and $y$ represent pixel position and $I_n$ indicates the $n^{th}$ phase stepped image. The coordinate terms $(x, y)$ will be omitted in further equations for convenience, however it should be noted that all equations throughout this section must be applied to each pixel.

Provided there are at least three phase stepped images, of known and constant step magnitude, it becomes possible to generate a solution to the system of equations using a least squares technique (Kreis, 1996). Appendix B presents the procedure for determination of the phase equation for a five-step process of 90° steps. Following the least squares methodology three common solutions are produced,

$$\phi_{three} = \tan^{-1}\left(\frac{I_3 - I_2}{I_1 - I_2}\right),$$ (14)

$$\phi_{four} = \tan^{-1}\left(\frac{I_4 - I_2}{I_1 - I_3}\right), and$$ (15)

$$\phi_{five} = \tan^{-1}\left[\frac{7(I_4 - I_2)}{4I_1 - I_2 - 6I_3 - I_4 + 4I_5}\right],$$ (16)

for three, four, and five steps of 90°, respectively, with Eq. 16 being the same as Eq. B-21 of Appendix B.

More than the required three steps are often recorded as the sensitivity to errors, such as non-linearity and miscalibration of the phase step, is decreased as the system becomes over defined. An alternative approach is introduced by Hariharan et al. (1987), based on the prior work of Schwider et al. (1983). This technique involves using five

steps, solving for the phase term using a four step algorithm twice, once for steps one

through four, and then for steps two through five, giving the equations

$$\phi_{1-4} = \tan^{-1}\left(\frac{I_2 - I_4}{I_3 - I_1}\right), \quad and \tag{17}$$

$$\phi_{2-5} = \tan^{-1}\left(\frac{I_2 - I_4}{I_3 - I_5}\right). \tag{18}$$

The sine term (numerator of the arctangent function) and the cosine term (denominator of

the arctangent function) are summed for the two measurements. Resulting in the solution

for $\phi$ as

$$\phi = \tan^{-1}\left[\frac{2(I_2 - I_4)}{-I_1 + 2I_3 - I_5}\right]. \tag{19}$$

An alternative approach to the solution of the unknown phase term is the

approach known as the Carré-formula (Carré, 1966),

$$\phi_{Carre} = \tan^{-1}\left(\frac{\sqrt{I_1 + I_2 - I_3 - I_4}\sqrt{3I_2 - 3I_3 - I_1 + I_4}}{I_2 + I_3 - I_1 - I_4}\right). \tag{20}$$

The magnitude of the phase step is not critical for the Carré-formula, it must only be

constant (linear). The phase step value calculation is performed within Eq. 20, providing

a technique which is robust to linear errors in the phase shift. This advantage is however

countered by a sensitivity to phase step non-linearity, as well as being computationally

expensive in comparison to the alternative methods.

It might also be important to determine the phase step between the recorded

images during PZT calibration. For the case of five phase steps, with goal of 90º,

$$\Delta\phi = \cos^{-1}\left[\frac{I_1 - I_5}{2(I_2 - I_4)}\right], \tag{21}$$

gives the phase step (Cheng and Wyant, 1985). Another important property that can be determined from the phase stepped intensities is the modulation intensity, $I_m$. The modulation may be used as a threshold filter, disregarding pixels which do not modulate, such as those out of the coherence range. The modulation intensity, which is seen in Eq. 13, is solved for, giving

$$I_m = \sqrt{(I_1 - I_3)^2 + (I_4 - I_2)^2}, \tag{22}$$

based on the results of the least squares solution to a four step algorithm.

## 2.4. Processing by Hariharan technique

Thus far a description of the theory behind interferometry has been presented mathematically. Throughout this section a tilted mirror will be used as an example to demonstrate the steps taken to analyze and scale phase. The processing is performed following Eq. 19, the Hariharan technique for five phase steps. The measurements have been made with a Twyman-Green interferometer, similar to that displayed in Fig. 11. Five phase steps are recorded, shown in Fig. 13, with a phase step of 90.03° as determined by Eq. 21.
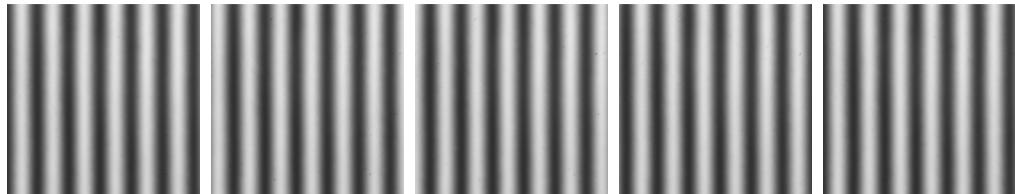


Fig. 13.  Five phase stepped images, tilted mirror.

This example is able to verify the modulation equation, Eq. 22. The modulation is calculated at each pixel and displayed as an image, Fig. 14(b). Perfect modulation gives a white pixel, while zero modulation displays black. Horizontal traces are taken across the first phase step and modulation images. The fringes produced by the tilted mirror show the full range of modulation, with a uniform variation from light to dark. The trace of the image intensity appears sinusoidal, with peak-to-peak amplitude equal to the modulation. In this example, the peak-to-peak value is 162. The average value of the trace through the modulation image is 163. This particular example has excellent modulation, as expected for a near ideal case with a mirror as the object.
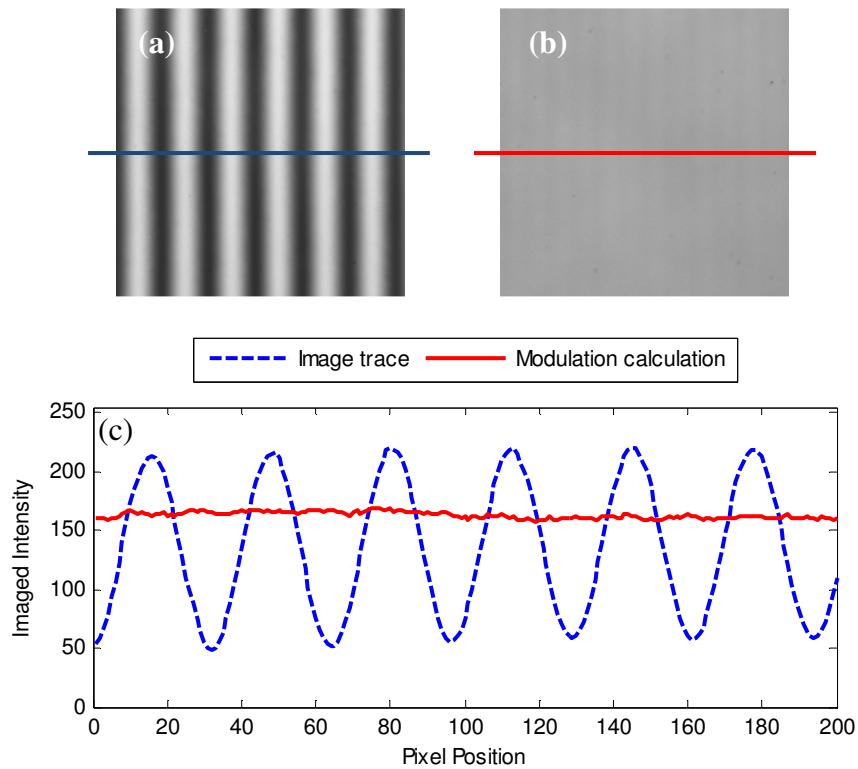
Fig. 14. Modulation calculations: (a) fringe pattern of the first phase step, (b) modulation map calculated for measurements, (c) traces through centers of (a) and (b).

All solutions for the phase term from the phase stepped images contain an arctangent function. This function results in a discontinuous phase surface, wrapped modulus $2\pi$. The wrapped phase image of the tilted mirror, along with a trace through the center of the measurement, is shown in Fig. 15. Phase unwrapping is performed to remove the discontinuities. By comparing neighboring pixels and performing a shift of $2\pi$ whenever the difference between pixels is greater than $\pi$.
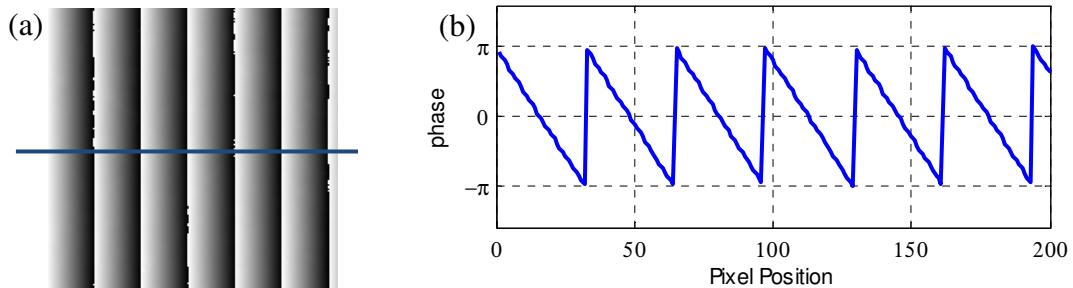


Fig. 15. Wrapped phase: (a) wrapped image, (b) trace across center of a wrapped phase.

A flood unwrapping algorithm is used to allow processing around areas of no modulation. In a more traditional raster scan unwrap procedure the process will stop upon encountering a non-modulating pixel. The flood unwrap simply proceeds in other directions until all adjoining pixels which modulate have been unwrapped. Pixels which do not modulate, such as those from a back surface of a MEMS device, are not unwrapped and are disregarded from this point forward. The flood algorithm begins with a seed pixel from within the image to be unwrapped and moves outward in all directions from that pixel. Various steps along the unwrapping process are shown in Fig. 16.
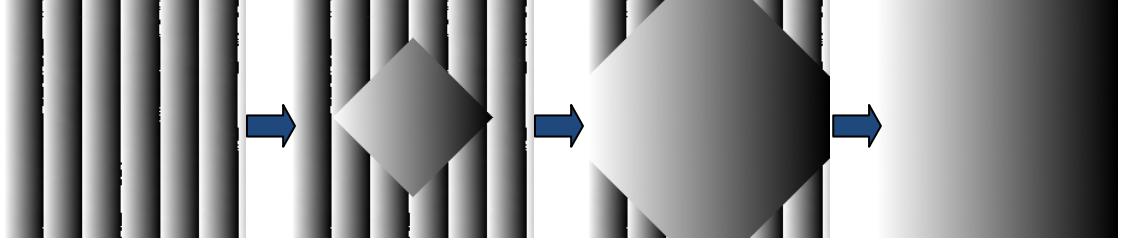
Fig. 16.  Unwrapping of tilted mirror in various intermediate states.

Once unwrapped, the shape is known in units of phase.  By considering the wave

number and the geometry of the interferometer the unwrapped phase, $\phi_{uw}$, can be

converted to units of length,

$$\Omega(x, y) = \frac{\phi_{uw}(x, y)}{\boldsymbol{K}k} = \phi_{uw}(x, y)\frac{\lambda}{4\pi}, \tag{23}$$

where $\Omega$ is the scaled shape known as the fringe-locus function, $\boldsymbol{K}$ is the sensitivity

vector, and $k$ is the wave number, as defined in Eq. 2.  The sensitivity vector is a function

of the interferometer geometry and is defined as a difference between the unit vectors

describing the direction of observation and illumination (Pryputniewicz, 1995).  For the

case of a Twyman-Green configuration $\boldsymbol{K}$ is defined as

$$\boldsymbol{K} = 0\hat{\imath} + 0\hat{\jmath} + 2\hat{k}, \tag{24}$$

and is replaced by the $\hat{z}$ component of $\boldsymbol{K}$.  This is only the case for a retro reflective

interferometer as for other geometries the scalar value for the $\hat{k}$ component is less than

two.  Completing the analysis by scaling the measured data results in the scaled shape

shown in Fig. 17.
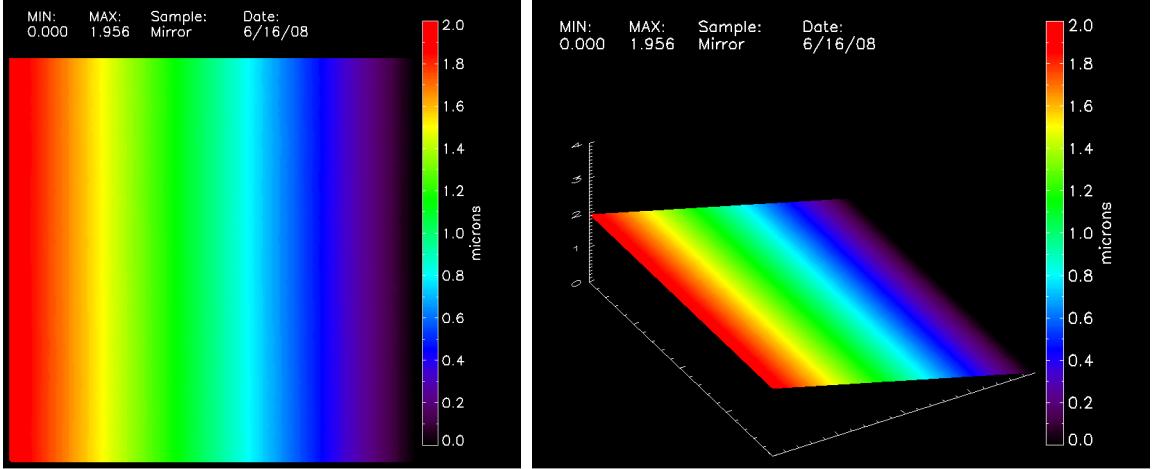
Fig. 17. 2-D and 3-D representation of unwrapped phase for a tilted mirror.

## 2.5. Errors

Accuracy of amplitude division interferometers has been stated in literature at $\lambda/1000$ (Schwider et al., 1983). The accuracy for phase stepped interferometry is dependent on a number of errors, including phase step errors, stability errors, and/or camera noise. Compensation of these errors may be achieved by applying appropriate phase calculation algorithms and/or by physical means.

### 2.5.1. Phase step errors

Piezoelectric devices are often used to induce phase changes by moving the reference mirror in PSI. Errors of both a linear and nonlinear nature adversely affect the accuracy of PSI. Linear phase step error is often caused by miscalibration of a phase stepping PZT, resulting in constant offset in the phase step. Nonlinear error is due to the mechanical relation of strain to electric field (Chen and Wei, 2004). Both such errors produce a ripple effect throughout the measurement, with a frequency twice that of the

fringe frequency (Creath, 1991). The intensity observed by the camera is rewritten to include linear and quadratic coefficients of the phase step (Ai and Wyant, 1987),

$$I = I_b + I_m \cos(\phi + c\Delta\phi + d\Delta\phi^2), \tag{25}$$

where $c$ and $d$ are the linear and quadratic coefficients of the phase step, respectively.

Ideally, proper calibration of the PZT should eliminate any linear errors; however this might not be practical. The different techniques for processing interferometric measurements, as discussed in section 2.3.2, have varying degrees of sensitivity to phase step errors. Proper selection of phase algorithm limits the propagation of such ripple errors. Creath (1993) plotted the effects of linear phase step calibration errors as phase peak-valley (PV) amplitude as a function of percent error. This procedure is repeated herein, although rather than represent error as a PV value, the root mean square (RMS) value is used; also the phase is converted into length units (of nanometers) based on a red light source of 640 nm. This simulation follows a method described by Hu and Chen (1997), where artificial fringes are generated and analyzed. The fringes are generated following Eq. 25, with $d = 0$, and c varying from 0.8 to 1.2. The processing is performed in MatLab with results for all five algorithms previously introduced, Fig. 18.
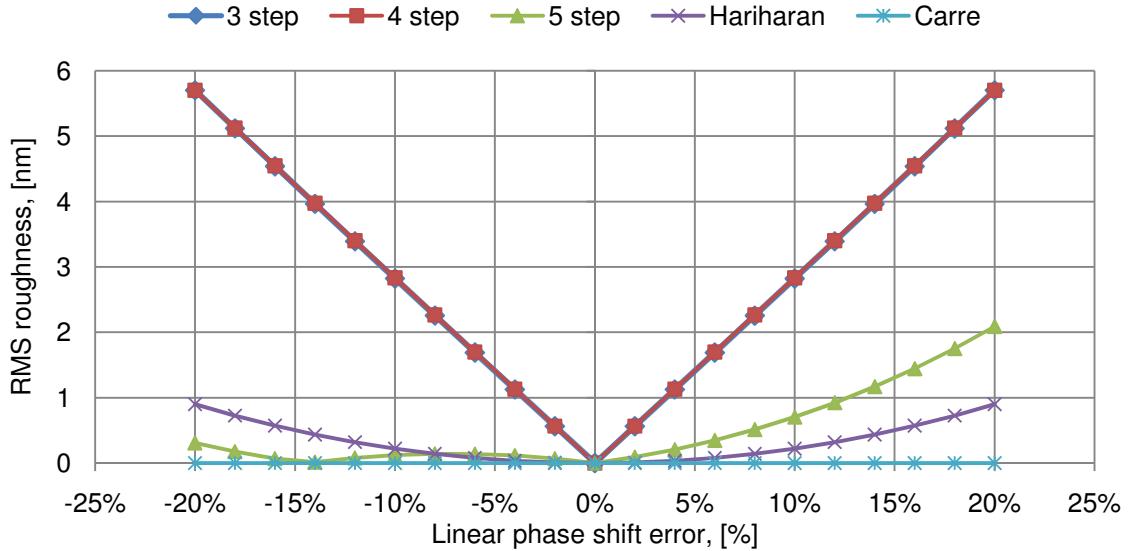
Fig. 18. Simulation of linear phase shift error using different analysis techniques.

The simulations suggest that either the five step, Hariharan, or Carré algorithms are far superior to the three and four step methods; note that results for the three step and four step analyses are virtually identical. Results of the simulation are corroborated by experimental analysis.

A linear error has intentionally been experimentally applied to the PZT, with results of the RMS roughness plotted Fig. 19. A constant phase step with a proportional error, giving constant phase steps of non-ideal amounts, is used during the data acquisition. Five phase steps are recorded at each of the error states from -20% to +20%. In the case of the three step and four step analyses only the first three or four images are used for processing. This procedure allows for using the same set of phase stepped images for all five of the analysis techniques. The actual phase step, which is an independent variable for this experiment, is verified by applying Eq. 21 after recording.

The experimental results corroborate the analytical simulations. The major discrepancy between analytical and experimental is that there are no measurements with a RMS roughness of zero. The experimental procedure approaches a minimum roughness of 0.8 nm (at 640 nm illumination). This threshold might be due to the actual roughness of the mirror, environmental instabilities, or noise limits in the detector.
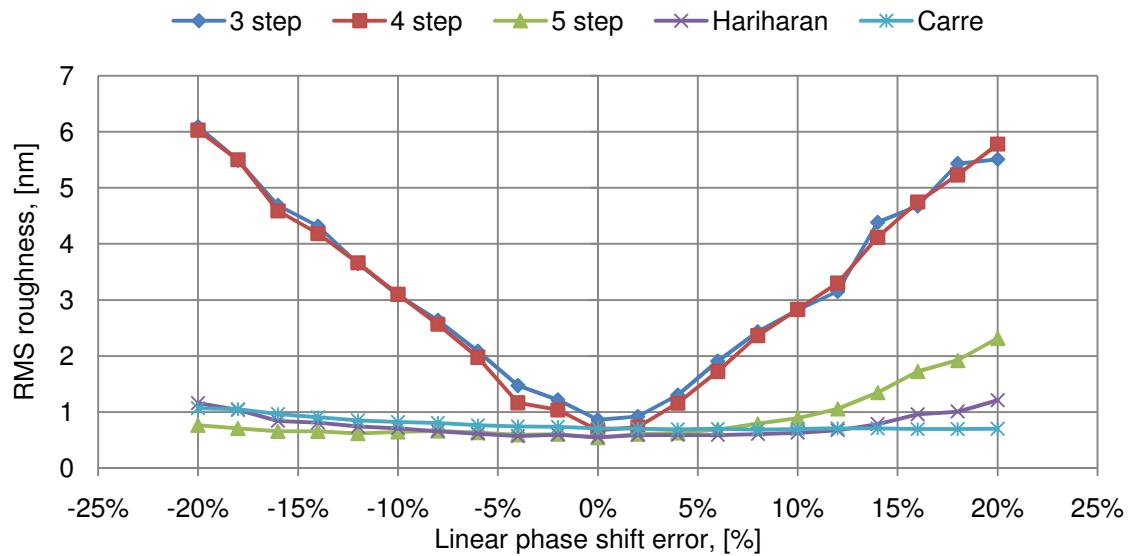


Fig. 19. Phase shifter experimental calibration errors for different analysis techniques.

Effects of nonlinear errors have been predicted in a similar way. The linear coefficient, $c$, is held constant at 1.0 while varying $d$ from -0.05 to 0.05, simulating 5% nonlinearity in either direction, Fig. 20.
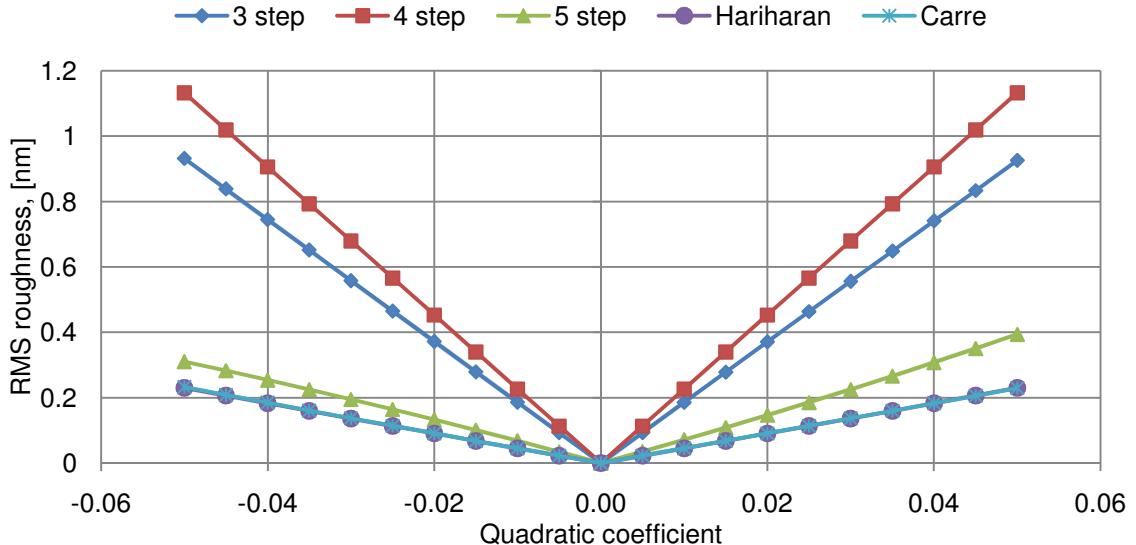
Fig. 20. Simulation of nonlinear phase shift error using different analysis techniques.

Similar to the case with linear error, the over defined solutions perform better. Experimental validation of the nonlinear phase step error has not been performed as such measurements are not practical. It is difficult to directly calculate the degree of nonlinearity in a set of phase steps. Furthermore, PZT transducers almost universally have both a linear and non-linear region. The non-linear regions are at the extremes of the input voltages, with a linear relation between voltage and displacement present for much of the range. A bias voltage is applied, prior to phase stepping, such that all steps are performed in the linear range of the device.

Based on the results of simulations and experiments the Hariharan algorithm has been selected as the preferred method for analysis. All results presented from this point on have been analyzed following this procedure.

## 2.5.2. Environmental influences

While making measurements with sub-nanometer resolution the environment becomes critical. Vibrations from the ground or acoustic sources easily couple into measurement systems, resulting in an instable fringe pattern. Optical tables designed with a massive, stiff table top, supported on pneumatic legs serve to damp vibrations. Acoustic waves are able to bypass the table damping, they are minimized by limiting the activity in the room during image acquisition.

The environment in which measurements are made is critical to the performance of the measurement system. Temperature should be held within a high tolerance to reduce the possibility of expansion (or contraction) in mechanical components comprising the interferometer between measurements. Also, air currents caused by convection or ventilation ducts, might couple into the interferometer, causing instabilities in measurements.

The system that has been developed for this work is unique in that it may be operated remotely. This minimizes operator caused disturbances in the laboratory during data acquisition, while also allowing for process monitoring during long term experiments without entering the room.

# 3. HARDWARE

The interferometer assembled for the measurement system is closely modeled off previous interferometers fabricated in the CHSLT (Klempner, 2007). The complete setup is shown in Fig. 21.
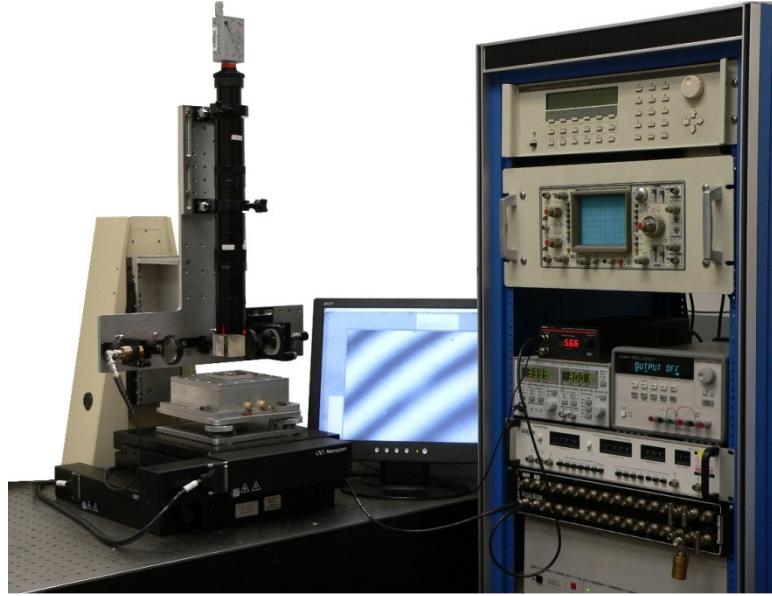


Fig. 21. Interferometric measurement system used for analysis.

Included in the system is 5 axis positioning (3-axis linear, 2-axis tilt), LED illumination, TEC controlled thermal chamber, PZT phase stepping and modulation adjustment, DC voltage source for driving MEMS components, variable phase function generator, 1.3 MP imaging, and complete custom PC interface. Throughout this chapter the details of individual components of the system are presented.

### 3.1. Light source

In order to achieve interference while making PSI measurements a coherent light source must be used. As discussed in section 2.3.1, the coherence is related to the wavelength bandwidth of the illumination. Also, it has been shown that coherence is directly related to the maximum path length difference for which interference occurs. The frequency bandwidth of the light source becomes an important consideration when a specific application is desired. For example, if a laser illumination is used on a MEMS device such as a TFG, fringes will appear on all of the surfaces, i.e., both the proof masses and the chip substrate. Analysis of such a fringe pattern is difficult, requiring complex masking to differentiate the surfaces such that unwrapping may be performed.

An alternative coherent light source is a LED, which possesses a coherence length on the order of 10's of micrometers. Such a light source allows for modulation to be focused on a single surface of a MEMS component. This eases analysis by allowing the use of a low modulation filter to remove background surfaces prior to unwrapping. A LED is also capable of providing a strobe illumination up to 20 kHz for dynamic measurements without the requirement of a shutter system. In general, a LED fringe pattern is cleaner than that of a laser. There are no speckles, and also modulation is usually only present on one surface at a time. An example of a proof mass from a TFG is shown in Fig. 22, with (a) being from He-Ne laser illumination and (b) from a LED illumination.
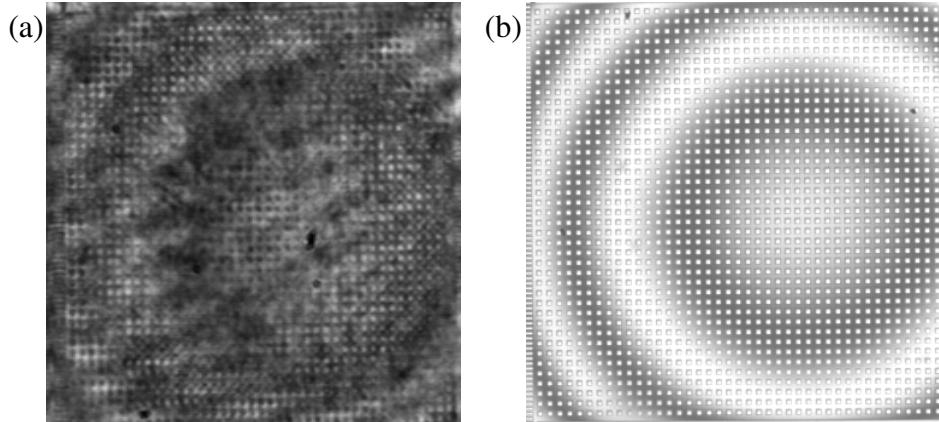
Fig. 22.  Fringe pattern on TFG proof mass: (a) HeNe laser, (b) LED.

The LED that has been implemented for this system is an Opto Diode LD620L
(Opto Diode, 2008), Fig. 23.  The diode has been mounted in a custom 1" brass holder,
allowing for easy connection to a BNC cable and dissipation of heat from the diode.
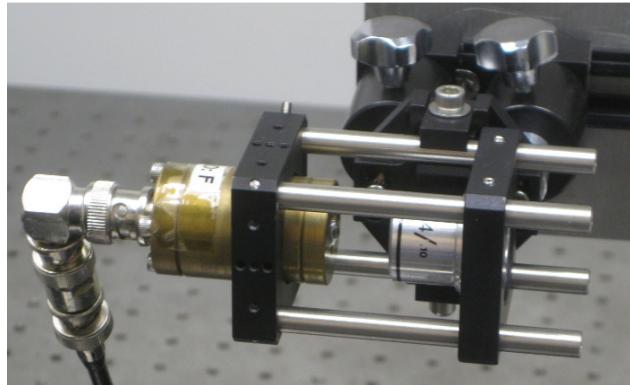


Fig. 23.  Opto Diode LD620L light emitting diode, as installed on interferometer.

The spectral output, as specified by the manufacturer, is shown in Fig. 12.
Calibration of the specific LED, designated as LED F, was performed using an Oriel
model 77200 1/4m monochromator, resulting in a normalized spectral output displayed in
Fig. 24.  The measurements were made at a driving current of 50 mA, which is a typical

value used when measuring MEMS components. Also in Fig. 24 is the spectral output of a He-Ne laser, shown for comparison.
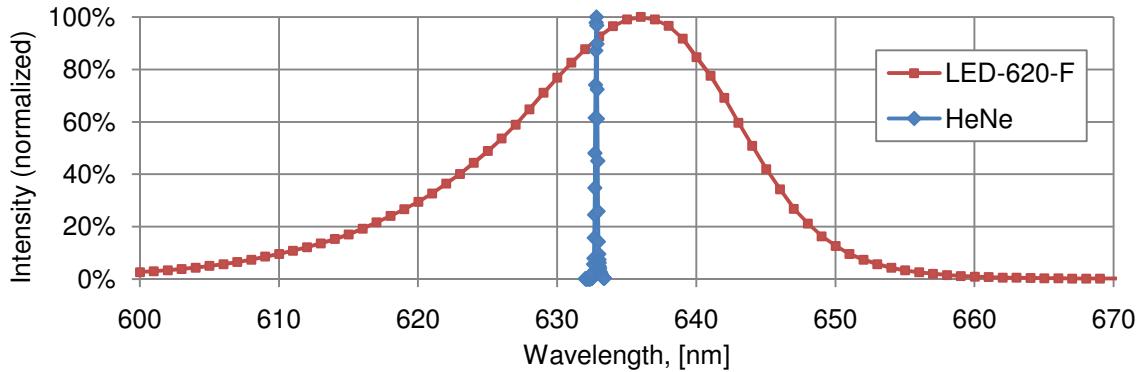


Fig. 24. Spectral output of LED F at 50 mA, as calibrated in CHSLT.

There is a significant shift in the peak wavelength with regard to manufacturer specification of 620 nm. The peak has been measured to be 638 nm, a shift of 3%. It should also be noted that the peak wavelength is a function of the driving current. The peak wavelength has been measured for a range of driving currents, with the results plotted in Fig. 25. The linear relation is used to find the wavelength which is used during the analysis of interferograms.
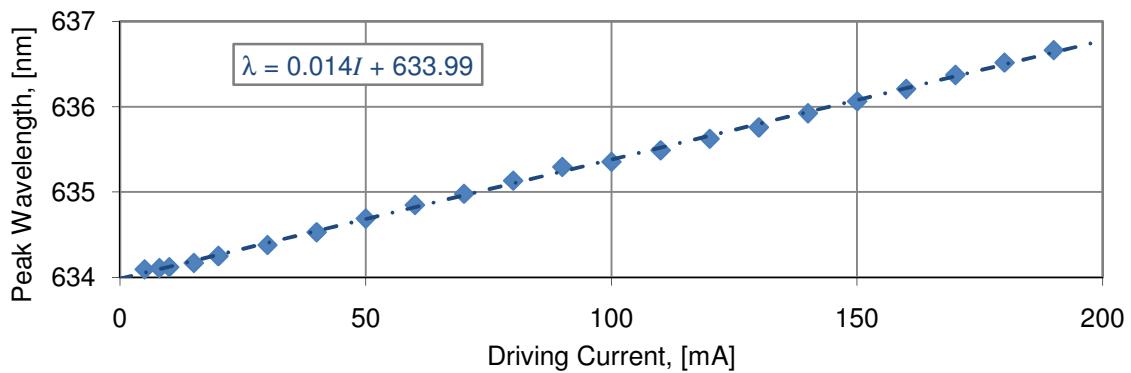


Fig. 25. Peak wavelength vs. input current for LED F.

By applying the calculation of Eq. 12 to the wavelength spectrum for the LED, Fig. 24, a coherence length of 22.8 µm was calculated. This value for coherence length is within 10% of the value calculated based on the manufactures plot, despite a shift in the peak wavelength of 18 nm. This coherence length is not great enough to overcome the temporal path length differences caused by placing a window in one portion of the interferometer, such as the glass lid used in packaging a MEMS TFG (Marinis et al., 2005). A compensation glass of the same material and thickness must be placed in the reference arm of the interferometer to achieve modulation. The same procedure must be followed in the event that measurements are made in a chamber through a window.

The LED is powered by the ThorLabs ITC510 benchtop laser diode and temperature controller. The LED channel has a maximum output of 1 A, more than sufficient for the LED in this system, which accepts a maximum driving current of 300 mA. An external modulation trigger allows for strobe illumination. A trigger signal from the function generator is synchronized with a cyclical motion and sent to the LED for dynamic measurements. Any output set on the ITC510, while in strobe operation, will serve as a DC offset when a trigger signal is used.

### 3.2. Heating element

A critical feature of the interferometer developed within the CHSLT is the ability to apply thermal loading. By making shape measurements at different temperature states it is possible to investigate how performance might be influenced in a real-world

situation.  Also, thermal cycling may be performed to track changes and possible hysteretic effects, or accelerate aging.

Thermal loading is performed via Marlow DT 12-6 TEC.  The TEC works on a Peltier principle, converting voltage to temperature differences.  As one side of the TEC heats, the other side cools.  The hot and cold side of the TEC can be reversed by changing the polarity of the voltage, allowing for a single instrument to be used for both heating and cooling.  The magnitude of the thermal load is dependent on the input current, which when controlled in a closed loop with a thermistor sensor yields precision control of temperature.  Thermoelectric coolers have become commonplace in applications where precision temperature control is required, such as in diode lasers.  The closed loop control is achieved by embedding an Analog Devices AD590 temperature transducer in the heating plate.  The AD590 has a resolution of 0.01ºC, temperature overshoot is minimized with proportional-integral-derivative (PID) control.

Instabilities in the interferometer are often observed when any thermal loading is applied to the component.  Convective currents rise from the heating stage, causing small changes in the refractive index of the air, also slightly deforming the interferometer.  One method of reducing these effects is to enclose the thermal loading within a chamber.  An aluminum chamber has been fabricated specifically for the system developed within the CHSLT, Fig. 26.  Inside the chamber a TEC is mounted on top of a liquid heat exchanger, with an aluminum stage for samples to rest on.  The stage may be interchanged between a blank platform, approximately 2" x 2", or a stage which has been machined to mount a TFG board provided by sponsors with original hardware.  A

neoprene insulation layer separates the hot and cold side of the TEC, reducing thermal currents within the chamber.
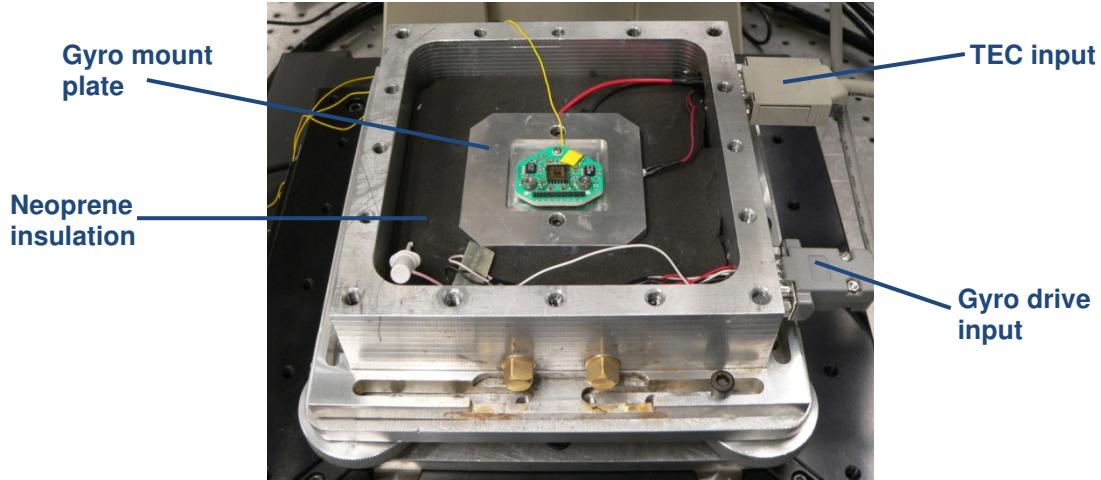


Fig. 26.  Enclosure chamber with TEC heating element.

The liquid heat exchanger rejects heat from the backside of the TEC.  In the absence of the heat exchanger the entire chamber will reach an elevated steady state temperature.  Glycol is circulated through the heat exchanger; maintained at approximately room temperature.  This holds the overall chamber outer temperature near room temperature, reducing convective currents.  The range of temperature achievable in the chamber is restricted between 0 and 100ºC.  Sub-freezing temperatures are possible, however condensation will frost over components.  In similar chambers, which are capable of holding vacuum, temperatures as low as -20ºC are possible.  Electrical feed through ports in the chamber allow for power to the TEC and MEMS components.

The TEC is powered by the same hardware that drives the LED, the ITC510 benchtop laser diode and temperature controller.  For TEC control a total current of ±4 A is available.  The Marlow DT 12-6 is capable of an input current of 5.6 A, allowing for

full use of the ITC510 capabilities. This chamber is unique in that it is completely integrated into the software interface, allowing scripting and remote operation.

### 3.3. Phase variable function generator

Dynamic measurements of cyclical motions (with a frequency much greater than the frame rate of the camera) are possible with a stroboscopic illumination. This technique has often been used with external excitation, such as investigation into resonance frequencies of cantilever beams excited by a PZT shaker. Two signals which share a common frequency are required, one sine signal to excite the PZT shaker, and a square wave to trigger a strobe illumination. It is critical that properties other than frequency are independently controlled in the signals, including amplitude, function type, phase, offset, and duty cycle.

To achieve all the requirements described the WaveTek model 650 variable phase synthesizer was adopted for this system. The instrument functions off a single frequency, however the four outputs allow for complete definition of the output signal. Also, the function generator locks onto an external signal as the master frequency. This feature is utilized when a strobe of the same frequency as a MEMS is desired, such as the operational gyroscopes used in this research. The output functions of the WaveTek have been recorded for the strobe illumination of a TFG, running at approximately 10 kHz, shown in Fig. 27. The solid blue line represents the in-plane motion of the gyroscope, measured directly from the TFG board, and the dashed red line represents the square wave used to trigger the LED.
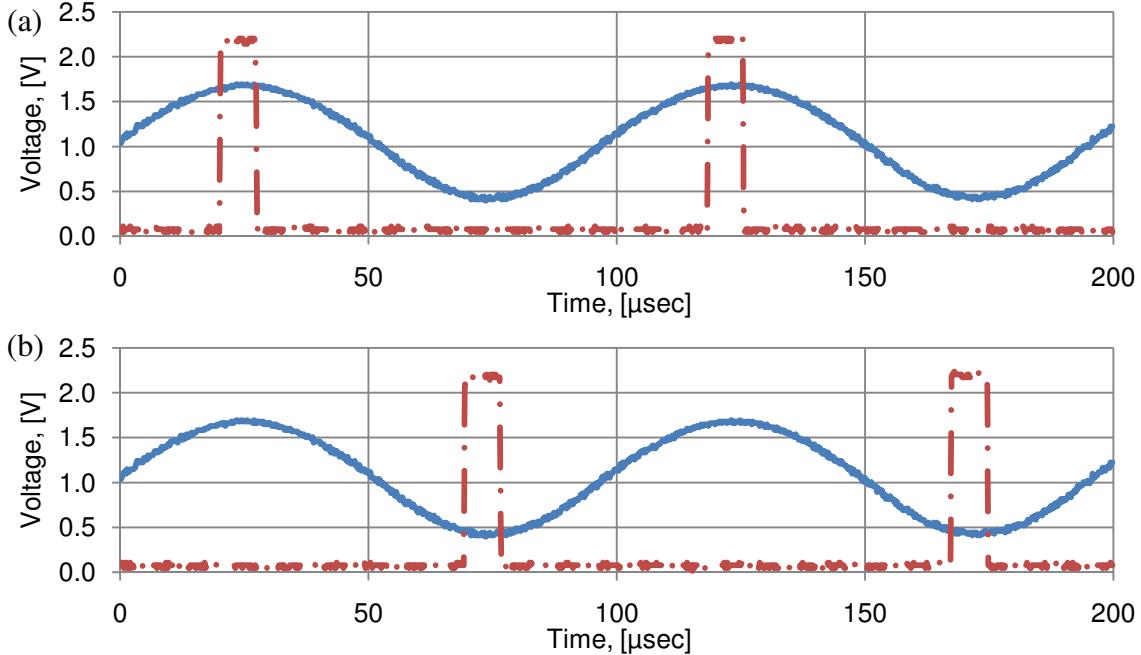
Fig. 27.  WaveTek output signal for gyro position and strobe pulse: (a) phase = 0, (b) phase = 180.

The motion is effectively frozen (to the camera) while the illumination is modulated.  An interferometric measurement can be made, after which the phase of the strobe signal is shifted.  After post processing the cycle is be reconstructed to generated animations of three dimensional motions or compiled into a database where specific behaviors may be monitored.

### 3.4.  Imaging hardware

The automated interferometer records images with the Pixelink PL-A741 machine vision camera.  The full resolution of 1.3 mega pixels (1280 x 1024) can communicate with the host PC via FireWire connection at a rate of 27 frames per second.  Images are stored as 8-bit, grayscale images.  The sensing element is a complementary metal-oxide-

semiconductor (CMOS) consisting of square pixels, 6.7 µm across.  The camera is fully

IIDC-1.3 compliant, allowing for direct control over a FireWire interface with many

software packages, including national instruments LabView.

The imaging is performed with the Infinity K2 long distance video lens with CF-3

optics.  This combination allows a working distance under the microscope of 90-125 mm,

sufficient for looking through a chamber window for heating/cooling applications.


### 3.5.  Reference assembly

A requirement for PSI is a reference mirror which can be shifted precisely and

consistently a fraction of the wavelength.  This reference mirror should also have

sufficient degrees of freedom to match the path length of the object beam and compensate

for tilt, relative to the object.  At least three degrees of freedom for the reference mirror

are required, tilt about the $x$ and $y$ axes, and linear position in the $z$ direction.  In order to

achieve phase shifting as required for PSI measurements a PZT has been installed such

that the reference mirror may be accurately stepped.

In addition to the phase shifting PZT, a second PZT has been implemented for

precision control of the reference mirror position.  A long travel PZT transducer actuates

a linear stage with a total of 700 µm of travel.  The Physik Intrumente P-287.70 actuator

is installed on a low-friction linear stage, as shown in the CAD model assembly, Fig. 28.

The long travel PZT transducer is essential for remote operation of the interferometer.

The $z$ stage on which the interferometer is mounted does not have a resolution suitable

for alignment of the reference and object paths for modulation optimization.

Two-axis tilt stage for
reference compensation

Long travel PZT for
phase adjustment

Manual micrometer
position adjustment
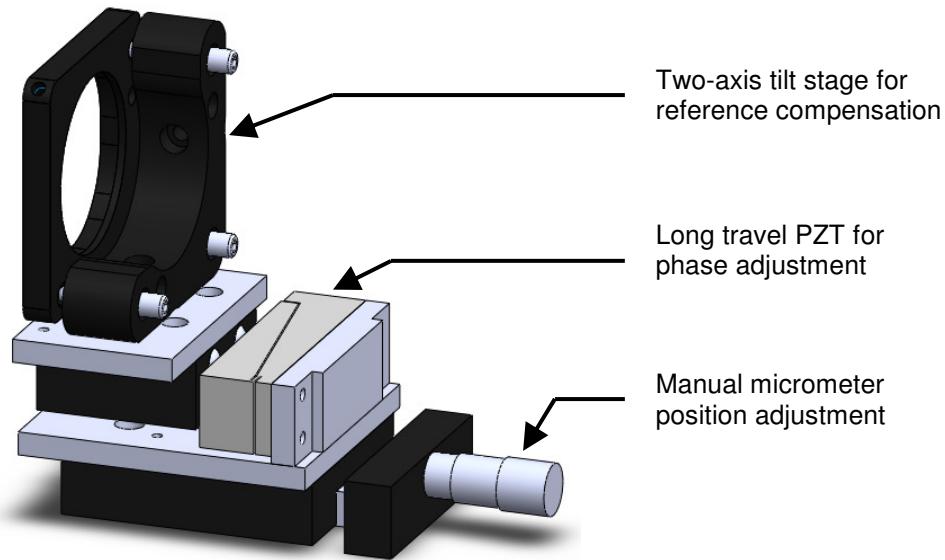
Fig. 28.  CAD model of reference assembly.

The entire assembly has been mounted on a stage with manual positioning control

through a micrometer.  The manual adjustment facilitates alignment of the interferometer

without the PC interface.  Both tilt axes are only controlled through manual operation.

Careful design of the assembly is required to ensure the optical path is in line with the

other components of the interferometer mounted on the base plate.

### 3.6.  Rate table

The Wuilfert EVO-10 precision rate table, which has been customized to accept

the TFG, is used for performance characterization, Fig. 29.  The rate table allows for

mounting of a functional gyroscope on the instrument and rotating at either constant rates

or performing user defined procedures, while recording the gyroscope output voltage.
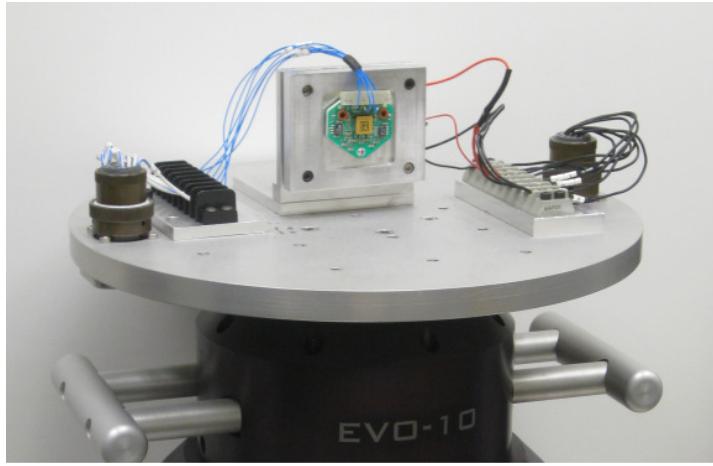
Fig. 29.  EVO-10 single axis rate table with TFG mounted on TEC.

The rate table is capable of rotations up to ±3,000 °/sec, which is sufficient for characterization of inertial sensors for guidance applications.  The test articles, described in section 5.3.1, used in this study function over the range of approximately ±1,000 °/sec. The gyroscope has an output voltage proportional to the input rotation; characterization involves determination of the proportionality constant (i.e., scale factor) and the bias voltage, also referred to as zero rate output (ZRO).  An example of a typical TFG output from a script consisting of constant rate operation and sinusoidal oscillations is shown in Fig. 30.
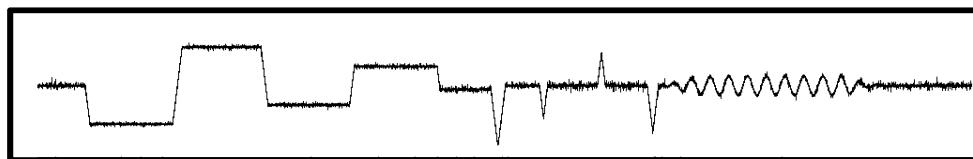


Fig. 30.  TFG output from rate table script, as recorded by digitizing oscilloscope.

A simple test methodology has been developed in which constant rate motion is applied and the DC voltage out of the test article is recorded.  The voltage is recorded

throughout the dynamic range of the gyroscope, in 100º/sec increments.  When plotted
the results are of the form shown in Fig. 31.  The slope of the linear portion provides the
scale factor while the intercept is the bias voltage.
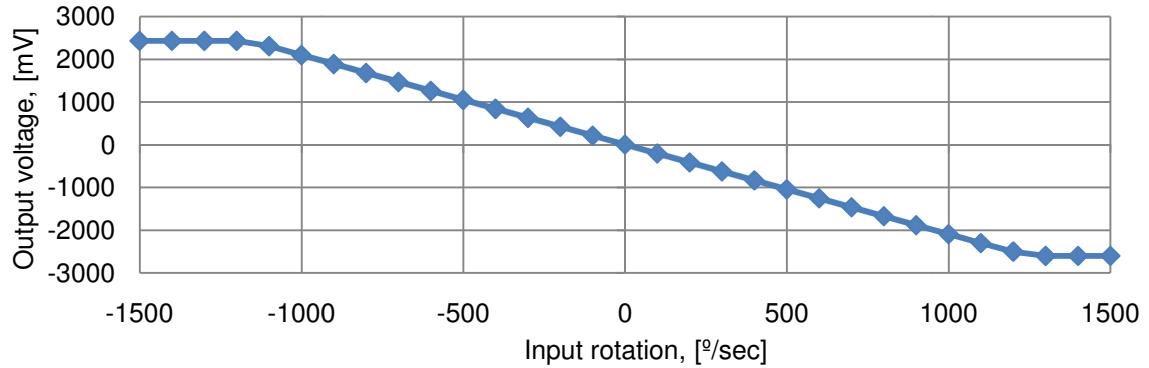


Fig. 31.  Representative result of rate table characterization.


Of particular interest is the response of gyroscopes to thermal loads.  A custom
heating element has been fabricated using a TEC identical to that used in the
interferometer system.  The gyroscope is mounted on a custom heating plate, which is
secured on the front of the TEC element.  A heat sink is mounted on the backside of the
mounting system to dissipate heat rejected from the TEC.  The CAD model, along with
the fabricated mount as installed on the rate table, is shown in Fig. 32.
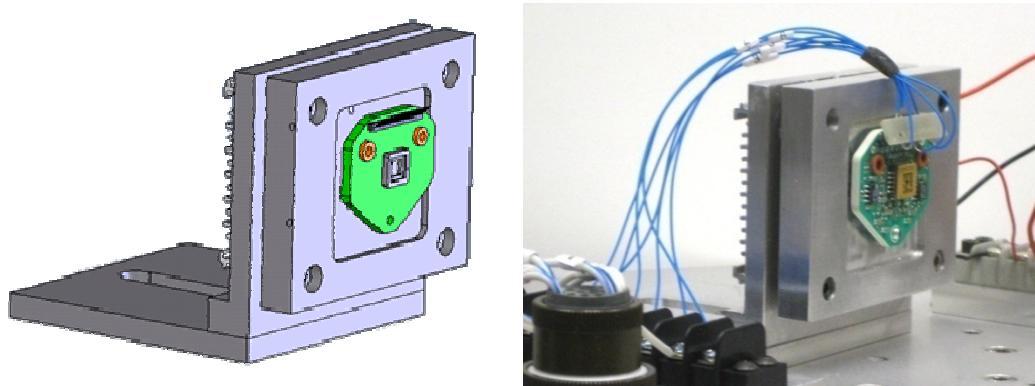


Fig. 32.  CAD model of heating element on EVO-10.

# 4. SOFTWARE INTERFACE

A custom software interface has been developed for the OELIM assembled in the CHSLT. Although the Twyman-Green configuration is common amongst interferometers used in MEMS metrology, the user interface makes the OELIM unique in its abilities. All hardware is remotely controlled via a host PC, allowing for automated data acquisition and remote operation. Communication with the hardware is achieved through IEEE 488 (GPIB), RS-232 (serial), and IEEE 1394 (FireWire) interfaces.

A modular approach is taken in the software design. Each piece of equipment is a self-contained program, all tied together through a main dashboard panel. Such an approach facilitates upgrading of the system, requiring only a portion of software to be modified if hardware is changed. This methodology is consistent with the National Instruments Virtual Instrument (VI) approach.

Scripts which perform tasks consisting of data processing or control multiple pieces of hardware at once are also written as VIs. The automated data acquisition is contained within such a script. Throughout this chapter the software interface is presented, with an emphasis placed on the graphical user interface (GUI) windows that the user will encounter during operation. These sections serve as a user's manual for the software interface.

## 4.1. Main user interface

Upon starting the OELIM software a main user interface opens, Fig. 33. This interface serves as a dashboard for launching sub-routines such as instrument control and script execution.
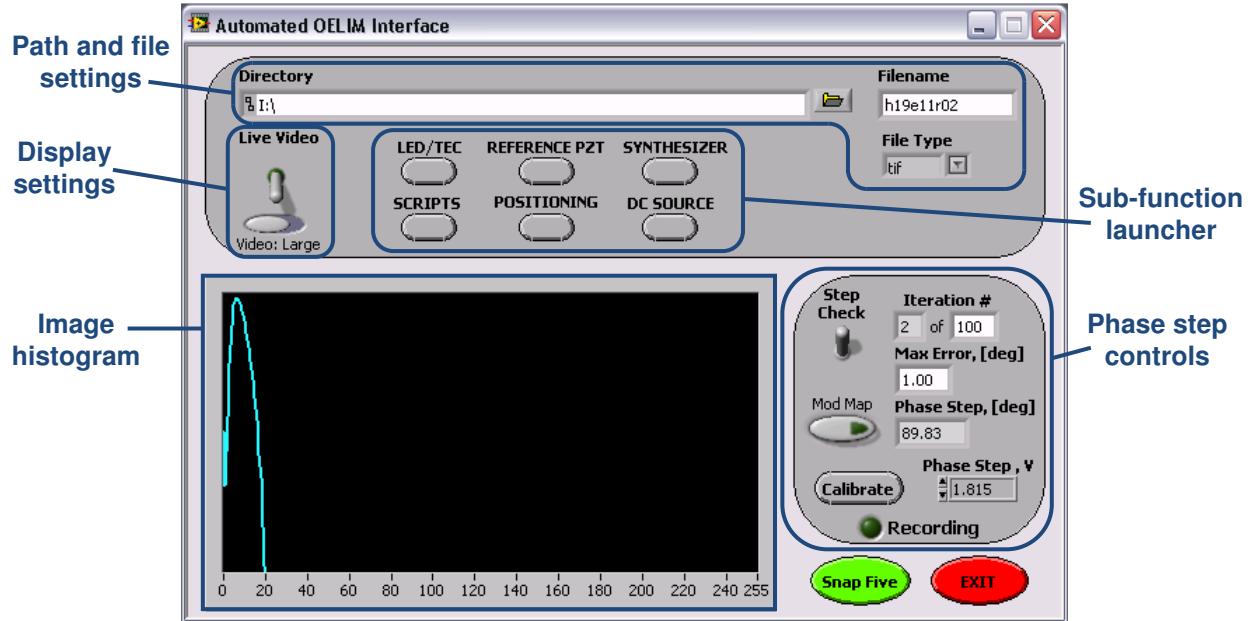


Fig. 33. Automated OELIM interface main panel.

The subsections identified in Fig. 33 are described in detail in the following sections.

### 4.1.1. Path and file settings

For each measurement made a total of five images are saved. In the *Path and file settings*, Fig. 33, it is possible to browse to the directory in which data will be stored, specify the base filename, and specify the image format. The base filename will be the root filename for each image, with the phase step number appended onto the end. The

output file format is designated by one of the four selectable image types in the drop-down box, Fig. 34.
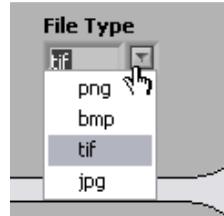


Fig. 34.  File format drop-down list.

The default setting for the image format is 8-bit tif format, which is required for analyzing with IDL software.

### 4.1.2.  Display settings

The *Display settings* region of the main window control live video.  By selecting the toggle switch a window opens to display live video of the camera.  The slider switch under the toggle (labeled Video:Large in Fig. 33) controls the size of the displayed video. In the *Video:Large* setting full resolution (1280 x 1024 pixels) is displayed.  The setting may be changed to *Video:Small* to display a sub-sampled (640 x 512 pixels) video.  This feature is advantageous while operating the system remotely with limited bandwidth.

### 4.1.3.  Phase step controls

Control of the phase step procedure is performed through the *Phase step controls* section of Fig. 33.  The field labeled *Phase Step, V* allows setting of the voltage sent from the PC to the amplifier controlling the phase stepping PZT.  Alternatively, the phase step voltage is determined by selecting the *Calibrate* button.  This feature starts a script in

which phase steps are performed over a finite range of voltages, with a linear regression analysis performed to obtain the ideal phase step voltage. The process is monitored in the progress window, Fig. 35. After completion of the routine it is possible to accept, reject, or retry the calibration, Fig. 36.
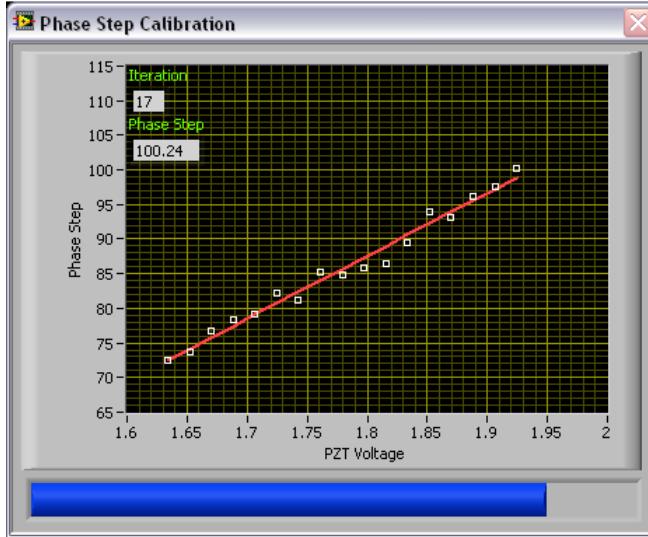


Fig. 35. Progress window for phase step calibration routine.
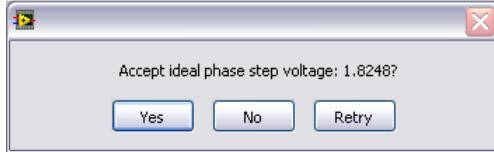


Fig. 36. User dialog after phase step calibration.

Closed loop verification of an accurate phase step is possible by setting the toggle switch labeled *Step Check*, Fig. 33, on. When selected, phase stepped images are stored into a buffer and the actual phase step is calculated, following Eq. 21, and displayed in the field labeled *Phase Step, [deg]*. If the error (in degrees, from an ideal step of 90º) exceeds the value set in the field *Max Error, [deg]*, then images are deleted from the

image buffer and the routine is repeated. Once a set of images meets the error criteria

they are saved according to the settings in the *Path and file settings*, Fig. 33. The

*Iteration #* fields dictate how many attempts have been made at obtaining an acceptable

phase step. The first field under the labels shows the current iteration number for phase

stepping, while the second field is a user entered number of the maximum number of

times phase stepping will be attempted. This feature is to prevent an infinite loop in the

event that the ideal phase step is not achievable, possibly due to PZT failure, LED failure,

inappropriate settings for the phase step, or interferometer misalignment resulting in no

modulation.

The button labeled *Mod Map*, Fig. 33, will calculate, and display, a modulation

image of the recorded data after each measurement. This feature is beneficial to ensure

that measurements are of adequate quality. During the entire measurement process the

*Recording* LED will be illuminated. The measurement is made by selecting the *Snap

Five* button on the main panel.

### 4.1.4. Sub-function VI launcher

Graphical user interfaces for each piece of hardware are opened by selecting one

of the *Sub-function launcher* buttons, specified in Fig. 33. Once a sub-VI is opened it

may only be closed by pressing EXIT button on the sub-VI window. Also, the launcher

button on the main panel will display in red while the sub-VI is running, Fig. 37.
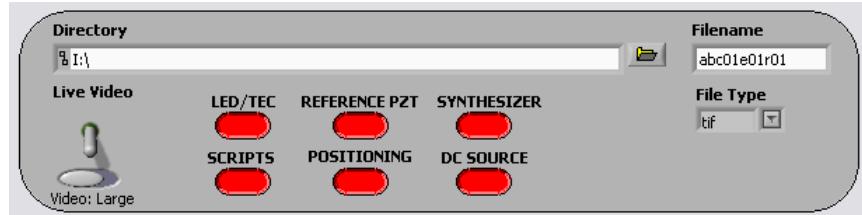
Fig. 37. Sub-function launcher buttons, during sub-VI execution.

Details regarding the operation of the sub-VI functions are discussed in subsequent sections.

### 4.1.4.1. LED/TEC control

Intensity of the LED and temperature control of the TEC are controlled by a single piece of hardware, the ThorLabs ITC510. Upon selection of the *LED/TEC* button on Fig. 33, the instrument control VI opens, Fig. 38.
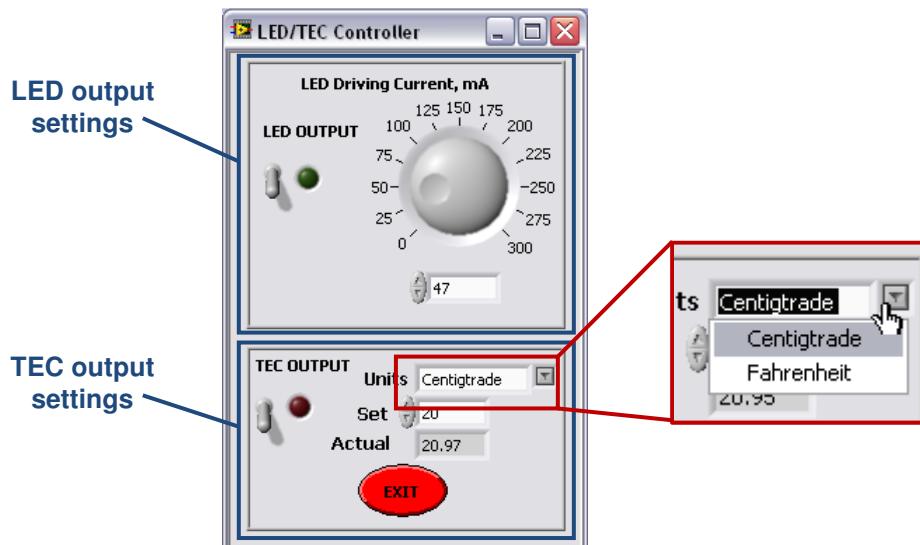

Fig. 38. ITC510 LED/TEC module interface.

Output for the LED illumination and the TEC temperature control are enabled with the toggle switches. LED intensity is adjusted either by the dial labeled *LED Driving Current* or by entering a number in the field below the dial. The output range is constrained to 0-300 mA, the range of operation for the LED in use. The temperature is set by entering a value in the field labeled *Set* in the TEC section. The range is constrained to 5-100ºC. The actual temperature, as measured by the thermistor in the sample stage, is displayed in the field labeled *Actual*. It is possible to switch display units between Celsius and Fahrenheit using the dropdown menu.

To close the window, select the *EXIT* button. Upon closing all values and states will remain as they are set (i.e., if LED is on at 50 mA, it will remain on at 50 mA). The values will still be present the next time the sub-function VI is opened.

### 4.1.4.2. Reference PZT

The reference mirror is mounted on two PZT devices, one which is solely used for phase stepping, and a second, long travel PZT, used for modulation adjustment. The GUI for the modulation adjustment PZT, Fig. 39, is opened by selecting the *Reference PZT* button on the main panel, Fig. 33.
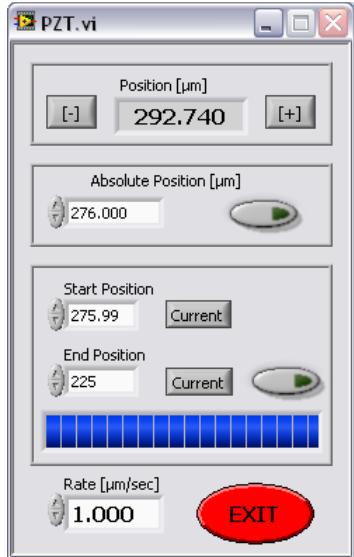
Fig. 39.  Control for reference PZT.

The long travel PZT allows for precision matching of the reference and object paths of the interferometer to maximize modulation.  The PZT has a travel length of approximately 700 µm with a resolution on the order of 7 nm.  The *Rate* field allows for setting of the scan rate of the PZT, all velocities are based on this value.  The PZT runs open loop, limiting the accuracy to approximately 10%.  For scanning the + and – buttons surrounding the *Position, µm* field are used.  The PZT will move while the +/- button is depressed, motion will stop once released. The actual position will be updated at approximately 20 Hz.  If the desired position is known it can be entered into the *Absolute Position, µm* field.  Once this button is pressed the PZT will travel, at the set rate, to the position specified.  Pressing the button in the *Absolute Position* field while the PZT is scanning will stop the motion at its current location.

Scans from one PZT position to another are achieved using the *Start Position* and *End Position* fields. The user enters limits of the motion and starts motion. The status bar will progress as the motion is completed.

Software control of the reference mirror position is critical for remote alignment of the interferometer. The linear stage for the Z-axis is too coarse for modulation adjustment. The reference PZT also facilitates moving between distinct surfaces of modulation remotely. For example, moving between the MEMS and substrate surfaces of a TFG. By scanning only the PZT it is possible to measure and compare multiple surfaces, although the absolute distance between surfaces remains unknown.

### 4.1.4.3. Positioning

Remote positioning of the interferometer relative to the object is performed using three Newport stages for linear translations. In-plane positioning is performed through the *X* and *Y* axes, and out of plane (optical axis) positioning performed through the *Z*-axis. Upon selection of the *Positioning* button on Fig. 33 the motion controller will initialize, Fig. 40. This initialization is only performed once per execution of the OELIM software. After initialization, the motion control is performed through the interface, Fig. 41.
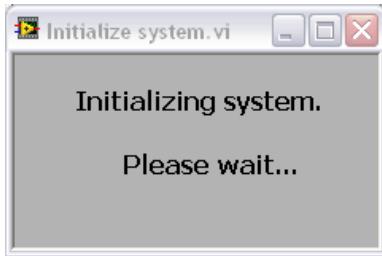


Fig. 40. Motion controller initialization.
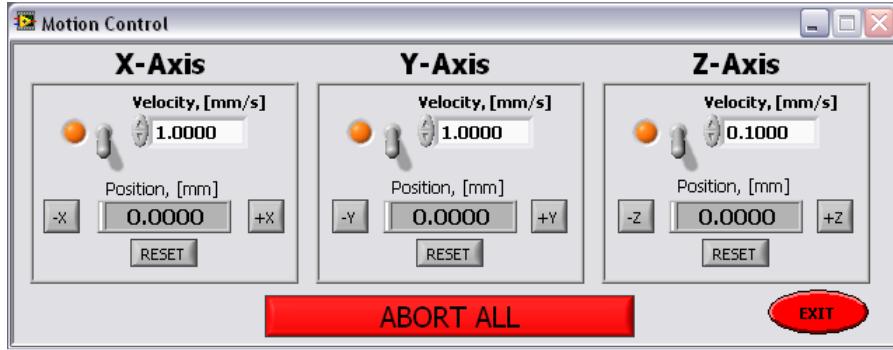
Fig. 41.  Motion controller interface.

Each of the three axes has an identical section in the *Motion Control* VI.  A description of the *X*-axis is presented, however the same operation principles hold for the *Y* and *Z* axes as well.

By default the axis is disabled.  To enable motion set the toggle switch to on. This will change the LED indicator from orange to green for that particular axis, both on the VI window and on the motion controller hardware.  The motion controller is set to jog configuration.  The stage will move while either the –*X* or +*X* button is pressed, in the negative or positive direction, respectively, and stop once released.  The relative position is displayed in the *Position, [mm]* field, which can be reset at any time by selecting *RESET*.   The movement rate may be set at any time by changing the *Velocity, [mm/s]* field.

If unstable operation causes the stages to move uncontrolled, the *ABORT ALL* button will cease all movement and disable stages immediately.

#### 4.1.4.4. DC source

In order to drive MEMS components (in this case TFG sensors) at least one DC voltage source is required. For the samples tested in this study the system requires a total of three voltages, +5 VDC, -15 VDC, and +15 VDC. Remote control of the voltage source is available to start and stop the TFG from the computer interface. This interface is opened by pressing the *DC Source* button on Fig. 33, and is displayed in Fig. 42.
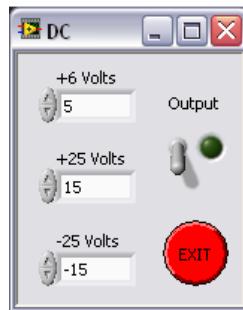


Fig. 42. DC Voltage controller window.

The voltage output is enabled with the toggle switch, the indicator LED will illuminate when the output is on. The output voltages are set with the numerical entry fields. Closing the window is accomplished by pressing the *EXIT* button. The outputs will remain on after exiting the DC controller VI.

#### 4.1.4.5. Synthesizer

A Wavetek model 650 function generator is available for providing a strobe illumination for dynamic measurements. For the samples included in this study the gyroscope output a sine wave of the drive frequency. This frequency is used for phase locking the master frequency of the Wavetek. Output signals of the same frequency are

used to completely define a square wave to modulate the illumination.  The panel for

control of the Wavetek is opened by selecting the *Synthesizer* button from Fig. 33, shown

in Fig. 43.
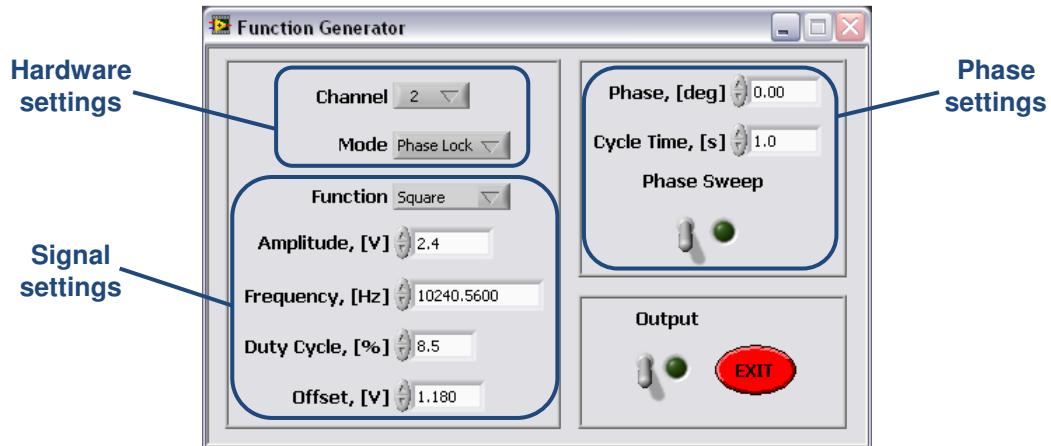


Fig. 43.  Function generator window, for control of Wavetek model 500.

Each of the four output signals is independently controlled from the Wavetek VI,

including setting the mode of operation.  A master frequency can be set within the

instrument, or an external trigger in conjunction with the Phase Lock mode.  The

definition of the output signal is performed via the settings in the *Signal settings* section

of the VI.  The signal phase, relative to the master frequency, can be adjusted, or set to a

sweep mode to visualize the motion at a slow rate.

#### 4.1.4.6. Scripts

By selecting the Scripts button on Fig. 33 the user is able to access the script

library and execute one of the predefined scripts from the Script Manager interface, Fig.

44.
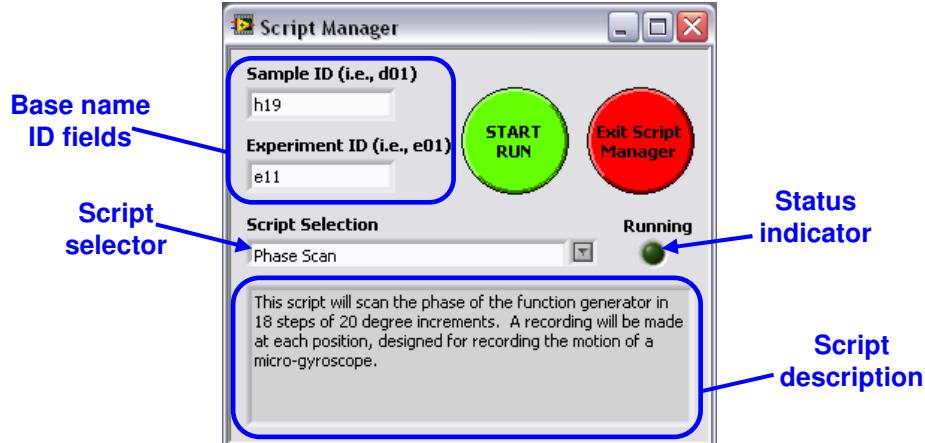
Fig. 44. Script Manager window.

Scripts are LabView VIs that perform data acquisition, thermal loading, or phase control, automatically. There is a library of pre-defined scripts available in the script manager, Fig. 45, or the users may define their own script composed of thermal cycling. A description of the currently selected script is shown, allowing the user to ensure it is the appropriate test.
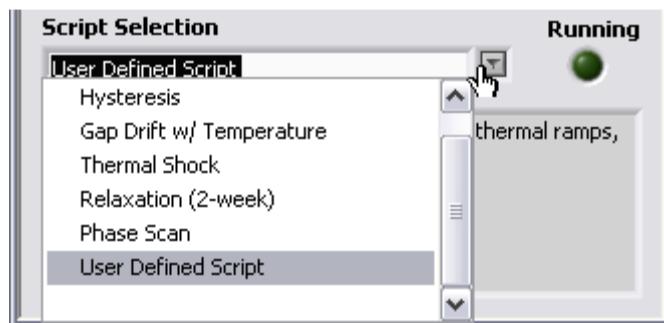


Fig. 45. Scripts available in OELIM software.

Before executing a script the *Sample ID* and *Experiment ID* fields should be filled. These identifications set the base filename for all measurements recorded during the script execution. The measurement iteration is appended at the end of the base filename, in the format of *r##* where *##* is the iteration number. Finally, the phase step

number is appended after a hyphen.  For the example displayed in Fig. 44 the first phase step of the first measurement would be h19e11r01-1.  The file format and saving directory are still governed by the appropriate fields on the front panel, Fig. 33.

Initiation of a script is accomplished by pressing the *START RUN* button on Fig. 44.  This opens the script progress display, Fig. 46.  The current step is displayed, as well as the overall script progress.
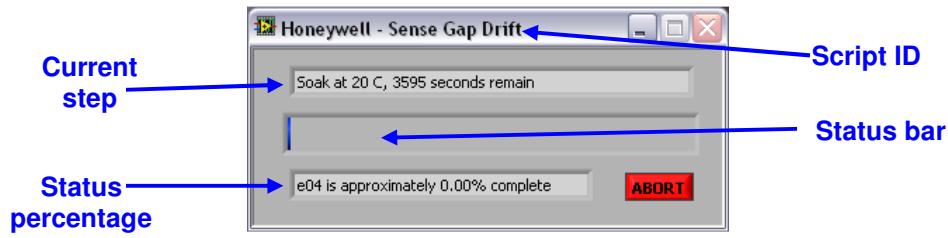

Fig. 46.  Script progress indicator.

The *ABORT* button will stop the execution a running script.  After completion of the script this window will automatically close.  The following sections describe the scripts currently integrated into the OELIM library.

### 4.1.4.6.1.  Hysteresis

A test has been developed for investigation into hysteretic effects of thermal cycling on MEMS devices, Fig. 47, where points along the trace indicate shape measurement points.  This script cycles the component of interest between 20ºC and 85ºC, with shape measurements made during temperature increase and decrease portions of the cycle.  Prior to execution of the script the interferometer should be adjusted such that ideal modulation is observed while the temperature is 40ºC.  All the measurements

are made at a thermal midpoint of the cycle (40ºC) after a soak of two hours. Two

sequential cycles are completed with no interruptions during measurement.
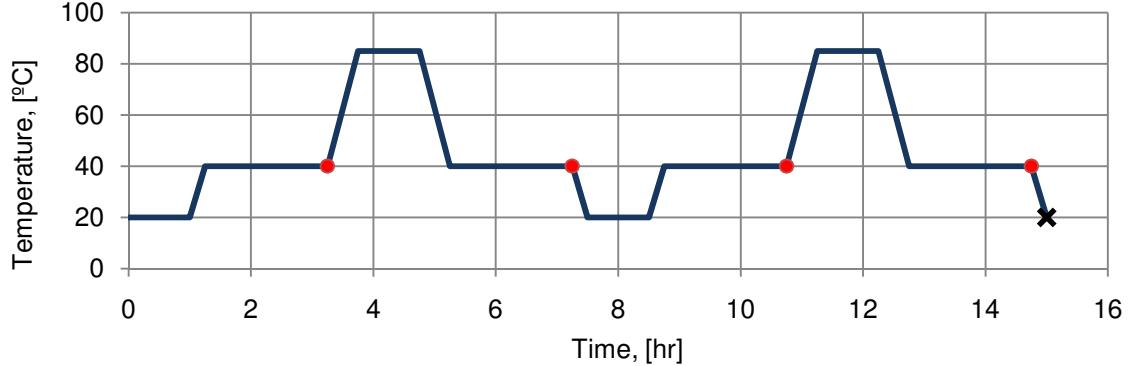


Fig. 47. Hysteresis script measurement profile.

The total time required to complete the two cycles is 15 hours, with the longest

soak time at any single temperature of two hours. This suggests that the experiment

could be completed by manual operation by a single person, however user interaction

must be performed at least every two hours. Such a script is not convenient for a single

operator to perform interactively.

### 4.1.4.6.2. Gap drift with temperature

The gap drift with temperature experiment is designed to monitor shape of a

component over extensive thermal cycling. Specifically, changes in the shape of a TFG

are monitored as temperature is cycled between 20ºC and 85ºC with measurements made

at 40ºC of the increasing temperature portion of the cycle. Prior to execution of the script

the interferometer should be aligned such that ideal modulation is observed at 40ºC. The

first five cycles of the script are shown in Fig. 48, where the points along the trace indicate shape measurement points.
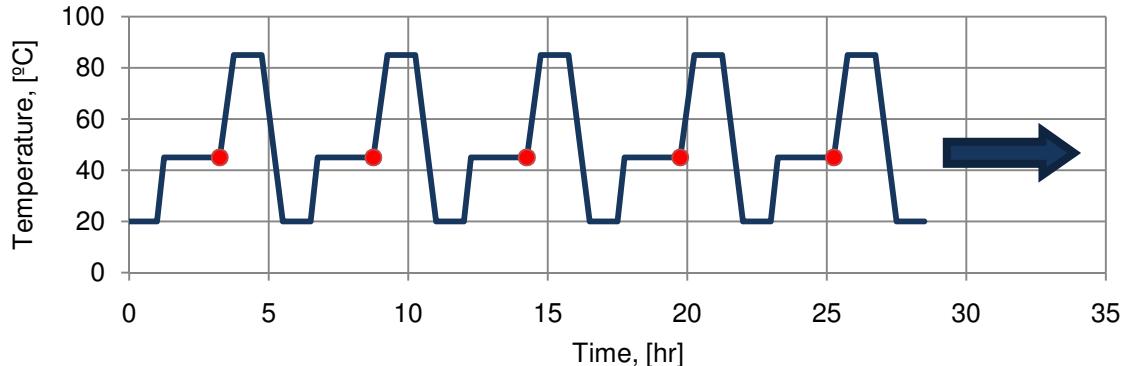


Fig. 48. Gap drift with temperature script measurement profile.

A total of 20 measurements are made for a total execution time of 110 hours, making manual operation very difficult. Investigators would be required to monitor the process and adjust parameters at all times, requiring several shifts around the clock if manually performed.

### 4.1.4.6.3. Thermal shock

The thermal shock script has been designed to monitor the time required for thermal deformations to reach steady state after a long soak period at an elevated temperature. The component of interest undergoes a soak at 85ºC for a period of three days. After completion of the soak, temperature is reduced to 20ºC as fast as possible, at which point measurements are made in varying increments (starting at five minutes and extending to one day between measurements). The process is outlined in Fig. 49, where points along the trace indicate shape measurement points.

84
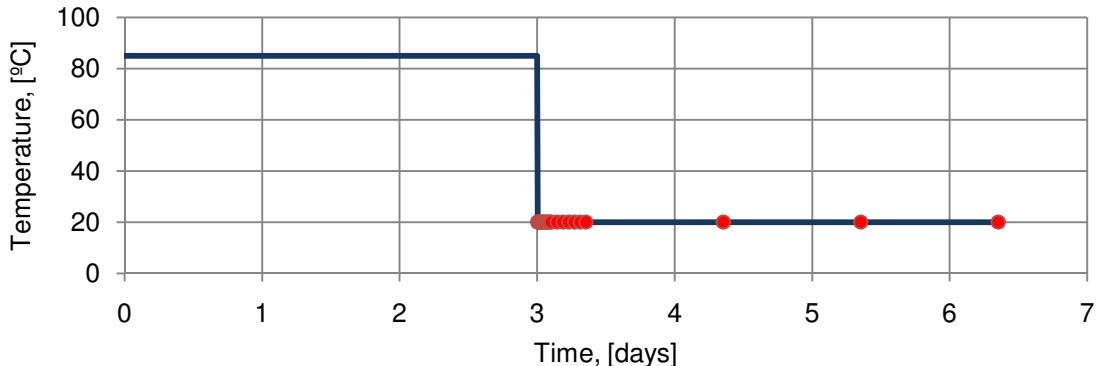
Fig. 49. Thermal shock script measurement profile.

The total process consists of 23 measurements made over 152 hours.  The first 72 hours constitute the elevated temperature soak, while measurements are made periodically throughout the remaining 80 hours.   Twenty of the 23 measurements are made throughout the first day after the thermal shock, with one measurement made per day for the following three days.

### 4.1.4.6.4.  Relaxation

The relaxation experiment has been designed to monitor the time dependant behavior of die bonds in a packaged MEMS device.  The temperature is maintained at a constant 100ºC while measurements are made over a two week period.  The measurements are evenly distributed on a logarithmic scale, shown by the points on Fig. 50.  A total of 25 measurements are made throughout the duration of the experiment.  The non-uniform time increments between measurements make this experiment difficult for manual performance and would require constant interaction and utmost attention.
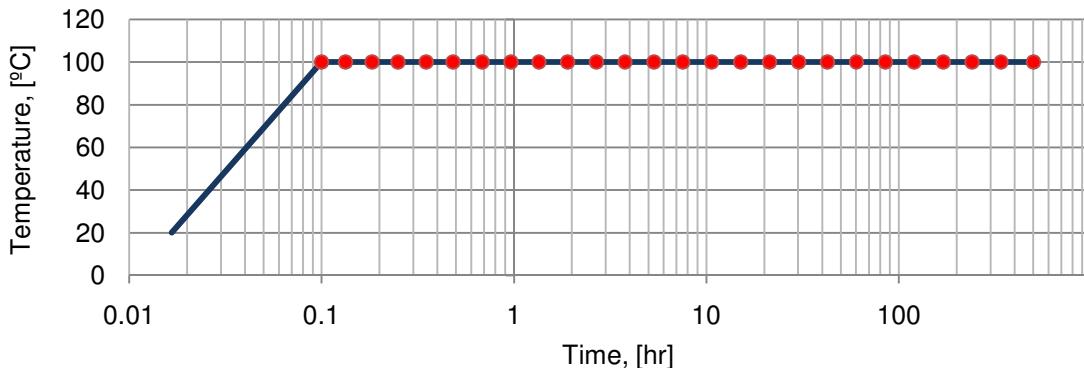
Fig. 50. Relaxation script measurement profile.

### 4.1.4.6.5. Phase scan

The phase scan script makes measurements throughout the operation cycle of a MEMS TFG, or other cyclical motion. Strobe illumination, triggered off the running gyroscope, makes the proof masses appear static. By varying the phase difference between the gyro position and the illumination bursts it is possible to make shape measurements at different positions of the cycle.

Prior to execution of the script the user must configure the LED strobe. First, the gyroscope should be turned on using the voltage supply. Using the LED/TEC control the LED should be turned on, however the driving current should be set to zero. This allows for an output that is triggered by an external signal with no DC offset. Using the synthesizer control, Fig. 43, set the channel number to 2 and the mode to phase lock. The square wave function, with a duty cycle set to 8.5%, produces the shortest pulse for strobe illumination. Turning on the synthesizer output via the toggle switch will start the strobe illumination. The amplitude and offset can be adjusted such that the illumination

maximizes the dynamic range of the camera without saturating the image, as monitored in the image histogram.

The script is graphically shown in Fig. 51, where the y-axis shows in-plane position of the proof mass locations. Unlike the other scripts discussed, this experiment treats relative phase between the proof mass $x$-position and the strobe as the independent variable, and proof mass position as the dependent variable.
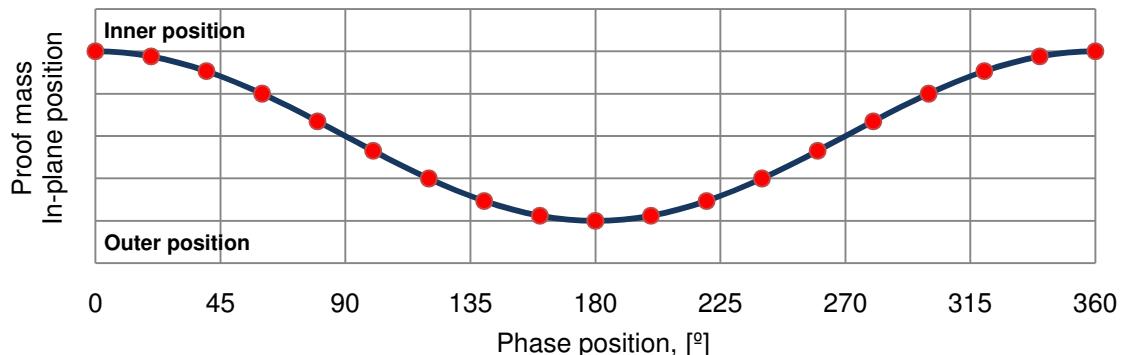


Fig. 51. Phase scan script measurement profile.

A total of 19 measurements are made, each 20º increment of relative phase position, with the first and last measurements at the same location (0º and 360º). Temperature is not controlled in this script, allowing it to be performed at any thermal state desired by setting the TEC control accordingly before execution. A single user is able to perform this script manually; however the time to perform the script is greatly reduced by allowing automated shifting of the relative phase position of the strobe.

Tracking the non-planar motion of proof masses during TFG actuation is key to investigation into mechanical quadrature error. This script is also useful for dynamic excitation, such as modal analysis of an excited structure. Often measurements of modal

analysis only consider the deformation, following this script the shape is measured at each point. The deformations are extracted by treating the initial measurement as a reference with regard to the subsequent measurements.

### 4.1.4.6.6.  User defined script

If the predefined scripts found in the library are not adequate for the desired experiment the user may define a script consisting of up to 12 steps of thermal ramps, soaks, or measurement points, through the GUI interface, Fig. 52.
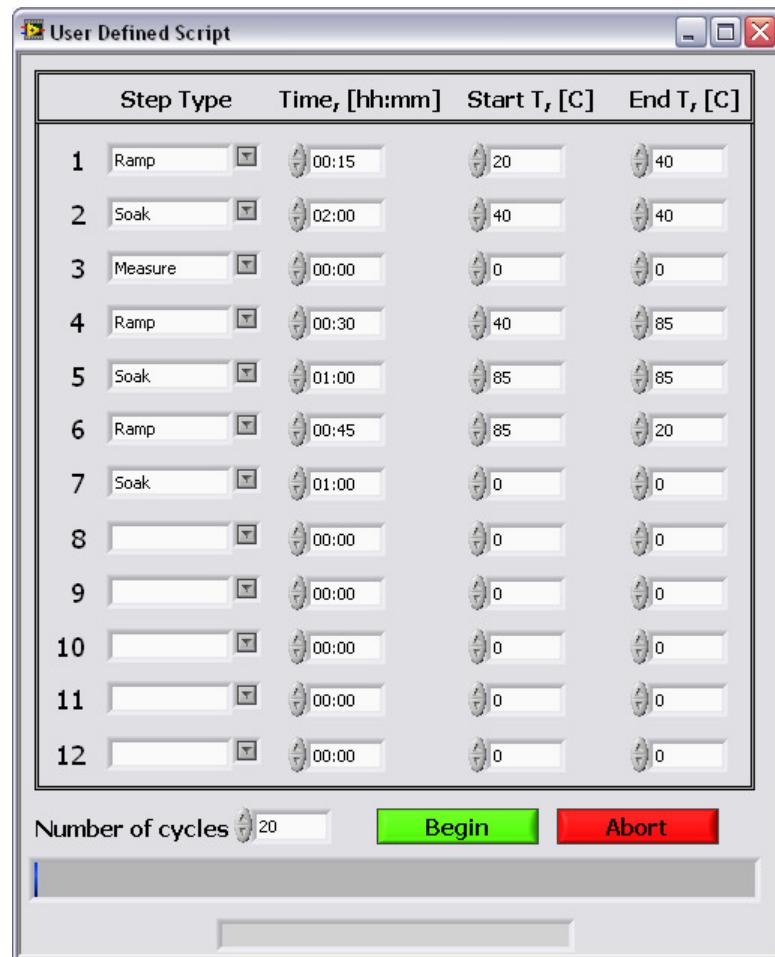


Fig. 52.  User defined script GUI interface.

The user defined script interface allows for the rapid generation of a thermal cycle script without designing a completely new VI.  Up to 12 steps are possible, which may then be cycled for as many as 50 iterations.  For each step the user selects one of three options from the dropdown menu under the *Step Type* heading in Fig. 52.  The first option under the dropdown menu is the *Soak* function.  This command will hold the TEC at the current temperature for the duration set in the *Time, [hh:mm]* field.  The *Start T, [C]*, and *End T, [T]* fields do not affect the soak command.  The second option under the *Step Type* menu is the *Ramp* command.  This option will adjust the temperature from the *Start T* to the *End T* settings linearly over the time set in the *Time* field.  The temperature ramp is digitized into steps performed in 30 second increments.  Finally, the *Measure* option under the dropdown menu triggers a shape measurement.  For this step the *Time*, *Start T*, and *End T* fields have no effect.  Any step that is left blank will be omitted from the process.  Once a cycle is defined it may be repeated by setting the *Number of cycles* field of the user defined script GUI.

Once the script is complete it is started by pressing the *Begin* button on the GUI interface.  The script status is shown in the scroll bar on the bottom of the window.  Any measurements made during the process will be saved based on the fields set in the *Script Manager*, Fig. 44, and the path and file format based on settings for the main user interface.  After completion of the script the *User defined script* window will automatically close.  The steps shown in Fig. 52 are identical to the gap drift with temperature script, shown graphically as Fig. 48.

89

# 5. TUNING FORK GYROSCOPE

Microelectromechanical sensors have become commonplace in inertial sensing due to the high performance and low cost of devices. Employing silicon batch processing techniques, commercial grade sensors are targeted to cost less than $25 per axis (Barbour et al., 1998). There has been significant work in the area of tactical grade sensors, including funding by the Army for development of inertial measurement units (IMUs). Such systems are comprised of at least six sensors; three accelerometers and three gyroscopes. On the forefront of the MEMS gyroscope has been the Charles Stark Draper Laboratory that, in 1987, became the first to sense rate with a MEMS sensor (Barbour and Schmidt, 1999). Draper was also an early pioneer in developing the MEMS tuning fork gyroscope (TFG) (King, 1989), which led to the first silicon TFG in 1993. This work has culminated in the delivery of Honeywell's HG1900, HG1920, and HG1930 INSs (Weinberg and Kourepenis, 2006).

## 5.1. Operation of TFGs

Tuning fork gyroscopes are rate sensors, the output of the sensor is a voltage proportional to the rotational rate input, $\Omega_I$. Details regarding the theory of operation behind these devices are described in literature by Bernstein et al. (1993), Bernstein and Weinberg (1998), Weinberg and Kourepenis (2006), and Sharma et al. (2004), among others. In the MEMS TFG there are two proof masses which resonate, in-plane, in opposite directions, Fig. 53. Excitation is performed by a set of electrostatic combs on the outer edges of the proof masses which produce an attractive force when a voltage is

applied. The proof masses are supported by spring flexures which allow for movement. Careful design considerations in the geometry of flexures supporting the proof masses ensures that the resonance mode excited is the drive mode, where the motion is in the same plane as the chip, with each mass moving in opposite direction. A rotation introduced along the central axis, labeled *y* in Fig. 53, results in a Coriolis acceleration, causing displacements of the proof masses as a function of rotational rate and planer velocity, *v*.
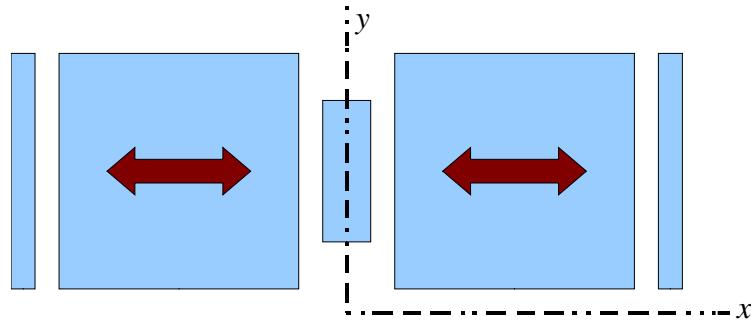


Fig. 53. Schematic of a tuning fork gyroscope.

The Coriolis acceleration, $a_c$, related to relative systems in which there is both linear and rotational motion, can be described mathematically as

$$a_c = 2\Omega_I \times v \, , \tag{26}$$

where $\Omega_I$ is the vector of rotation input to a gyroscope and $v$ is the linear velocity. Equation 26 shows that in the absence of either a rotation or a velocity there is no Coriolis acceleration, requiring for the proof masses to be excited in plane to observe the effect of an input rotation. It is also evident from Eq. 26 that the direction of the Coriolis acceleration is normal to the angular and linear motions, the *z* direction based on the

construction shown in Fig. 53. The scalar Coriolis force in the $z$ direction, $F_c$, applied to each proof mass, $m$, is based on Newton's second law, giving

$$F_c = 2\,m\,\Omega_I\,v\,.\tag{27}$$

The position of the proof masses follows a sinusoidal function, such that relative position as a function of time, written as

$$x(t) = \Delta x\,\sin(\omega_d t),\tag{28}$$

where $\omega_d$ is the drive frequency and $\Delta x$ is the stroke of the proof mass motion. Velocity is obtained by taking the time derivative of Eq. 28, which is then combined with Eq. 27 to find Coriolis force as a function of time,

$$F_c(t) = 2\omega_d m\,\Delta x\,\Omega_I\cos(\omega_d t).\tag{29}$$

The proof masses are supported by springs with stiffness, in the direction of $\boldsymbol{a_c}$, of $k$. This allows for the solution of displacement, $\Delta d_{gap}$,

$$\Delta d_{gap}(t) = 2\omega_d m\,\Delta x\,\Omega_I\,k\cos(\omega_d t).\tag{30}$$

The displacements in $x$ (drive direction) and $\Delta d_{gap}$ (sense direction) are out of phase by 90°. Such signals are referred to as being in quadrature (Allen, 2005). These displacements result in an oval shape motion of the proof mass, when input rotation is present, symmetric about the drive axis, shown in Fig. 54.
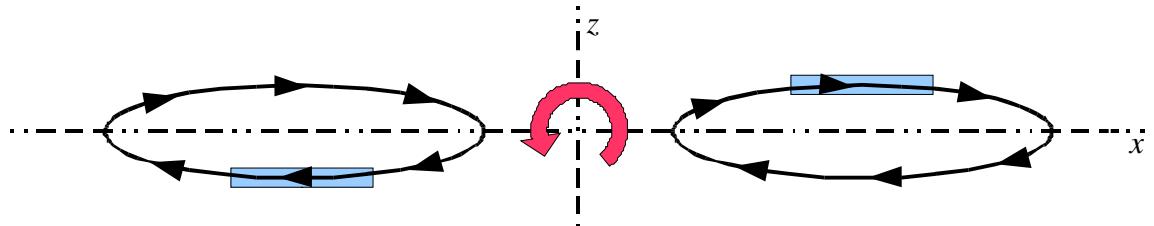


Fig. 54. Motion of proof masses during rotation of a microgyro.

The Coriolis force is measured by tracking the sense gap between the substrate and the proof masses. The gap is detected by the capacitance, $C$, between the bottom of the proof masses and the substrate,

$$C = \frac{\epsilon_r \epsilon_0 A}{d_{gap}}, \tag{31}$$

where $\epsilon_r$ is the relative permittivity of the medium between plates, $\epsilon_0$ is the permittivity of free space, $A$ is the cross sectional area of the overlapping plates (i.e., electrodes), and $d_{gap}$ is the gap between plates. The change in capacitance is based on changes in the sense gap, $\Delta d_{gap}$, from Eq. 30. A capacitance as a function of the input rotation, $\Omega_I$, and time, $t$, is measured,

$$C(t, \Omega_I) = \frac{\epsilon_r \epsilon_0 A}{d_{gap} + 2\omega_d m \, \Delta x \, \Omega_I \, k \cos(2\pi\omega_d t)}. \tag{32}$$

The measured capacitance of Eq. 32 is modulated by the drive frequency. Demodulation of the capacitance signal must be performed to extract the measured rotation.

In order to realize a complete INS based on MEMS technology the sensitivity and stability of the devices must be improved to reach the current standards of ring laser gyros. One method of improving performance is to maximize the quality factor ($Q$-factor) (Sharma et al., 2004, Klempner et al., 2009). The $Q$-factor is defined as

$$Q = \frac{Total \; energy \; of \; the \; system \; stored \; per \; cycle}{Total \; energy \; lost \; per \; cycle}. \tag{33}$$

The $Q$-factor is closely related to damping in the package, both gaseous damping due to the environment in the package and thermo-elastic damping of the flexures. The Q-factor

might be optimized by careful consideration during the packaging of the device, as discussed in section 5.2.

As the fabrication methods have improved another source of error has become significant in recent times, namely a qudrature error. If the motion of the gyroscope is not in the same plane as the substrate then a quadrature error is present, resulting in the displacement in the sense direction ($z$ direction as described by Fig. 54) when no input rotation is present. Graphical depiction of quadrature error is shown in Fig. 55.
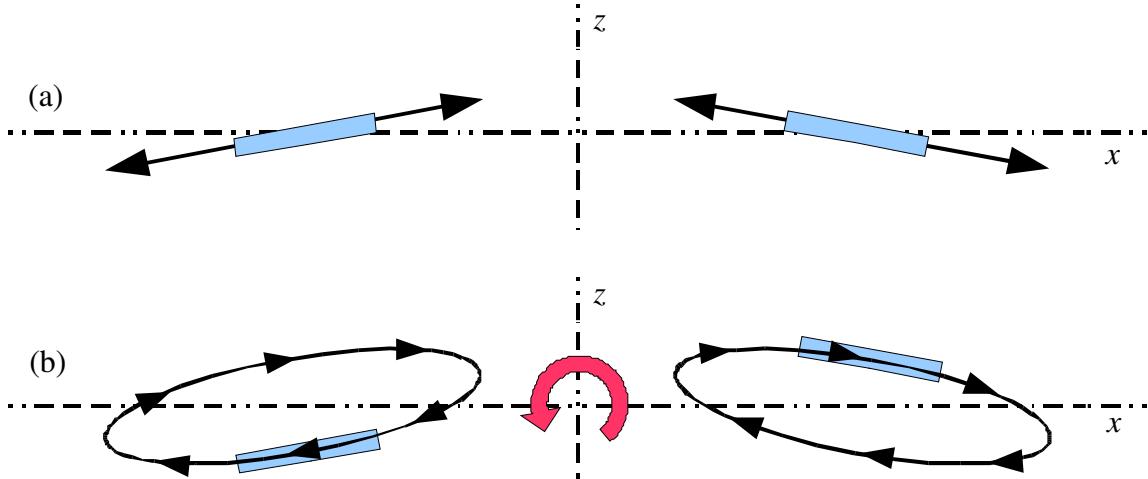


Fig. 55. Schematic of TFG running with quadrature error: (a) no input rotation, (b) input rotation.

The sense direction ($z$) motion of the proof masses caused by the quadrature error is interpreted as a Coriolis effect, or an artificial rotation. This results in a non-zero bias voltage in the form of a ZRO. Quadrature might be caused by mass imbalances or flexure springs with a minimum bending moment not in the drive plane, causing a resonance such as that shown in Fig. 55(a). It is also hypothesized that a non-planar chip causes quadrature error. Due to CTE mismatch there is residual thermomechanical stress

in a packaged sensor, which distorts the chip. The curvature in the chip is not constant over time or temperature, adding complexity into compensation for quadrature error.

## 5.2. Packaging of TFG

A major concern for the realization of high precision, low cost, inertial sensors is the packaging of the components. High quality inertial sensors perform better in vacuum environments (Marinis and Soucy, 2003). This is due to the increase in $Q$-factor as the pressure inside the package decreases. Wafer level packaging has produced systems with a $Q$-factor in the range of 3,000, which is acceptable for consumer products (Choa, 2005). Such packaging is performed by anodic bonding prior to dicing. However, Q-factor of inertial MEMS sensors for high performance military applications can be on the order of 1,000,000 (Pryputniewicz, 2008). In military applications pressures inside the package are on the order of 10 milli-Torr or better (Marinis and Soucy, 2003). This is the threshold at which atmospheric damping is no longer a dominating influence on the $Q$-factor.

In order to achieve this level of vacuum the packaging is performed in alumina 20-lead chip carrier. The lid is attached by brazing with AuSn eutectic after a thorough cleaning of the package, die, and lid (Marinis and Soucy, 2003). Getter material is also used in the package to maintain the integrity of vacuum over extended time. Ideally measurements would be made on a typical gyroscope; however the metal lid prevents measurements inside the vacuum sealed package. Special considerations have been made to allow for optical investigation of MEMS components in the high vacuum environment

by using a glass lid in place of the typical metal lid, as described by Marinis et al. (2008b). An example of a MEMS TFG packaged in a high vacuum environment with a glass lid is shown in Fig. 56.
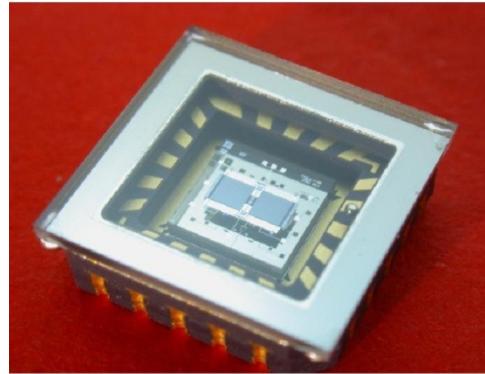


Fig. 56. Vacuum sealed MEMS gyroscope with glass lid.

In addition to the environment there are other concerns with regard to packaging. In particular, the MEMS die attachment. To maintain the high vacuum in the package two major techniques have been adopted; AuSn eutectic braze of the die to the package and thermocompression gold bump bonding (Hanson at al., 2001). Both methods require bonding of the die at elevated temperature (>300ºC), which leads to residual thermomechanical stress after cooling to room temperature (Marinis et al., 2006, Marinis et al., 2008a).

Gyroscopes are fabricated with silicon on insulator (SOI) technology, then anodically bonded onto a Hoya SD-2 glass substrate. The package, an alumina chip carrier, is prepared for packaging by a thorough cleaning, and then placing gold bumps onto the floor of the package cavity using a wire bonder machine. The number and placement of the bumps is variable, for most of the examples presented in this study 9

bumps in a 3 x 3 grid are used, however some components use four or 25 bumps.  Next, the entire system of the package and the MEMS on glass is heated to approximately 325ºC and the die is placed on the bumps with a load of 60 grams per bump, causing a gold thermo compression bond between the package and MEMS chip.  While cooling to ambient conditions the CTE mismatch between the materials results in a bowing of the MEMS chip, schematically shown in Fig. 57, where $w$ is the thickness of the chip, $L$ is the maximum distance between bump bonds, $h$ is the height of the bump bond, and $F$ is the force at the bump-chip interface.
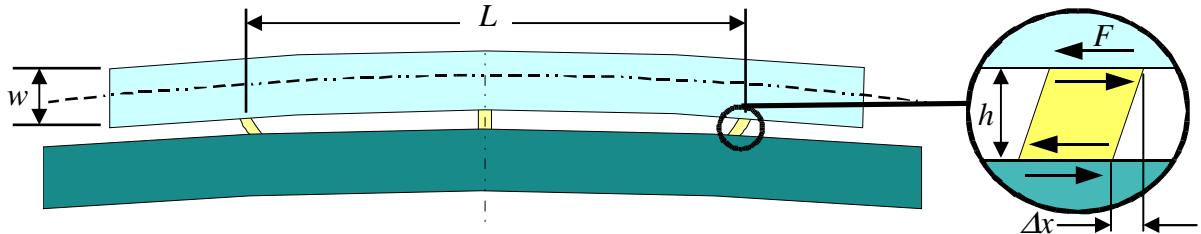


Fig. 57.  Schematic of deformed MEMS chip after packaging.

The full system may be modeled in an FEA package to simulate cooling from the initial bond temperature to an ambient temperature.  The construction of the model is shown in Fig. 58.  The dimensions are typical values for placement of die bonds, however the size and position of the bumps are variable in the parametric model allowing for rapid adjustment.
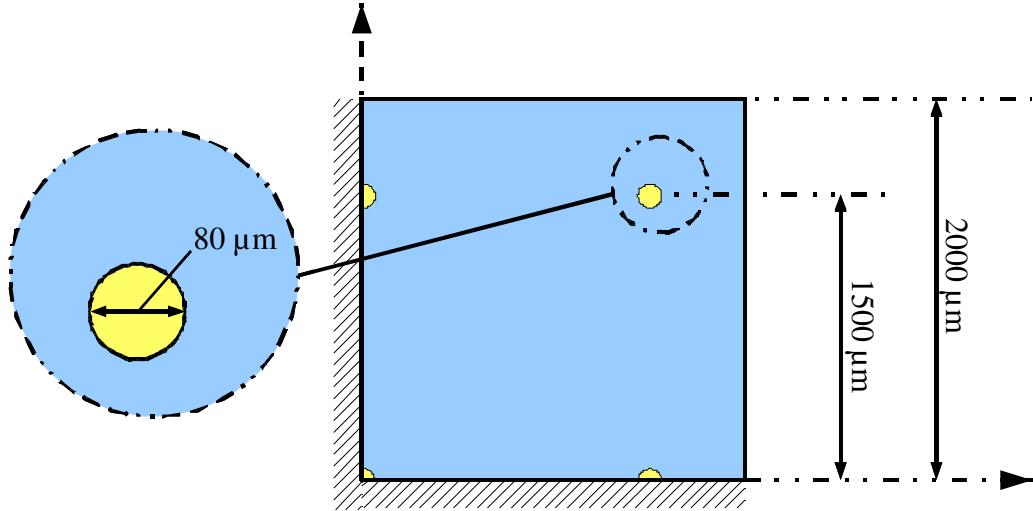
Fig. 58. Construction of the finite element model.

A three dimensional mesh, shown in Fig. 59, is generated in Gmsh, an open source finite element mesh generator (Gmsh, 2008). The package dimensions are based on direct measurements of the custom chip carrier.
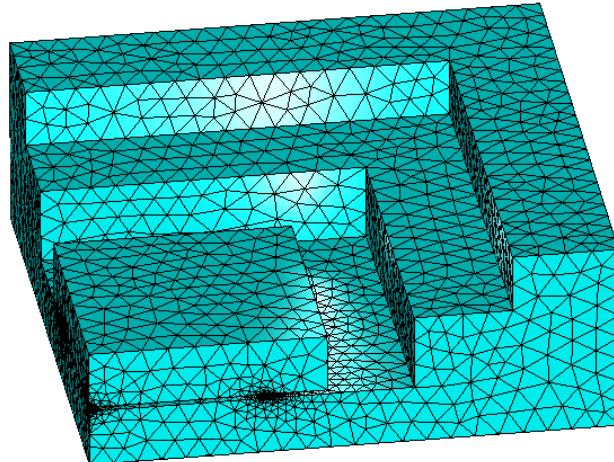


Fig. 59. Meshed model of die bonded into chip carrier; nine bump configuration.

The open source package Elmer FEA has been used for simulations, following a linear elastic equation set (Elmer, 2008). The model consists of three materials, alumina for the

chip carrier, gold for the bump bonds, and Hoya SD-2 glass for the chip. The properties used in the model for these materials are summarized in Table 1.

Table 1. Material properties used in FEA model.

|  | Material | $\rho$, [g/cm$^3$] | E, Gpa | $\alpha$, ppm/°C |
|---|---|---|---|---|
| **Chip** | Hoya SD-2 | 2600 | 86.9 | 3.2 |
| **Bump** | Gold | 19300 | 78 | 14.2 |
| **Substrate** | Alumina | 3900 | 375 | 8.4 |

The initial state of the model is at the bond temperature (325°C) and the steady state solution is at approximately ambient conditions of 25°C. The full field of view solution, with the color map corresponding to the displacement in the Z-direction (normal to the chip) is shown in Fig. 60.
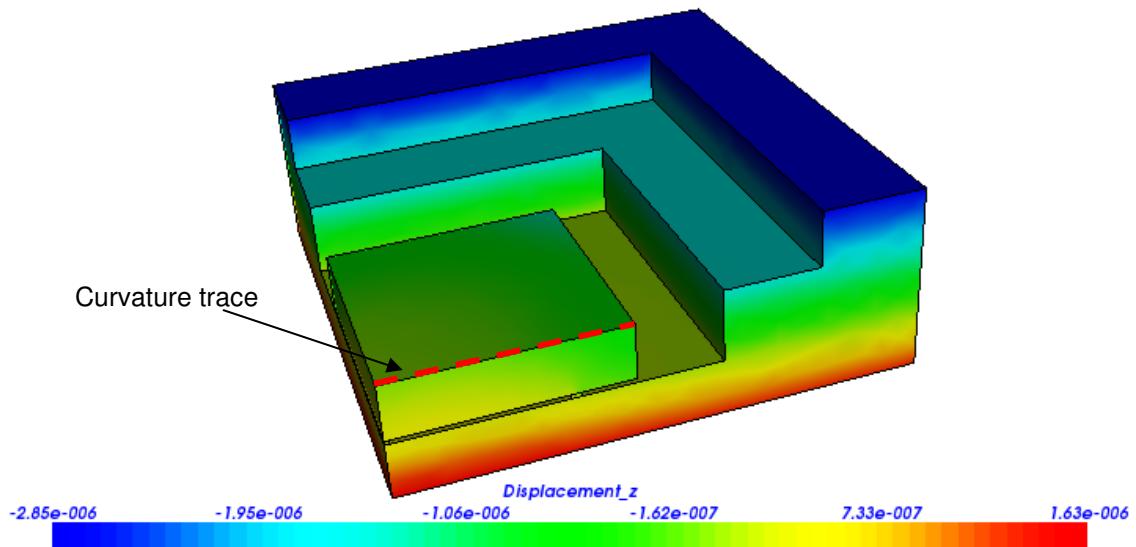


Fig. 60. Elmer FEA result for $\Delta T$ = -300°C, displacement in $Z$.

The curvature of the chip is more clearly represented by plotting the nodal displacements across the center of the chip, Fig. 61.
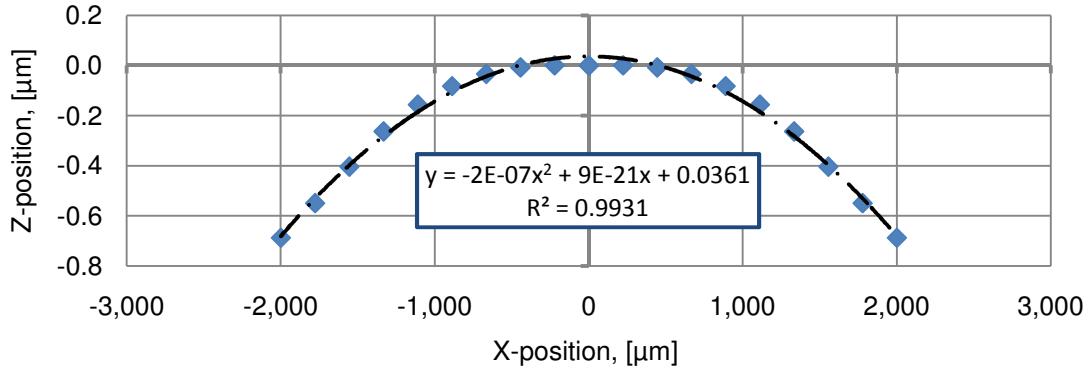
Fig. 61.  Nodal displacements of FEA simulation, ΔT=-300°C.

The data has been mirrored over the *X=0* (symmetry) axis to present the displacements over the entire chip center.  This is useful to ensure the appropriate condition (slope = 0) at the center of the chip when fitting a function to the data points.  The second order polynomial fit, via least squared method, describes the curvature through the points.

The curvature of a trace (or surface) is useful in quantifying the deformation present in a chip.  The curvature, $\kappa$, of a single function, $y(x)$, is defined as

$$\kappa(x) = \frac{|\ddot{y}|}{\left|(1 + \dot{y}^2)^{\frac{3}{2}}\right|} \, ,$$  (34)

where $\dot{y}$ and $\ddot{y}$ are the first and second derivative of $y(x)$, respectively (Hibbeler, 2000).  Equation 34 represents a point wise curvature over an entire trace, however when the slope ($\dot{y}$) is small Eq. 34 is approximated as

$$\kappa \approx \frac{\partial^2 y}{\partial x^2} .$$  (35)

The approximation of curvature is useful in comparing different line traces from FEA analyses or experimentally measured data.

This procedure is expanded to consider surfaces by way of the Gaussian curvature, ρ, which is defined as the product of the principal curvatures $\kappa_x$ and $\kappa_y$ as

$$\rho = \kappa_x \kappa_y. \tag{36}$$

For FEA simulations the principal curvatures, $\kappa_x$ and $\kappa_y$, are identical due to symmetry. Surfaces which are directly measured require calculation of each principal curvature independently.

The stresses that cause these deformations have been investigated using moiré interferometry on the entire package in wafer level packaging cases by Joo and Choa (2007). Alternatively, an OELIM may be used to directly measure the MEMS sensor (Pryputniewicz et al., 2003). With the use of a compensation glass in the reference beam it is possible to measure the shape of a sensor in a vacuum package with a glass lid, such as the device in Fig. 56.

### 5.3. Devices of interest

To demonstrate the capabilities of the interferometer and software developed, representative results are presented for measurements made on MEMS based TFG samples. Of particular interest is the shape of the substrate and device, which is distorted during the fabrication and packaging process. Many of these components are fabricated without an upper sense plate (USP). The USP is an electrode above the TFG structure which completes a second capacitive sensor between the top of the proof mass and the USP.

Three different structures have been studied during this research. The different test articles have been provided by sponsors throughout the duration of this work. Each geometry variation is described in the following sections. During the description of experiments, along with results, the specific TFG geometry, which was tested, is referenced by a nomenclature identifying each sample.

The naming scheme followed throughout will identify the TFG configuration and sample identification. Specifically, all test articles will be given a name of the form TFG-$\#_1.\#_2.\#_3$, where $\#_1$ indicates the general structure, $\#_2$ indicates the die bond type, and $\#_3$ represents the sample number. Details of the geometries are presented in sections 5.3.1 through 5.3.3, as well as summarized in the table located in Appendix C.

### 5.3.1.  TFG-1 configuration

The first TFG configuration that was investigated is that shown in Fig. 62. The fabrication of this device is described by Weinberg and Kourepenis (2006).
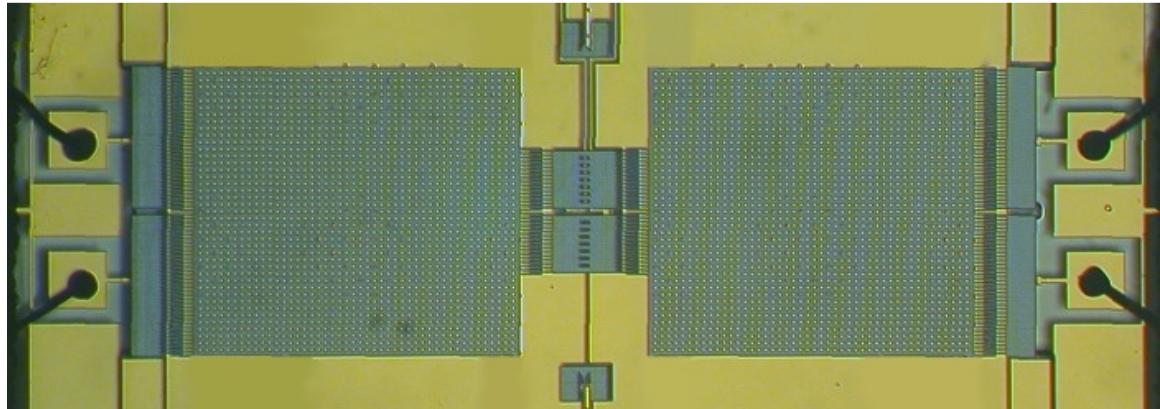


Fig. 62.  MEMS TFG, springs masked off image.

The flexure support springs have been masked off from the image in Fig. 62 as requested by sponsors. The removal of these springs does not affect any of the results presented herein, which will be based on proof masses and the substrate of the gyroscope. These devices are fully functional TFGs, mounted on a circuit board, Fig. 63, allowing for actuation of the proof masses. The glass lid allows for optical inspection of the device while maintaining a vacuum environment. The die is attached with nine gold bump bonds.
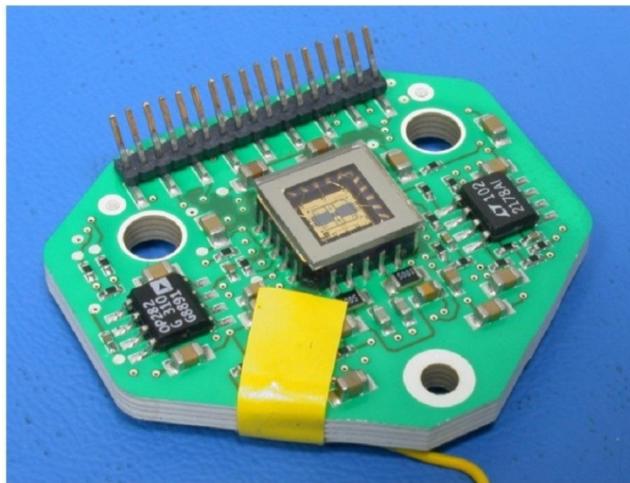


Fig. 63.  MEMS TFG mounted on board with electronics.

There are three functional gyroscopes of this configuration considered in this work, from this point further they will be identified as TFG-1.1.1 through TFG-1.1.3.

### 5.3.2.  TFG-2 configuration

The second configuration of gyroscope investigated in this work is shown in Fig. 64. This component is complete with the USP in place. The samples are for mechanical investigation only, the gyroscopes are not functional. Also, there is not a vacuum

environment in the package. The devices were constructed for investigation into the effects that high acceleration loads might have on the mechanical shape. In military applications these structures must be capable of surviving accelerations in excess of 20,000 g's (Karnick et al., 2004). The USP interferes with direct measurement of the MEMS surface; however measurements are made directly on the USP surface.
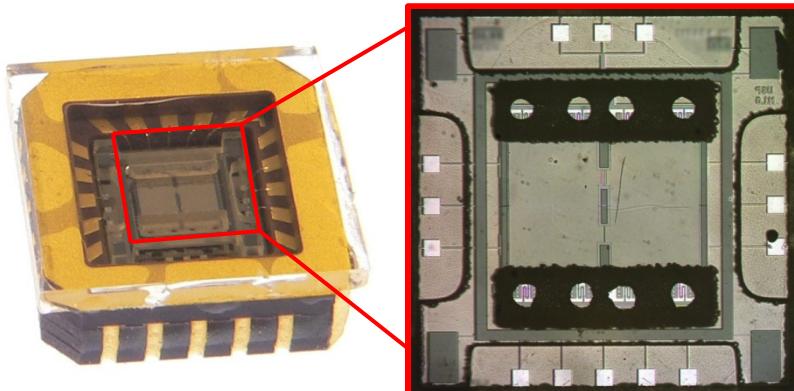


Fig. 64. TFG-2 Gyroscope with upper sense plate.

The USP is fabricated from SD-2 glass with metallization in the areas of the electrodes. The region of the USP is clearly shown in Fig. 65, where the red tinted region shows the USP glass and the blue shaded region shows the electrodes above the proof masses.
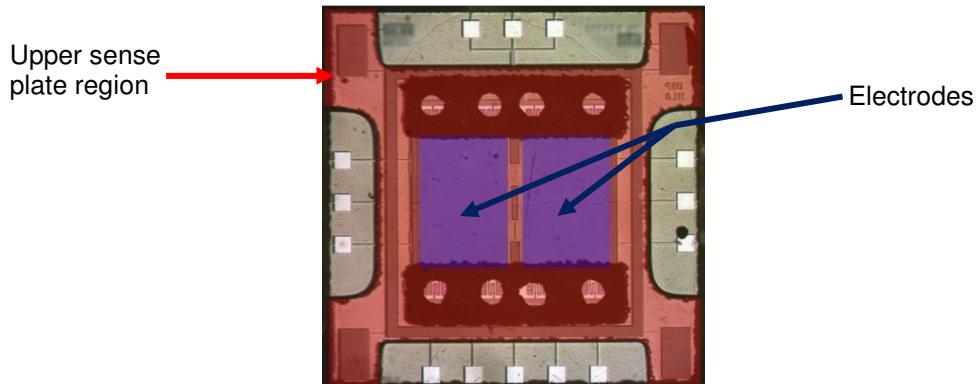


Fig. 65. Gyroscope with USP and shading to distinguish structures.

The die attachment was treated as a variable for these devices since components have been provided with a AuSn braze die attachment, 9-bump compression bond, and 25-bump compression bond.

A total of 18 components of this geometry have been investigated throughout this work, six components for each of the die attachment techniques. The braze die attach components will be referred to as TFG-2.1.1 through TFG-2.1.6, the 9-bump die attachment will be referred to as TFG-2.2.1 through TFG-2.2.6, and the 25-bump die attachment test articles will be referred to as TFG-2.3.1 through TFG-2.3.6.

### 5.3.3. TFG-3 configuration

The third TFG which was studied for relaxation of die bonds is a similar die to the previous component except no USP has been attached. These device are attached with four compression bonds, in two configurations. X-ray images show the placement of the compression bonds, Fig. 66.
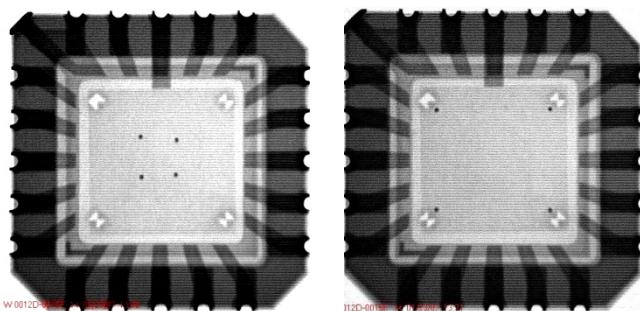


Fig. 66. X-ray images of compression bump positions: (left) bumps close together, (right) bumps spread far apart.

These test articles were provided as strictly mechanical samples, therefore no vacuum or package lid are required. Surrounding the TFG structure is a frame, metalized

directly on the substrate glass. Measurements are made on the frame with traces

extracted to reveal curvature. The packaged sample, along with a microscope image of

the sensor, is shown in Fig. 67.
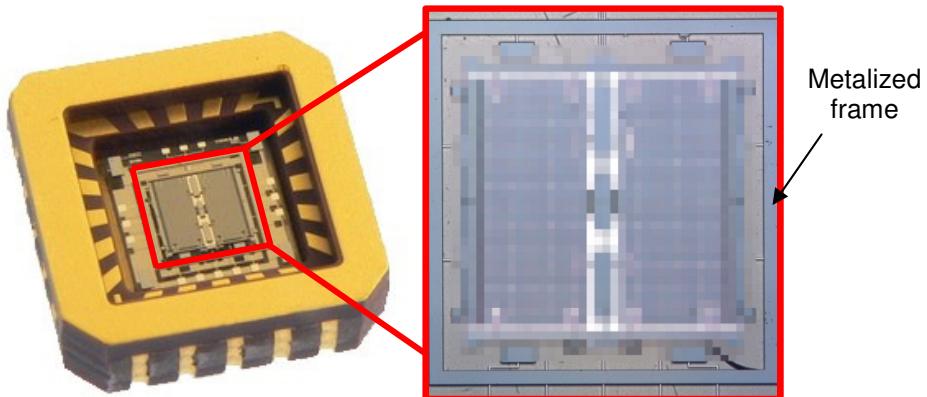


Fig. 67. Tuning fork gyroscope with 4-bump attachment, metalized frame.

A total of six components of this type are investigated, three of each bump

configuration. The three components with bumps close together will be referred to as

TFG-3.1.1 through TFG-3.1.3 and the three components with the bumps spread far apart

will be referred to as TFG-3.2.1 through TFG3.2.3.

# 6. CASE STUDY OF MEMS TFG

The automated interferometer serves as a versatile metrology tool, suited for direct shape measurements of microelectronic components under a variety of conditions. Scripting capabilities are integrated within the software interface, allowing for execution of measurement processes which are not practical or possible with purely manual operation in a highly interactive manner. The motivation for the development of an automated interferometer was driven by the need to characterize the shape of MEMS TFG components as a function of temperature and thermal cycle. Currently there are no commercially available solutions, all systems have limitations in the realm of thermal loading within a chamber.

Throughout the design of the automation system additional features, such as the scripted phase scanning measurements made during stroboscopic illumination for dynamic analysis, have been implemented. Based on the modular architecture of the interface it is possible to continually add measurement modules or processes without a dramatic redesign of the interface.

The following sections serve to demonstrate various capabilities of the interferometer and software. The presented results are representative of the tests that have been performed on MEMS TFG components. In most cases an experiment is designed to first determine if an effect is observed due to some process; for example, if thermal loading leads to curvature change. If an effect is observed, then further investigation is performed to characterize the behavior or determine the real world

consequences. In cases where no effect is observed (the null hypothesis holds true) the example only demonstrates the specific capability of the measurement system.

Although all the presented tests are based on MEMS TFG components, the measurement system is not exclusive to these geometries. Similar methodologies are possible on a variety of MEMS components, including cantilever devices, pressure sensors, and accelerometers.

The underlying theme in the tests performed is the investigation into the effects of packaging on the performance of the components. Specifically, it is believed that the die attachment process leads to some degree of chip curvature which will influence the performance of the device. The chip curvature might be a function of both temperature and time, making compensation for the effects difficult.

## 6.1. Thermal effects on TFG

A major area of research has been in the thermal stability of MEMS devices. In field applications the temperature might not be accurately controlled, however correction factors are required for compensation. As discussed in section 5.2 there is a thermomechanical residual stress present in the die after packaging. The shear stress in the bump bond has a reaction stress on the bottom surface of the die, generating a bending moment which results in a curvature. As the temperature increases towards the bond temperature the curvature reduces.

Two different test article configurations are presented with respect to thermal effects, TFG-1 and TFG-3.

### 6.1.1.  TFG-1 configuration

The most direct measurement of the MEMS are those made on the structure itself (Pryputniewicz et al., 2003).  The proof masses are connected by spring flexures, providing a single surface for unwrapping analysis.  The high reflectivity of the MEMS is well suited for Twyman-Green measurements.  A representative fringe pattern on a TFG-1 component is shown in Fig. 68.
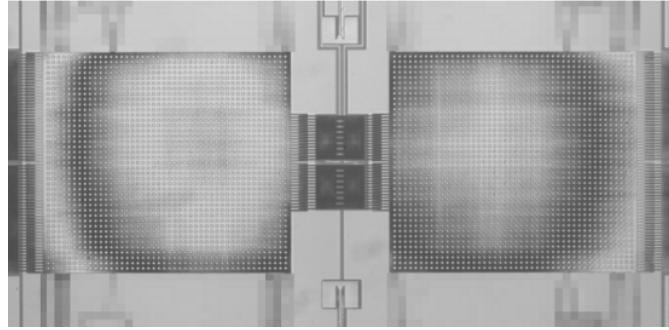


Fig. 68.  Fringe pattern on TFG-1 test article.

The sample is placed in the thermal loading chamber and shape measurements are made at five thermal states, ranging from 5-85ºC in 20ºC increments.  A thermal soak of 20 minutes is performed before a measurement is made.  The analyzed proof mass shapes are shown at the extreme temperature states for TFG-1.1.1 in Fig. 69.
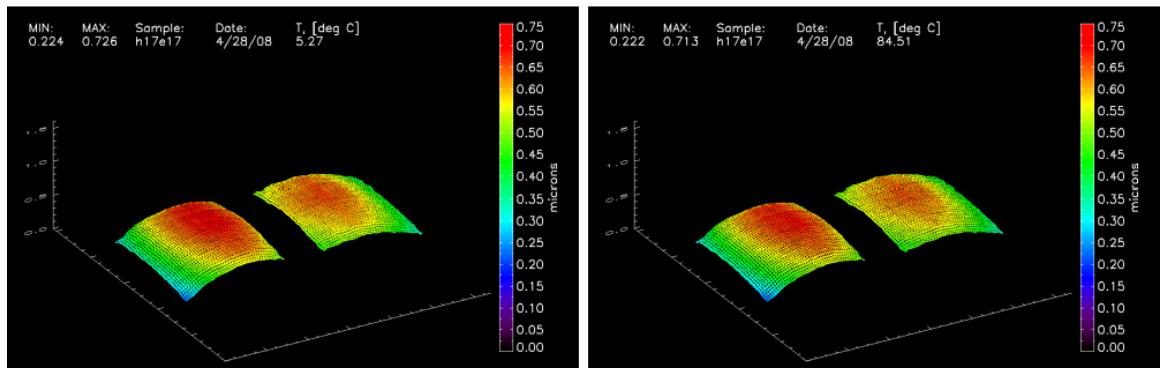


Fig. 69.  Proof mass shapes of TFG-1.1.1 at extreme temperature states.

There is little discernable difference in the full field of view results, however a lateral line trace extracted through the center of the proof masses might more clearly show the differences. The traces are shown relative to the low temperature (5ºC) measurement to highlight changes. A maximum change of approximately 25 nm is observed at the high temperature (85ºC) state, relative to 5ºC, Fig. 70.
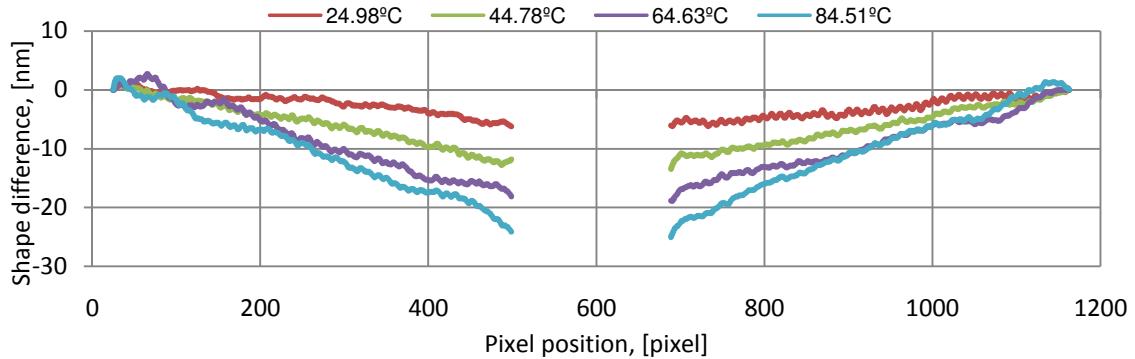


Fig. 70. Differential central line traces of TFG-1.1.1 sample at different thermal states, relative to 5ºC measurement.

The differential traces appear linear, suggesting a rigid body tilt of the proof masses at different temperatures. A change in shape of the substrate would suggest such a deformation. The proof masses are supported by flexures that are affixed to rigid posts off the substrate. By using alternative methods the substrate is directly measured for shape as a function of temperature. The interferometer is adjusted such that fringe modulation is on the substrate rather than the MEMS structure, Fig. 71 (a). The MEMS structure is masked off such that only the regions of the substrate are visible. At this point the surface is not continuous; unwrapping will only analyze a single region. All of

the discrete sections are linked by drawing traces on each of the five phase steps. The traces must modulate so as not to be removed by a low modulation filter.
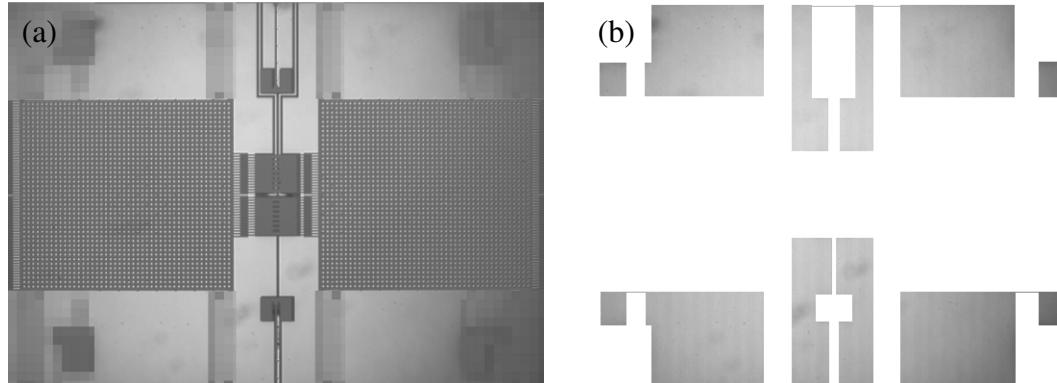


Fig. 71. Modulation on the substrate of a TFG chip: (a) full image, (b) image masked with discrete areas linked.

Measurements of the TFG substrate are made following the same procedure as the MEMS structure. Analyzed results are shown for the extreme temperature states, Fig. 70.
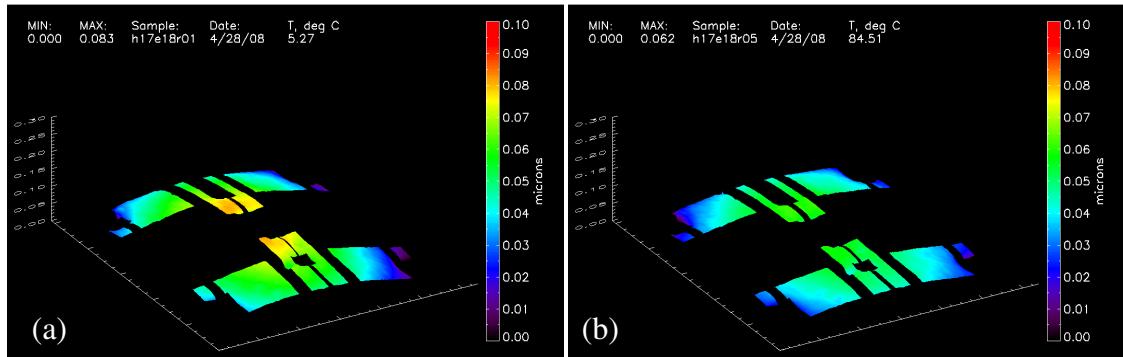


Fig. 72. Substrate shapes at extreme temperature states: (a) 5.27ºC, (b) 84.51ºC.

Qualitatively there appears to be a shape difference between the two thermal states. Extracting a lateral data trace through the center of the measurement is not possible for these measurements as that region has been masked. An alternative analysis method is proposed, fitting the second order surface to the data for quantitative analysis

of measurements.  A mathematical representation of a substrate is obtained by fitting an equation of the form

$$Z(x, y) = A + By + Cy^2 + Dx + Exy + Fx^2 ,$$   (37)

where the $2^{nd}$ order surface coefficients $A, B, C, D, E,$ and $F$ are obtained from the least squares fit of the surface.  During the analysis in-plane scaling is performed such that all units for the surface fit to the data, $Z$, are in micrometers.  Measurements are made on the substrate at temperatures ranging from 5-85ºC.  The surface coefficients are outlined in Table 2.  The coefficients of particular interest are $C$ and $F$, which correspond to the $2^{nd}$ order terms in $y$ and $x$ directions, respectively.  Changes in these terms indicate deformation, rather than rigid body motion.

Table 2. Coefficients for the $2^{nd}$ order surface fit to substrate, TFG-1.1.1.

| T, ºC | A | B | C | D | E | F |
|-------|-----|-----|-----|-----|-----|-----|
| 5.27 | -1.89E-02 | 5.94E-05 | -2.35E-08 | 7.51E-05 | 4.07E-09 | -2.66E-08 |
| 24.98 | -1.93E-02 | 5.21E-05 | -2.18E-08 | 7.46E-05 | 4.27E-09 | -2.48E-08 |
| 44.78 | 3.00E-02 | 2.48E-05 | -1.82E-08 | 6.67E-05 | 3.99E-09 | -2.25E-08 |
| 64.63 | -3.08E-03 | 3.36E-05 | -1.63E-08 | 6.84E-05 | 3.79E-09 | -2.07E-08 |
| 84.51 | -1.10E-02 | 3.29E-05 | -1.35E-08 | 5.78E-05 | 2.81E-09 | -1.83E-08 |

The decreasing values for $C$ and $F$ show that curvature is reducing as temperature increases, in agreement with Fig. 72.  Lateral traces extracted through the center of the fit surfaces are shown in Fig. 73.
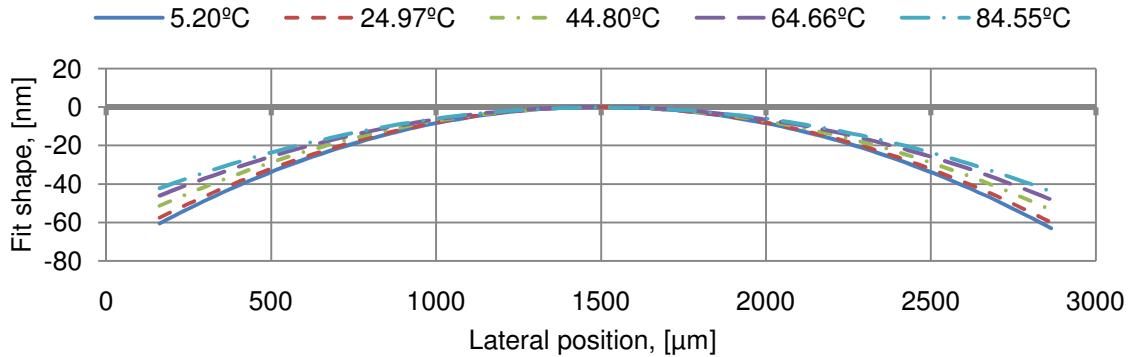
Fig. 73. Central line traces through substrate fit of TFG-1.1.1 sample at different temperatures.

There is a clear change in the shape of the traces through the fit surface of the substrate. This trend is more clearly shown by displaying the traces after subtracting the 5ºC trace as a reference. This plot, Fig. 74, shows the deformations relative to the most curved (coldest) state.
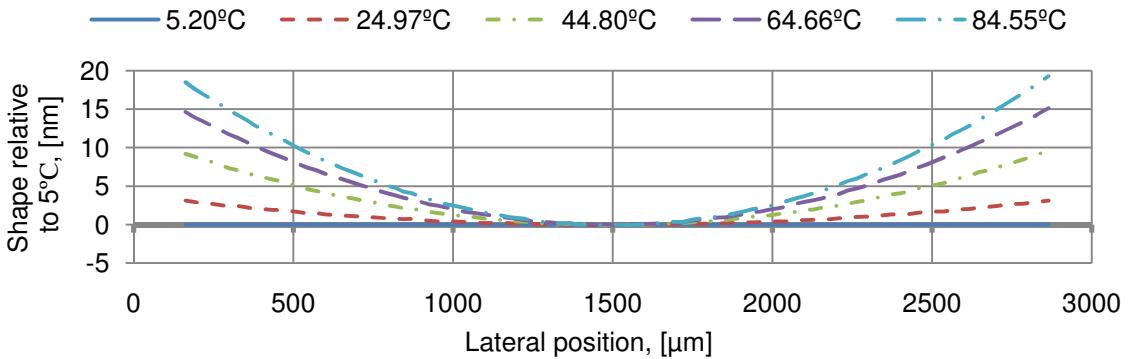


Fig. 74. Deformation of the substrate fit due to thermal loads, TFG-1.1.1.

The plot of deformations shows that there is an elevation change of nearly 20 µm from the edge of the substrate to the center. This is similar in magnitude to the tilt of the proof masses, shown in Fig. 70, suggesting that the changes visualized in the proof

masses are actually due to the deformation of the substrate, rather than deformations of the proof masses themselves.

A final test to determine if there are deformations, or only rigid body motions, in the proof masses is to track the degree of shape chance in proof mass as a function of temperature. The shape of the proof masses is mathematically modeled as the $2^{nd}$ order surface. To demonstrate the quality of fit for this approximation Fig. 75 displays the data directly extracted from the measurement in a dashed blue trace, and the $2^{nd}$ order fit is shown in the continuous red trace.
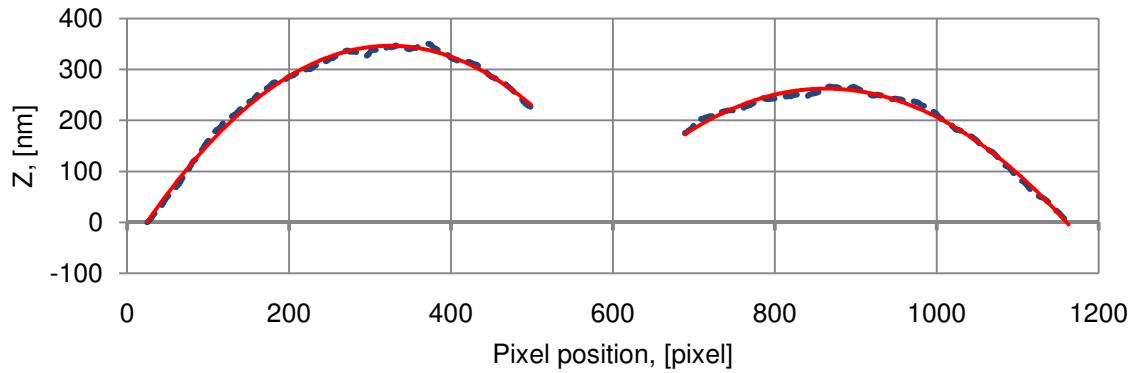


Fig. 75. Demonstration of quadratic fit to proof mass shape.

The curvatures of the proof mass surface models are calculated as a function of temperature. The percent reduction in curvature as a function of temperature is represented in the bar graph, Fig. 76, showing virtually no change in the shape of the proof masses, corroborating the hypothesis that the changes in the traces of Fig. 70 are rigid body tilts of the proof masses caused by a deforming substrate.

114
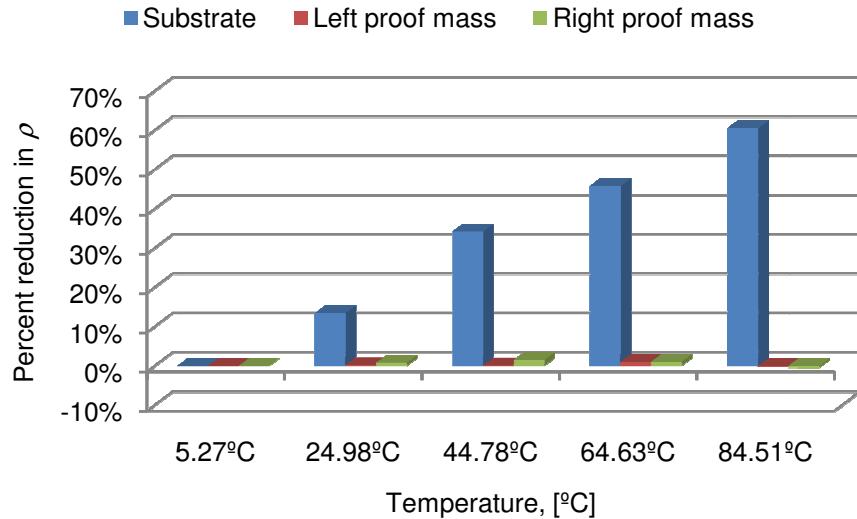
Fig. 76. Thermally induced reductions of curvature in the substrate and proof masses.

The potential effects of the substrate curvature, and the deformation with respect to temperature, is quantified by integrating between the surfaces of the proof mass and the substrate,

$$A_{LPM} = \int_{x_1}^{x_2} \left(f_{LPM}(x) - f_{sub}(x)\right) dx \,, \tag{38}$$

where $A_{LPM}$ is the area under the left proof mass trace, $f_{LPM}(x)$ is the analytical function describing the left proof mass trace, $f_{sub}(x)$ is the quadratic function of the substrate trace, and $x_1$ and $x_2$ are the extremes of the proof mass. The average gap distance is obtained by dividing the calculated area between the curves by the width of the proof mass.

The preliminary analytical model is based on the curvature decrease in the substrate. It has been shown that the percentage shape change in the proof masses is very small in comparison to the substrate. Because there is little deformation in the proof masses they are modeled as linear functions to simplify calculations. For integration a

115

line equation is used to model the proof masses, passing through points set at a constant, nominal offset above the substrate at the endpoints of the proof masses. The constant offset is the ideal case of the edges of the proof mass at the same elevation as the posts, assuming no deformations in the spring flexures. A plot of the linear model of the proof masses, offset from the substrate model by 50 nm at the edges, is shown in Fig. 77. Results of the integration, relative to the 5ºC state, between the proof masses (modeled as linear functions) and the substrate are presented in Table 3. As expected, the average gap distance increases with temperature, as the curvature in the substrate decreases. In devices the gap distance is on the order of 3 µm, however very small nominal gap distances are used in the calculations for display purposes. By examining changes in the gap distance, relative to the 5ºC state, the magnitude of the nominal gap distance becomes irrelevant.
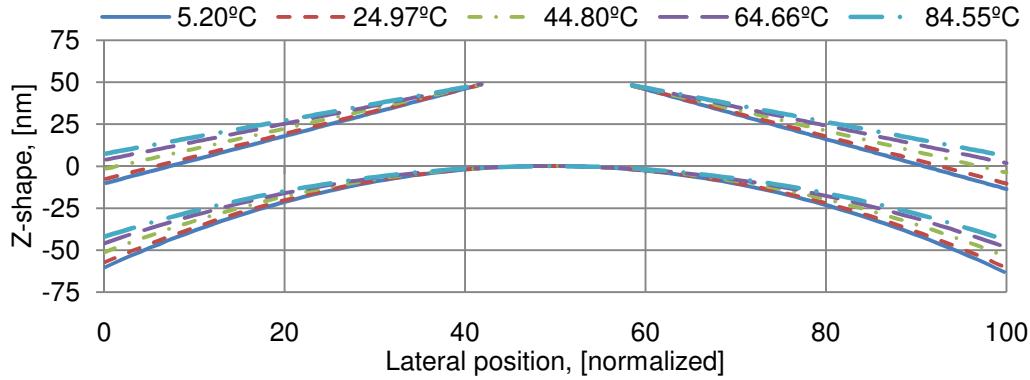


Fig. 77. Linear model of proof masses offset nominal distance from substrate.

Table 3. Change in average gap distance relative to 5ºC for TFG-1.1.1.

|  | 5.20ºC | 24.97ºC | 44.80ºC | 64.66ºC | 84.55ºC |
|---|---|---|---|---|---|
| $\Delta d_{gap,L}$, [nm] | 0.000 | 0.358 | 1.090 | 1.800 | 2.236 |
| $\Delta d_{gap,R}$, [nm] | 0.000 | 0.117 | 0.843 | 1.475 | 2.015 |

116

Using the PSI measurement technique it is not possible to measure the proof mass surface and the substrate simultaneously, however it is possible to measure each surface independently with no tilt adjustments made between recordings. The reference mirror position is adjusted to focus modulation on the different surfaces for each recording. During analysis a nominal offset is applied between a post, which is connected to the proof masses through the spring flexures, and the substrate. The offset is applied between the points, labeled $p_1$ and $p_2$ in Fig. 78.
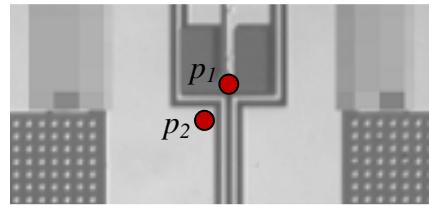


Fig. 78. Points used to apply nominal offset between proof masses and substrate.

By linking the measurements made on the proof mass and the substrate by an offset of 0.1 μm, trace made through the mathematical model of the proof masses is added to Fig. 73, resulting in Fig. 79.
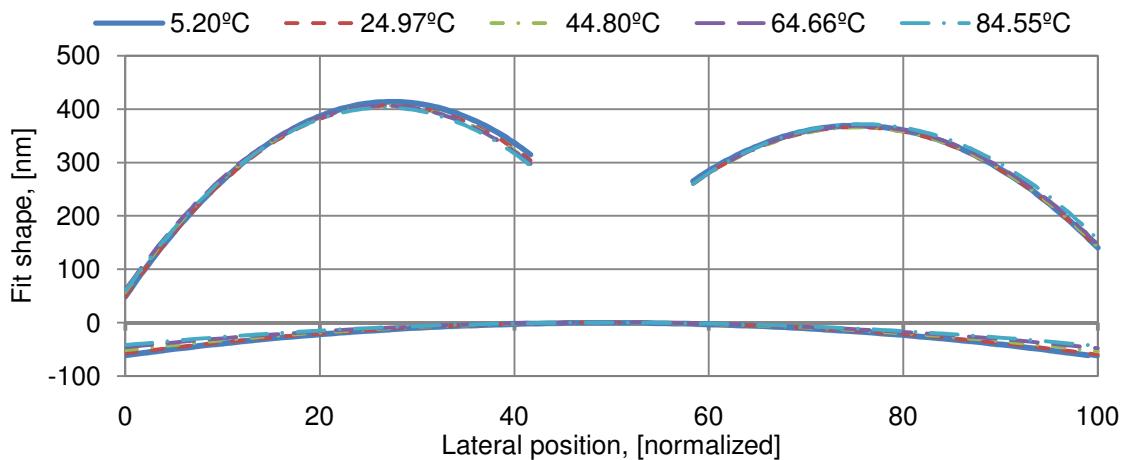


Fig. 79. Central line traces through analytical surface models of the substrate and proof masses, TFG-1.1.1.

The small deformations in the shape of the substrate make it difficult to visually discern changes in the average gap distance; however the integration method applied while approximating the proof masses as linear functions is implemented. Furthermore, with the full shape of the proof masses known, the integration is expanded to a double integration,

$$d_{gap} = \frac{1}{A} \iint (f_{pm}(x,y) - f_{sub}(x,y)dA .$$ (39)

The integration is performed numerically using a MatLab script with the surface fit coefficients for the proof masses and substrate entered as input variables. The volume between the proof masses and the substrate is divided by the electrode area of the proof mass to determine the average gap distance. These values are gap distances relative to the nominal gap set between $p_1$ and $p_2$. The change in gap distance, $\Delta d_{gap}$, is determined by subtracting the first temperature state gap distance from subsequent measurements. This analysis has been performed on the three TFG-1 configuration gyroscopes, with results summarized in Table 4.

Table 4.  Change in gap distance as calculated by double integration method.

|  | TFG-1.1.1 | | TFG-1.1.2 | | TFG-1.1.3 | |
|---|---|---|---|---|---|---|
|  | $\Delta d_{gap,L}$ | $\Delta d_{gap,R}$ | $\Delta d_{gap,L}$ | $\Delta d_{gap,R}$ | $\Delta d_{gap,L}$ | $\Delta d_{gap,R}$ |
| 5ºC | 0.00 | 0.00 | 0.00 | 0.00 | 0.00 | 0.00 |
| 25ºC | -7.32 | -3.69 | 0.45 | 2.94 | -0.10 | 7.54 |
| 45ºC | -8.42 | -6.04 | 0.91 | 7.80 | 3.66 | 7.82 |
| 65ºC | -10.52 | -5.90 | 6.28 | 5.49 | 3.54 | 3.85 |
| 85ºC | -16.15 | -3.64 | 14.65 | 15.05 | 5.39 | 5.38 |

All values listed in Table 4 are in units of nanometers. The sample TFG-1.1.1, which was the basis for the linear proof mass approximation method, shows a discrepancy with results in Table 3. Not only is the magnitude in the gap distance change much larger, but the volume integration method indicates that the average gap distance is decreasing with temperature. This suggests that, approximating the proof masses as linear first order surfaces with the edges offset a nominal distance above the substrate is not a viable method for investigating changes in the sense gap due to substrate deformation. Both the substrate and the proof mass surfaces must be measured in order to obtain insight into potential changes in the sense gap distance.

### 6.1.2. TFG-2 configuration

Thermal loading has been performed on samples of the TFG-2 configuration for different methods of die attachment. The initial measurements show that braze die attachment has the highest amount of curvature, as shown in Fig. 80.
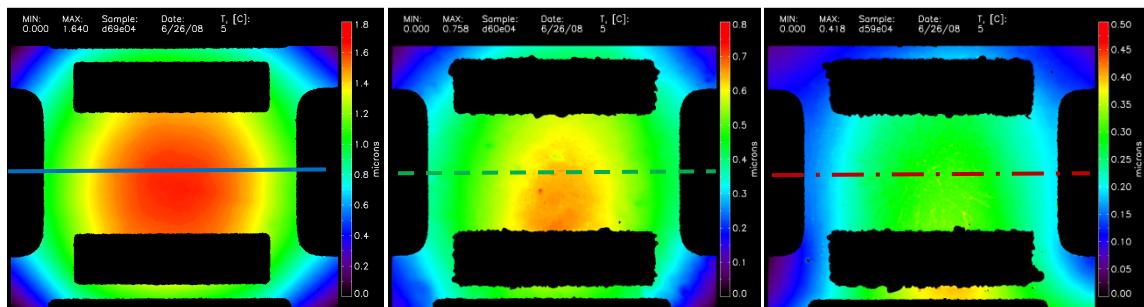


Fig. 80. Shape measurement of: (a) Braze (TFG-2.1.2), (b) 9-bump (TFG-2.2.2), and (c) 25-bump (TFG-2.3.2) configurations.

Lateral traces through the center of the USP glass show comparison of the curvatures of the components, Fig. 81.
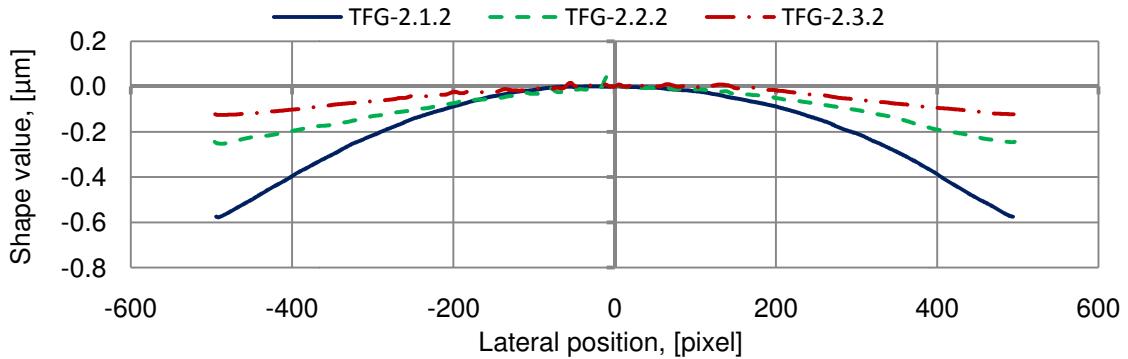
Fig. 81. Lateral traces through USP of TFG-2 configuration at 5ºC.

As observed on the TFG-1 components, curvature decreases as temperature increases. A total of nine TFG-2 components (three for each die bond method) have been measured at three different temperature states. The Gaussian curvature is determined at 5, 45, and 85ºC for each of the components, the braze curvature change is shown in Fig. 82.
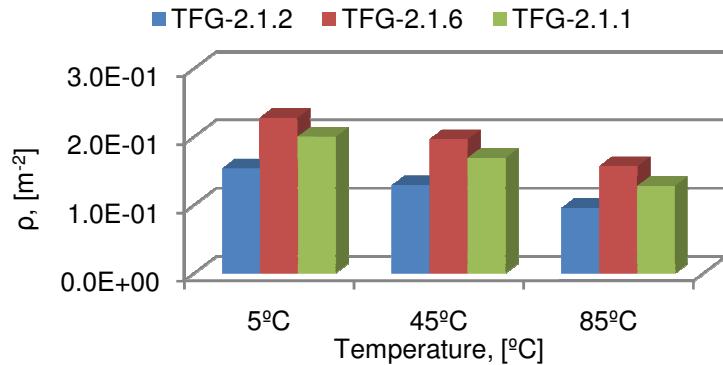


Fig. 82. Gaussian curvature reduction for TFG-2.1 (braze) configuration.

Tabulated values for Gaussian curvature ($\rho$) and the percent change with respect to the 5ºC measurement in Gaussian curvature ($\%\Delta\rho$) are given in Table 5.

Table 5. Summary of Gaussian curvature changes for TFG-2.1 (braze) configuration.

| | TFG-2.1.2 | | TFG-2.1.6 | | TFG-2.1.1 | |
|---|---|---|---|---|---|---|
| | ρ | %Δρ | ρ | %Δρ | ρ | %Δρ |
| **5ºC** | 1.53E-13 | 0.0% | 2.28E-13 | 0.0% | 2.00E-13 | 0.0% |
| **45ºC** | 1.29E-13 | -16.0% | 1.96E-13 | -13.8% | 1.69E-13 | -15.5% |
| **85ºC** | 9.59E-14 | -37.5% | 1.57E-13 | -31.1% | 1.28E-13 | -36.1% |

Both the magnitude and the reduction of the curvature is consistent for each of the braze

die attachment samples.

Similar results for the TFG-2.2 configuration, with 9-bump die attachment, are

presented in Fig. 83 and Table 6.
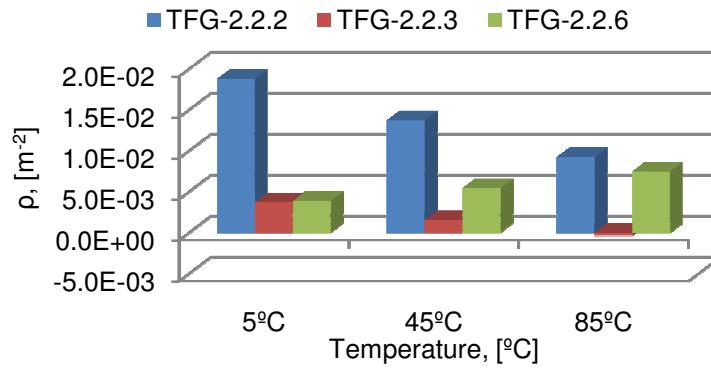


Fig. 83. Gaussian curvature reduction for TFG-2.2 (9-bump) configuration.

Table 6. Summary of Gaussian curvature changes for TFG-2.2 (9-bump) configuration.

| | TFG-2.2.2 | | TFG-2.2.3 | | TFG-2.2.6 | |
|---|---|---|---|---|---|---|
| | ρ | %Δρ | ρ | %Δρ | ρ | %Δρ |
| **5ºC** | 1.88E-14 | 0.0% | 3.71E-15 | 0.0% | 3.90E-15 | 0.0% |
| **45ºC** | 1.37E-14 | -26.8% | 1.52E-15 | -59.0% | 5.42E-15 | 39.0% |
| **85ºC** | 9.23E-15 | -50.8% | 3.41E-16 | -90.8% | 7.46E-15 | 91.3% |

It is of particular interest that TFG-2.2.6 has a curvature that increases with

temperature. The initial shape shows that the test article is concave up, while all other

components are concave down.  The analyzed shape map of TFG-2.2.3 and TFG-2.2.6 are shown in Fig. 84, to display the unusual shape.
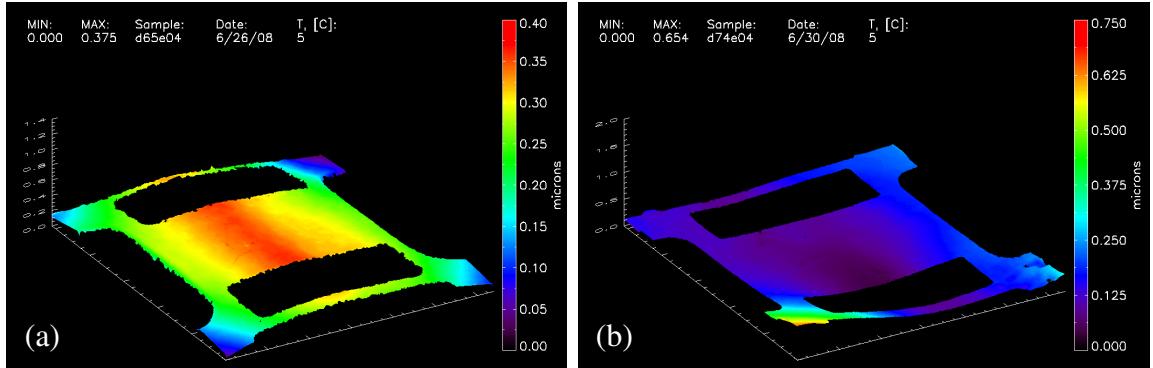


Fig. 84.  Shape at 5ºC of components: (a) TFG-2.2.3 and (b) TFG-2.2.6.

The TFG-2.3 configuration (25-bump) results are similar to those of the 9-bump samples.  The results of the shape measurements at different temperature are presented in Fig. 85 and Table 7.  Again the curvature generally decreases with temperature increase, however this is not the case with sample TFG-2.3.6, shown at the 5ºC state in Fig. 86.
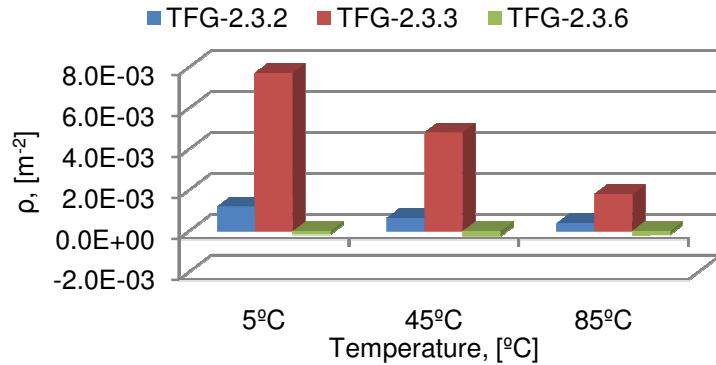


Fig. 85.  Gaussian curvature reduction for TFG-2.2 (25-bump) configuration.

Table 7.  Summary of Gaussian curvature changes for TFG-2.2 (25-bump) configuration.

| | TFG-2.3.2 | | TFG-2.3.3 | | TFG-2.3.6 | |
|---|---|---|---|---|---|---|
| | ρ | %Δρ | ρ | %Δρ | ρ | %Δρ |
| 5ºC | 1.19E-15 | 0.0% | 7.72E-15 | 0.0% | -1.70E-16 | 0.0% |
| 45ºC | 6.44E-16 | -46.0% | 4.82E-15 | -37.6% | -2.67E-16 | 57.0% |
| 85ºC | -3.77E-16 | -131.6% | 1.80E-15 | -76.7% | -1.78E-16 | 4.9% |
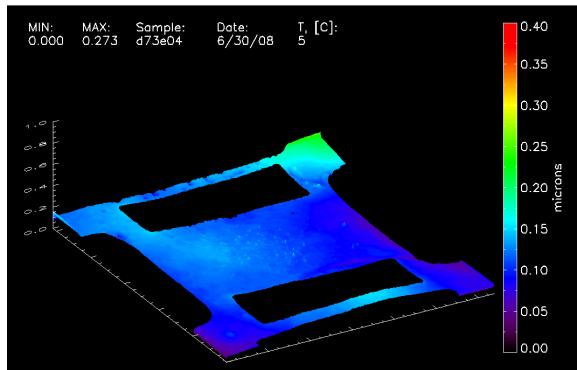


Fig. 86.  Shape of TFG-2.3.6 USP at 5ºC.

This sample possesses an initial distorted shape that might be due to manufacturing problems while bonding the USP and TFG glass.  The distorted shape is not a good fit to the second order polynomial; therefore the results of curvature calculated based on this assumption might be erroneous.

## 6.2.  Sense gap hysteresis

Static thermal shape is not be the only temperature dependence in TFG components.  There has also been a hysteretic effect observed with respect to thermal loading.  Specifically, the components behave differently during the temperature increasing and decreasing portions of a cycle.  It has been clearly shown that shape of the

MEMS (and substrate) are functions of temperature, it is possible that hysteresis is present in the deformation of a sensor.

A process has been developed in which the test article is placed within a temperature chamber subjecting the TFG to thermal cycling. Interferometric measurements are made at 45ºC during the rising and falling temperature cycle, which ranges from 5ºC to 85ºC. The process is similar to that described in section 4.1.4.6.1, an extra cycle has been added and the cold temperature limit is decreased. The experiment profile is shown in Fig. 87, where the red dots indicate measurement points.
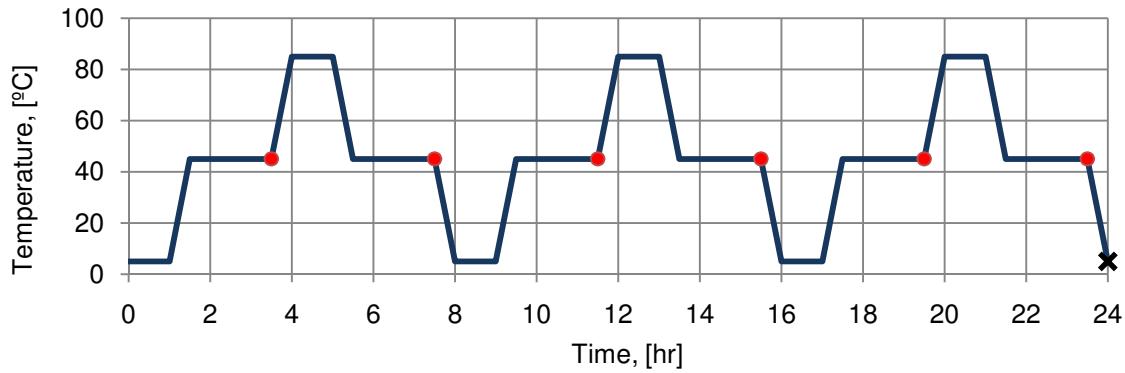


Fig. 87. Measurement profile for sense gap hysteresis test.

The total experiment, which requires 24 hours to complete, has been automated using the *User Defined Script* feature described in section 4.1.4.6.6. The profile, as entered into the software environment, is shown in Fig. 88.
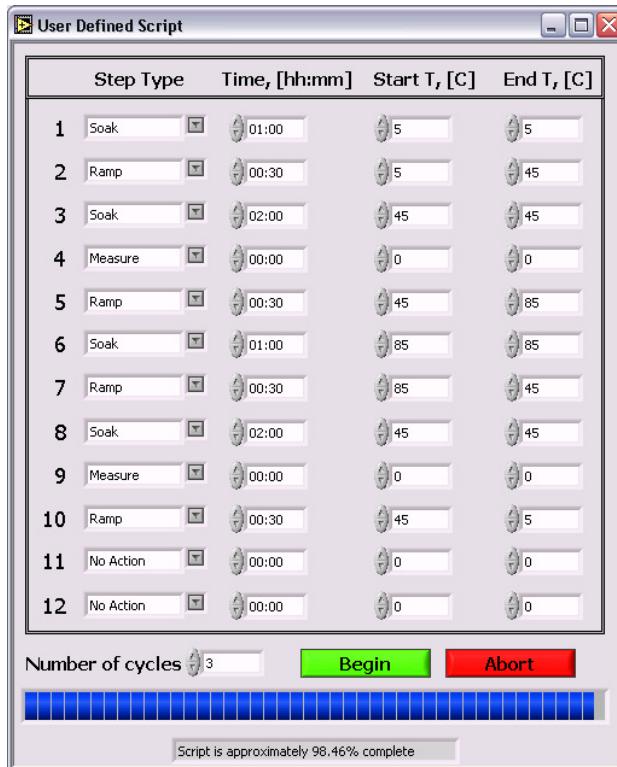
Fig. 88. Script definition for sense gap hysteresis experiment.

Demonstration of these capabilities is performed on the TFG-2.1.1 (braze), TFG-2.2.1 (9-bump), and TFG-2.3.1 (25-bump) samples. The measurements are made on the electrodes of the USP, shown in blue on Fig. 65. The shape is characterized by the Gaussian curvature calculated from the $2^{nd}$ order surface fit to the measurement. The surface map at the first measure point is shown for all three components in Fig. 89.

125
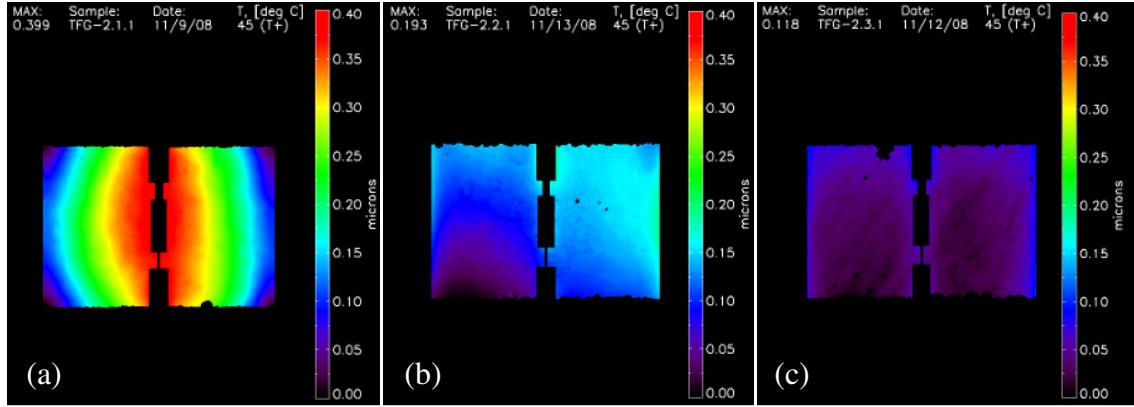
Fig. 89. Shape of USP electrode during gap hysteresis experiment: (a) TFG-2.1.1, (b) TFG-2.2.1, (c) TFG-2.3.1.

There are six measurements made during each test, three of which while the temperature is increasing, and three while decreasing. The second order surface parameters are determined by least squares method. The null hypothesis is that there is no change in the Gaussian curvature between the temperature increasing, T(+), and temperature decreasing, T(-), measurements. A t-test is applied between the increasing and decreasing recordings to determine if the measurements are statistically different. The Gaussian curvatures, and the statistical results, are summarized in Table 8, where *t* is the value for the test statistic, and *P* is the probability that there is no effect on the Gaussian curvature due to increasing/decreasing portion of the cycle.

Table 8.  Calculations based on gap hysteresis test for TFG-2 components.

| TFG-2.1.1 | | TFG-2.2.1 | | TFG-2.3.1 | |
|---|---|---|---|---|---|
| T(+) | T(-) | T(+) | T(-) | T(+) | T(-) |
| 9.29E-14 | 9.29E-14 | -8.1E-16 | -6.6E-16 | 2.04E-15 | 2.03E-15 |
| 9.24E-14 | 9.32E-14 | -7.7E-16 | -6.3E-16 | 1.80E-15 | 2.04E-15 |
| 9.15E-14 | 9.16E-14 | -7.4E-16 | -5.7E-16 | 2.18E-15 | 1.80E-15 |
| *t* = -0.42 | | *t* = -4.53 | | *t* = 0.37 | |
| *P* = 0.69 | | *P* = 0.01 | | *P* = 0.73 | |

The results show that there is no statistical hysteretic effect observed in the TFG-2.1.1 (braze) or TFG-2.3.1 (25-bump) samples. However, the probability of the T(+) and T(-) measurements for TFG-2.2.1(9-bump) are of the same distribution is low, suggesting a hysteresis in the substrate deformation. The Gaussian curvature for each of the measurements made on TFG-2.2.1 is plotted as a function of measurement number in Fig. 90. The line is the mean of the total population (all six measurements).
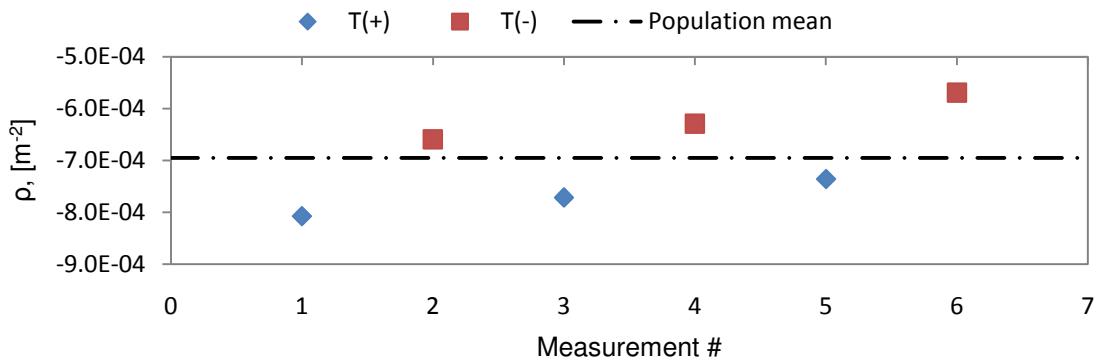


Fig. 90. Gaussian curvature for gap hysteresis test on TFG-2.2.1.

The plot shows that all measurements taken during the T(+) portion of the cycle are less than the mean while measurements during T(-) potion are greater than the mean, indicating that curvature is greater while temperature is increasing. Another trend is observed, specifically the decrease in $\rho$ with increase in the cycle number. This shows that thermal cycling reduces curvature of packaged MEMS.

An area of concern regarding these results is that the shape of TFG-2.2.1, as shown in Fig. 89, is not an ideal fit to the 2nd order polynomial shape. Also, the Gaussian curvature is negative, indicating a saddle shape in which one principal curvature is concave up, while the other is concave down.

## 6.3. Sense gap drift

The sense gap experiment deals with effects of thermal cycling on the shape of packaged MEMS components, however hysteretic effects are not considered. The thermal loading cycle performed is similar to that described in section 6.2, except measurements are only taken on the increasing temperature portion of the cycle, resulting in the experiment profile shown in Fig. 91. A total of 20 cycles are completed, with each cycle lasting for six hours. The total experiment requires five days of continuous execution, which would not be practical without automated data acquisition.
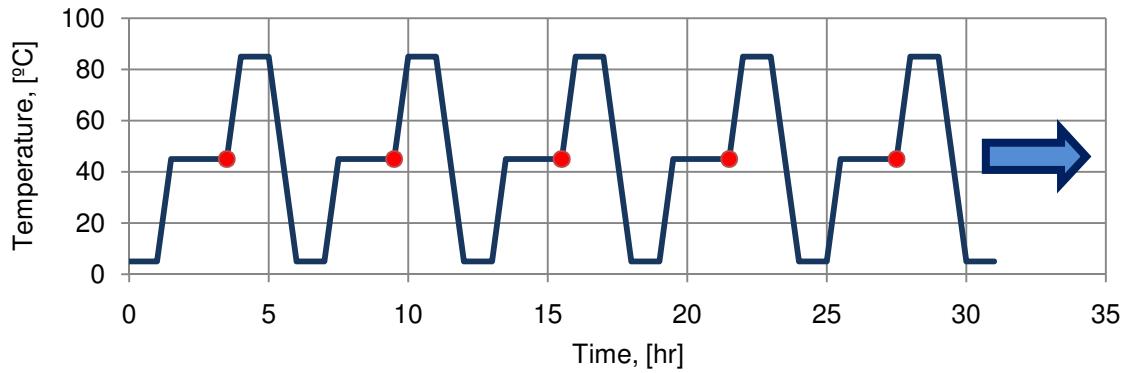


Fig. 91. Measurement profile for gap drift experiment.

The script was generated using the *User Defined Script* interface, which when completed was as shown in Fig. 92.
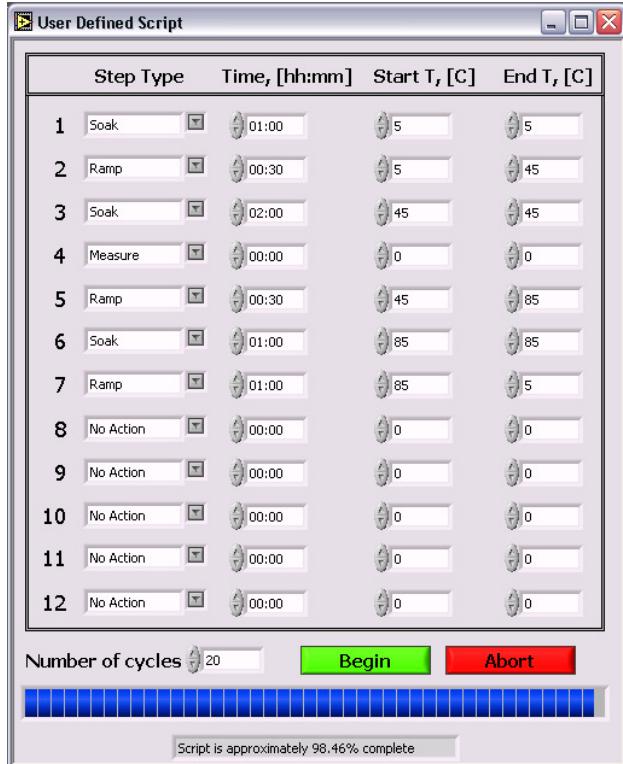
Fig. 92.  Script definition for sense gap drift experiment.

The gap drift experiment is performed on the same components that were used during the sense gap hysteresis test, TFG-2.1.1, TFG-2.2.1, and TFG-2.3.1.  In contrast to the previous experiment, measurements were made on the upper sense plate region, as shown in Fig. 65.  The analyzed USP regions for the first of the 20 measurements for each test article are shown in Fig. 93.  The scale of the color map was adjusted for each measurement to fit the dynamic range of the test article.  As previously seen, the braze die attachment has the largest deformation, with a maximum of 2.018 µm on the color map, while the 9-bump and 25-bump samples have maximum shape variations of 0.845 and 0.252 µm, respectively.
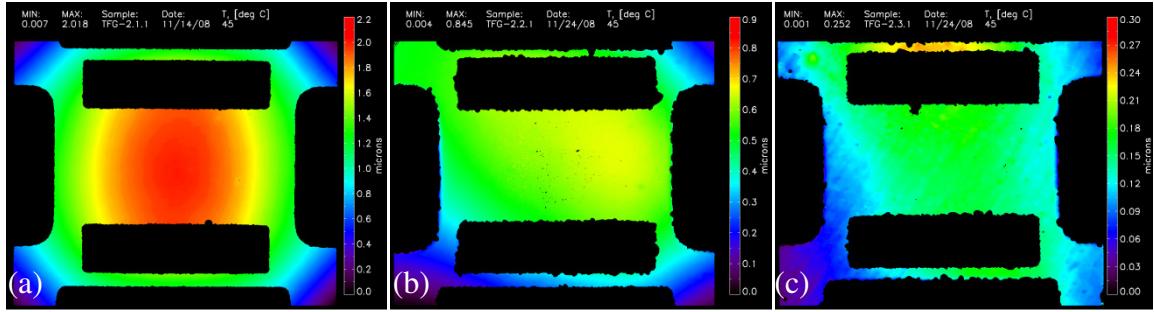
Fig. 93.  Shape of USP region during gap drift experiment: (a) TFG-2.1.1, (b) TFG-2.2.1, and (c) TFG-2.3.1.

The Gaussian curvature is calculated for each measurement, with the percentage change in curvature plotted as a function of cycle number for each component, shown in Fig. 94 through Fig. 96.  A linear model is fitted to the measured data, attempting to quantify the effects of thermal cycling on the shape of the upper sense plate.  The assumption is that a linear relation exists between number of cycles performed and reduction of curvature for the number of cycles.
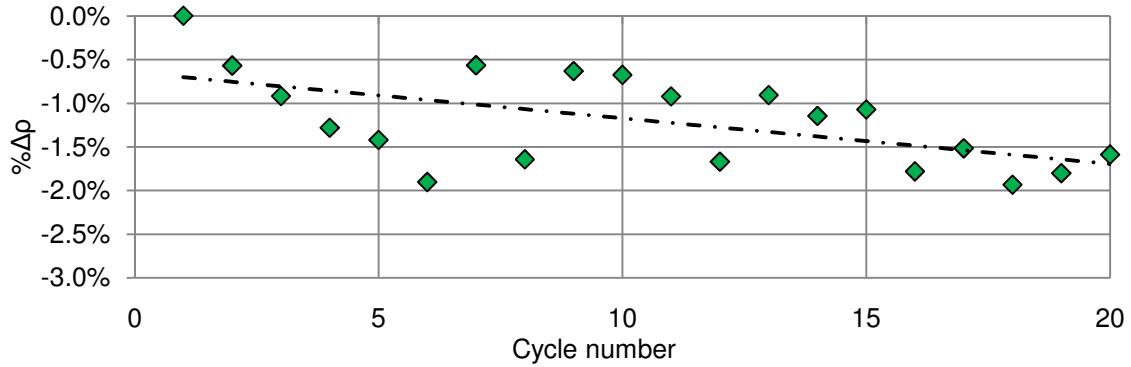


Fig. 94.  Percentage change in Gaussian curvature vs. cycle number, TFG-2.1.1.
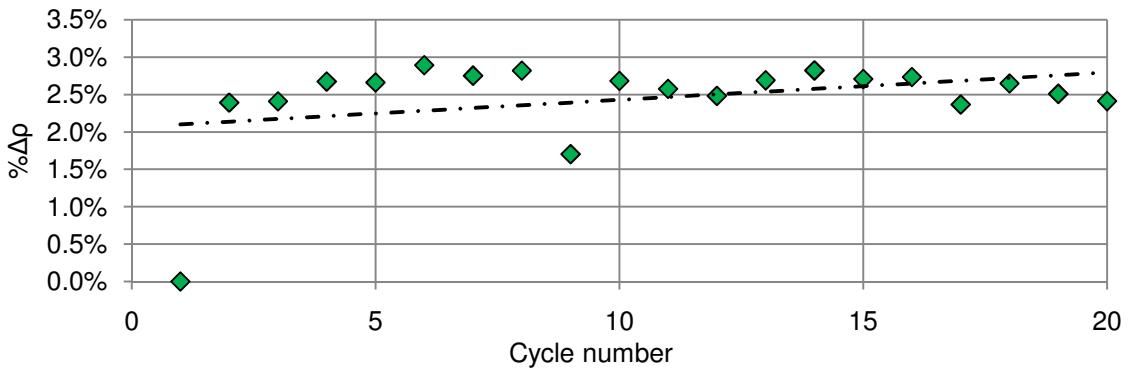
Fig. 95.  Percentage change in curvature vs. cycle number, TFG-2.2.1.
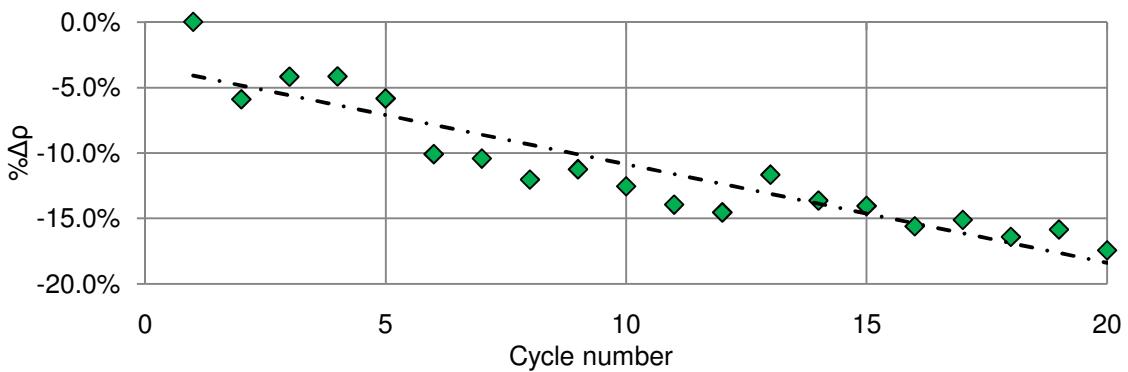


Fig. 96.  Percentage change in curvature vs. cycle number, TFG-2.3.1.

To demonstrate the repeatability of the measurement system a series of 20 measurements were made on sample TFG-2.1.1 held constant at 20ºC with one minute between measurements.  The results of this test are plotted in an identical manner to those of the gap drift measurements, Fig. 97.  The range of the plot is of the same magnitude as the sense gap drift test performed on TFG-2.1.1, Fig. 94.  The maximum percent difference from the initial measurement in the repeatability test is less than 0.2%.
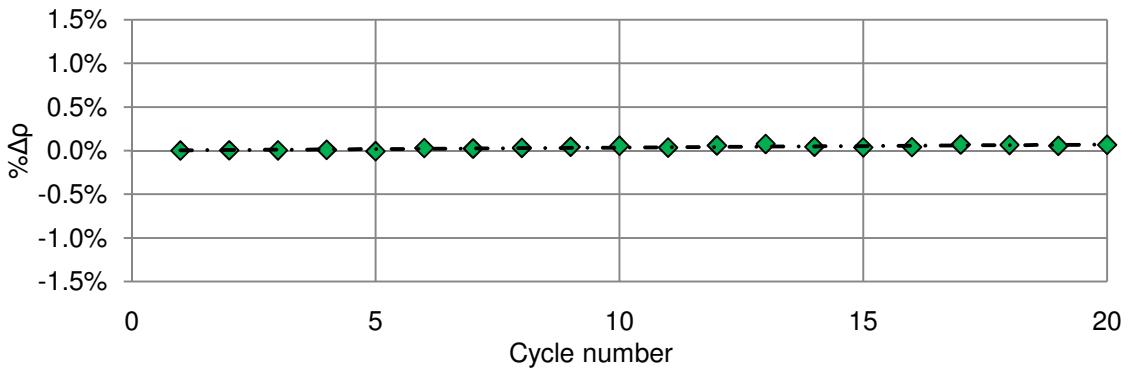
Fig. 97. Change in Gaussian curvature repeatability test, TFG-2.1.1-rep.

The slope of the data fit, $m$, along with the coefficient of determination, $r^2$, are given for each of the sample measurements in Table 9. The $r^2$ value is a measure of the variance in the data that is accounted for by the linear model.

Table 9. Slope and coefficient of determination for sense gap drift measurements.

|         | TFG-2.1.1-rep | TFG-2.1.1  | TFG-2.2.1 | TFG-2.3.1  |
|---------|---------------|------------|-----------|------------|
| $m$     | 3.62E-03      | -5.24E-02  | 3.66E-02  | -7.53E-01  |
| $r^2$   | 0.716         | 0.328      | 0.118     | 0.855      |

The units associated with the slope are percent reduction in the Gaussian curvature per thermal cycle. The coefficient of variance is a percentage, showing the quality of the fit model to the data. The test articles TFG-2.1.1 and TFG-2.2.1 show that only 32.8% and 11.8% of the variance in the data is accounted for by the linear model. The low $r^2$ values suggest that this model is not a good source of information on behavior during thermal cycling. The results for TFG-2.3.1 show must less variance in the model that is unaccounted for. The slope is also one order of magnitude greater than TFG-2.1.1 and TFG-2.2.1.

### 6.4. High acceleration load effects on TFG

Inertial sensors which are implemented for an INS must be robust with regard to high accelerations while remaining sensitive to lower inertial loads. For example, the TFG sensors that are used for navigation would require sensitivity for low rotational rates, below 3000º/sec, yet must be able to survive the high acceleration launch, which might be in excess of 20,000 G's (Karnick et al., 2004). In such a scenario the mass of the chip generates a significant force on the die bonds, potentially causing a plastic deformation, changing the substrate shape.

Measurements made before and after samples are subjected to approximately 15,000 G accelerations are performed on several of the TFG-2 configuration gyroscopes. All 18 of the gyroscope samples of this configuration have been initially measured and returned to the manufacturer for high acceleration loading. The orientation of the applied load was varied throughout the test, and one sample of each die bond type was excluded from the high-G loading, acting as a control sample. After loading was performed by the manufacturer, the samples were returned to WPI for a second set of measurements. All measurements were made with the investigator blind as to which samples had been loaded, and which orientation the load was applied.

The orientation of the die, relative to the applied acceleration, was recorded. The loading orientations, as well as the identity of the control sample, were not known to the investigator during the interferometric measurements, but were revealed after all information was acquired. Although different orientations of the TFG relative to the

133

acceleration are considered it is of particular interest to study the loading normal to the TFG plane.

The first die attachment considered is the AuSn braze. Test article TFG-2.1.4 is measured before and after exposure to a high acceleration load normal to the chip plane, with measurements made on the USP glass. The analyzed shape is shown in Fig. 98, with horizontal traces through the center of the USP shown in Fig. 99.
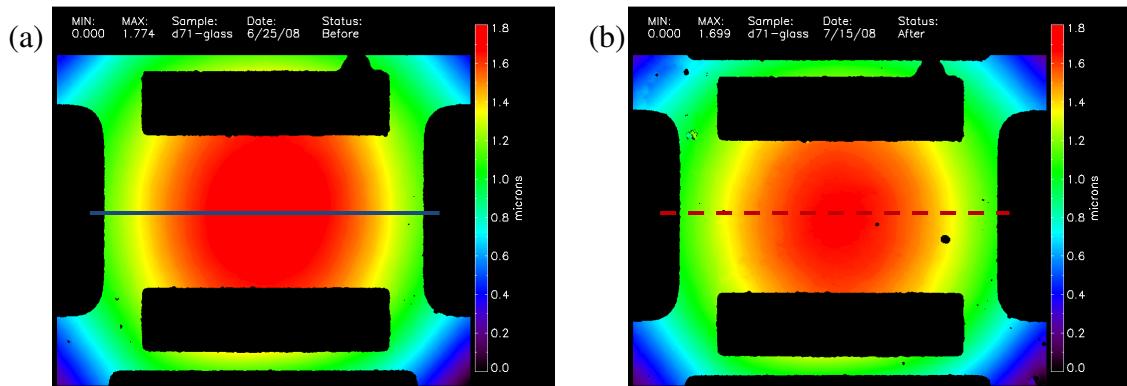


Fig. 98. High-G test for braze die attachment (TFG-2.1.4): (a) before loading, (b) after loading.

The in-plane scale (*x*-axis) of the traces has been normalized to account for slight differences in magnification between the measurements. The results for the AuSn braze die attachment sample that was not exposed to high-G loading, TFG-2.1.5, are presented with horizontal traces taken through the center of the USP in Fig. 100.

134
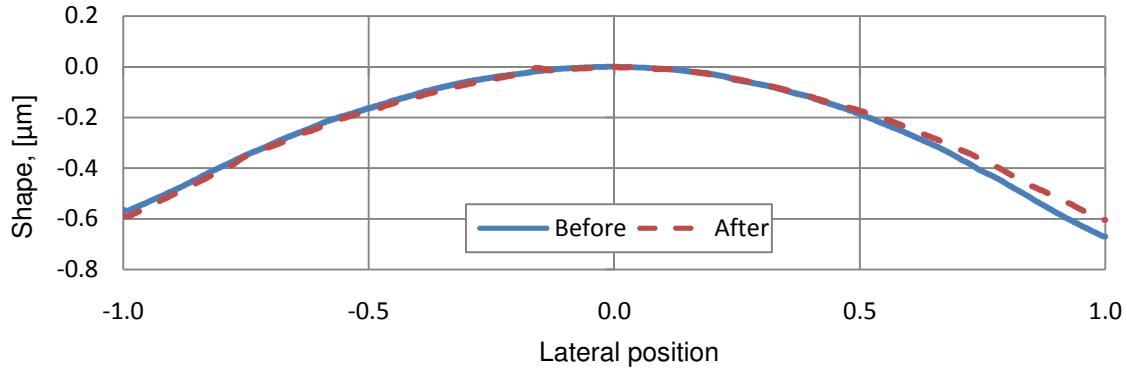
Fig. 99. Horizontal traces through TFG-2.1.4 before and after high-G loading.
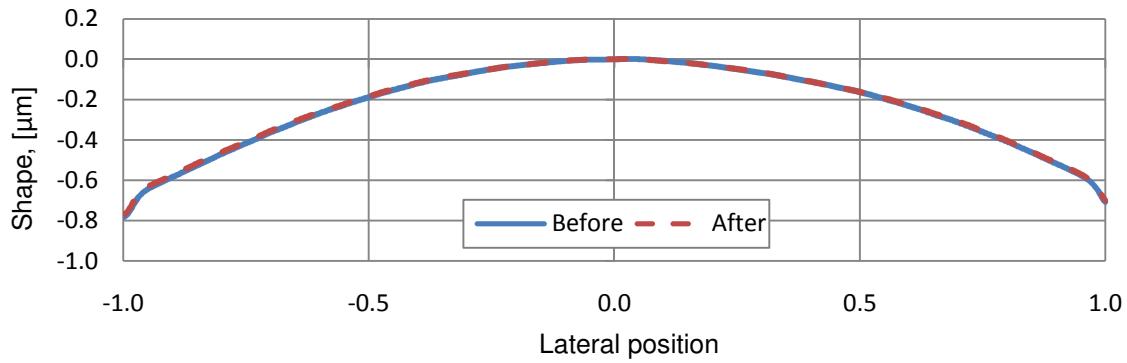


Fig. 100. Horizontal traces through TFG-2.1.5 before and after high-G loading, control sample.

There is a perceivable difference in the traces on the component which was loaded, while the control sample traces appear nearly identical. This preliminary result suggests that the inertial forces associated with acceleration indeed cause a plastic deformation in a braze die bond.

A similar procedure is performed on a test article with a 9-bump die attachment. Sample TFG-2.2.1 is measured before and after loading, with orientation of the load

135

normal to the chip plane. The shape of the chip is shown before and after the inertial loading in Fig. 101.
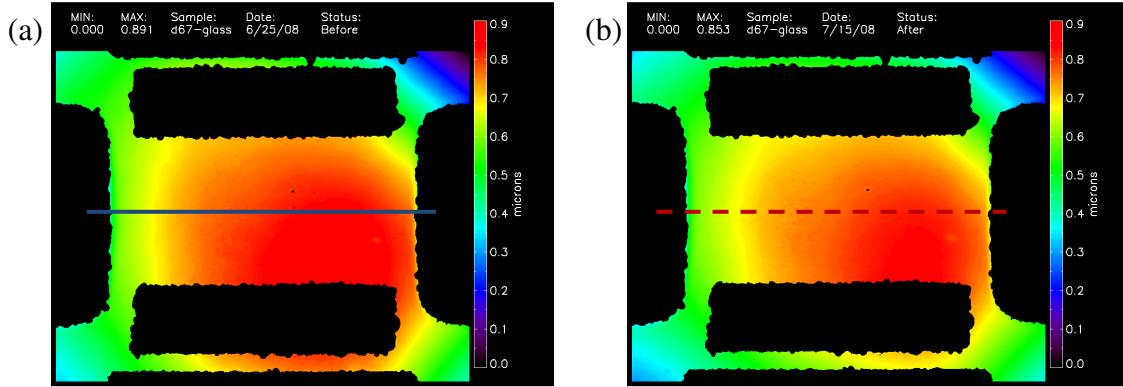


Fig. 101. High-G test for 9-bump die attachment (TFG-2.2.1): (a) before loading, (b) after loading.

Horizontal traces through the center of the USP glass show the changes in the USP topography as a result of the high-G loading, Fig. 102.
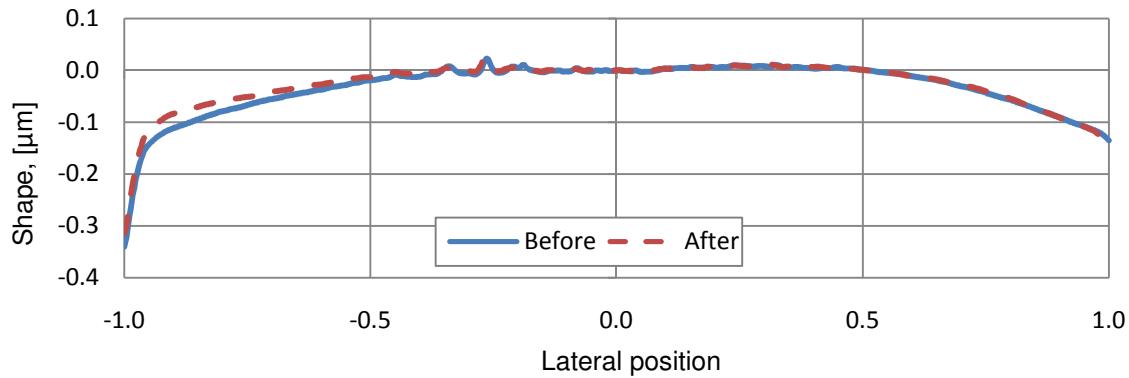


Fig. 102. Horizontal traces through TFG-2.2.1 before and after high-G loading.

A control sample, TFG-2.2.5, has been measured at the same times as TFG-2.2.1, however this sample was not subjected to the high-G loading. The horizontal traces made across the USP glass are shown in Fig. 103.
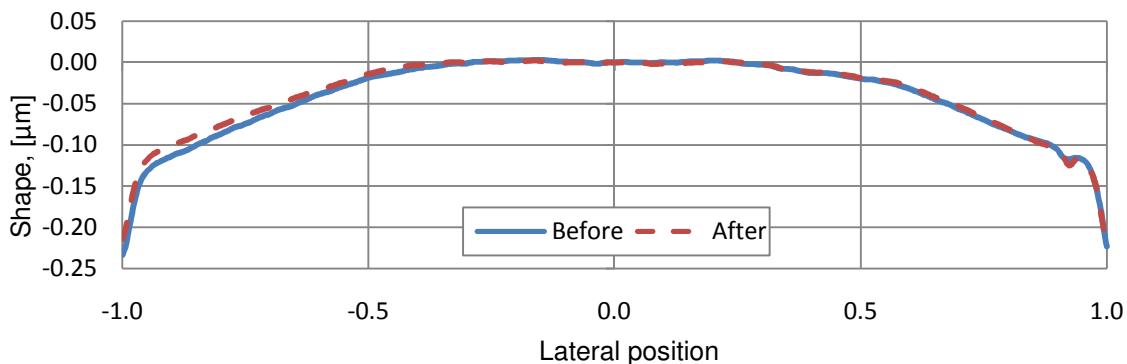
Fig. 103.  Horizontal traces through TFG-2.2.5 before and after high-G loading, control sample.

The shape measurements of a 25-bump die attached sample, TFG-2.3.4, are shown in the before and after states in Fig. 104.  During the high-G loading the lid for the package fractured and chipped the USP glass, causing the missing section from the after analysis.
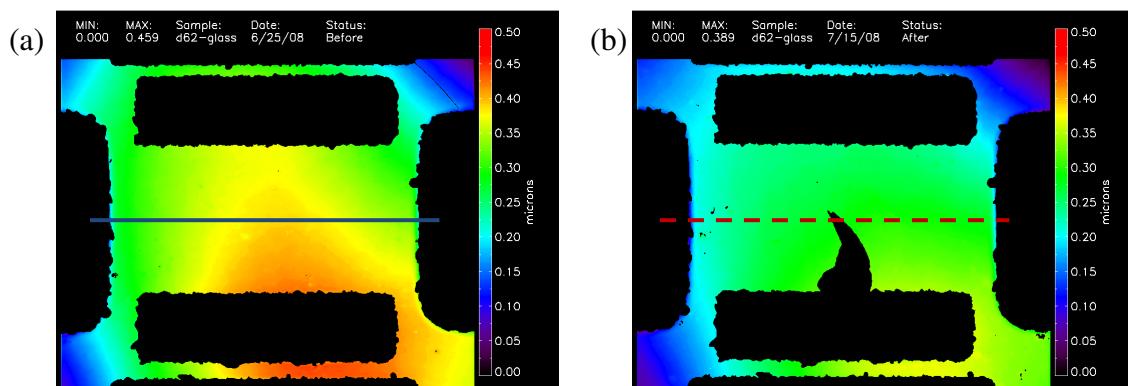


Fig. 104.  High-G test for 25-bump die attachment (TFG-2.3.4): (a) before loading, (b) after loading.

The traces extracted from the measurements, Fig. 105, show a more definitive change in shape than in the 9-bump and braze results.  As with other samples, a control sample for 25-bump die attach was also measured, with the traces shown in Fig. 106.

137
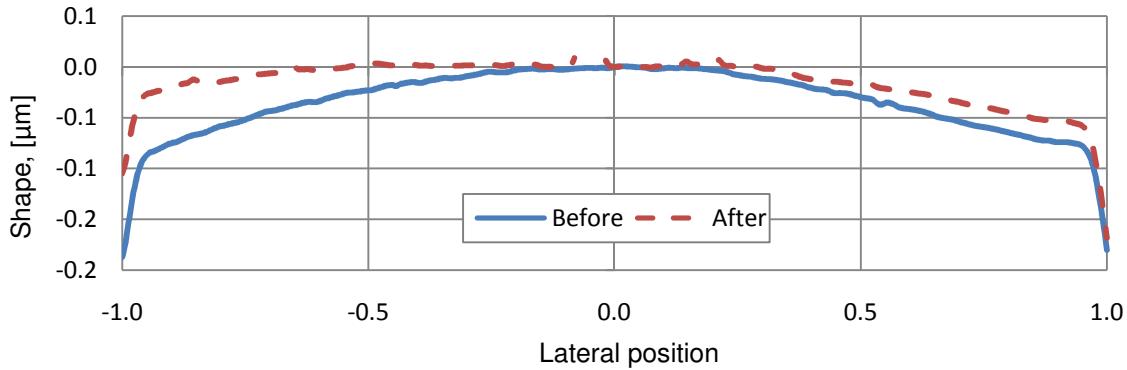
Fig. 105.  Horizontal traces through TFG-2.3.4 before and after high-G loading.
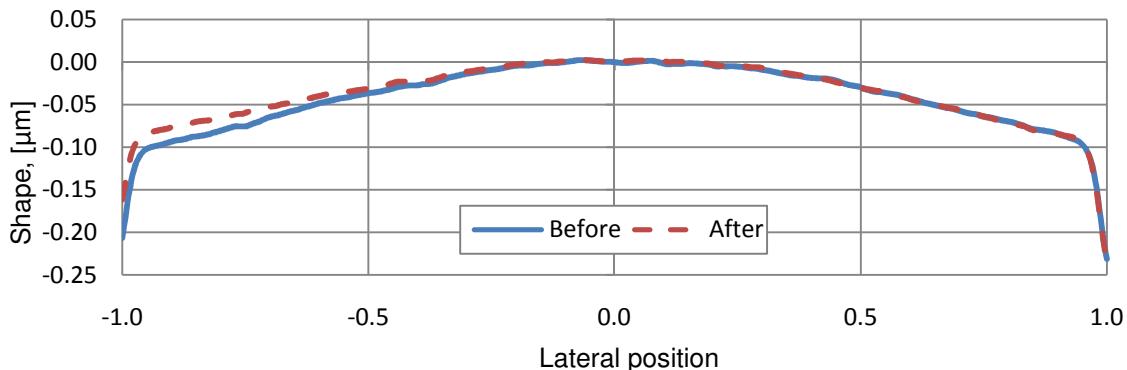


Fig. 106.  Horizontal traces through TFG-2.3.3 made at same times as before and after measurements on TFG-2.3.4.

The principal curvature in the horizontal ($x$) direction has been determined by fitting the 2$^{nd}$ order surface to the USP glass.  The reduction in curvature for the six components discussed (three test samples and three control samples) is summarized in Table 10.  For all six samples there is a reduction in the curvature, however for each bond type the magnitude of the curvature reduction is greater when subjected to the high-G acceleration loading.  Theoretically, there would be no change in curvature for the control samples, as no external loading has been applied.  This however is not the case, the

138

control samples have exhibited a reduction in the principal curvature.  For each die bond

method the control sample has shown less curvature reduction than the loaded sample.

Table 10.  Reduction in $\kappa_x$ for high-G load test samples.

| Die Attachment | Test | ID | %$\Delta\kappa_x$ |
|---|---|---|---|
| Braze | Loaded | TFG-2.1.4 | -4.2% |
| | Control | TFG-2.1.5 | -2.8% |
| 9-bump | Loaded | TFG-2.2.1 | -13.6% |
| | Control | TFG-2.2.5 | -3.6% |
| 25-bump | Loaded | TFG-2.3.4 | -37.6% |
| | Control | TFG-2.3.3 | -7.4% |

There might also be a time-dependant relaxation in the die bond causing the

curvature reduction in the control samples, yet additional plastic deformations are present

when subjected to high inertial loads.  The potential effects of time dependent relaxation

in die bonds are presented in following section.

## 6.5.  Time dependent deformation of TFG

In order to maintain high vacuum environments TFG chips are bonded into a

ceramic package by gold thermocompression bump bonds or gold tin eutectic braze

(Marinis and Soucy, 2003).  Often creep behavior is not considered for metals which are

in ambient conditions, however gold has been observed to exhibit time dependent plastic

strain, or creep, at ambient temperatures (Ramsey, 1975).  This creep behavior results in a

relaxation in the die bond, reducing the curvature of a MEMS substrate.  Interferometric

characterization of the MEMS, made with a storage time of 19 months between

measurements, shows the magnitude of these effects.

The test samples are TFG-3 configuration, with 4-bump compression bond die attachment in two geometries, described in section 5.3.3. All six of the TFG-3 samples have been measured upon initial receipt at WPI, and again 19 months later after storage in the lab environment of 68ºC and 50% RH.

The metalized frame surrounding the TFG structure is measured to obtain a continuous line from which the curvature value are determined, Fig. 107.
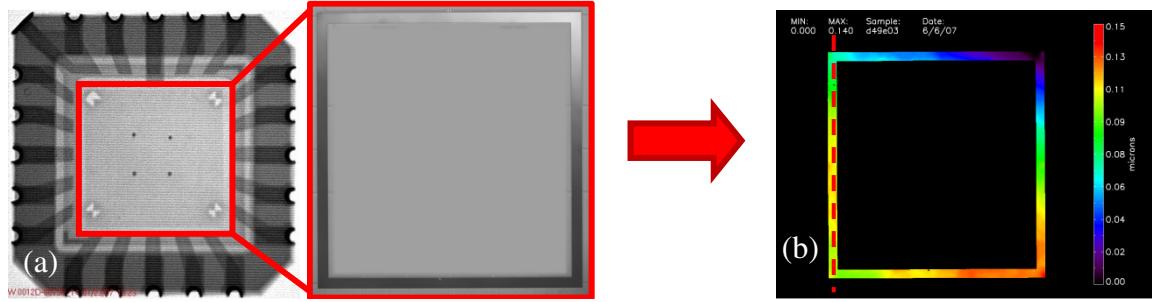


Fig. 107. Metalized frame on the MEMS component: (a) phase image, (b) scaled data.

The quantified measurement is the vertical trace shown as the dashed line on the metalized frame in Fig. 107(b). Representative traces along this line, extracted from, both, the initial and relaxed measurements, are shown for TFG-3.1.1 (close configuration) and TFG-3.2.1 (spread configuration) in Fig. 108 and Fig. 109, respectively.
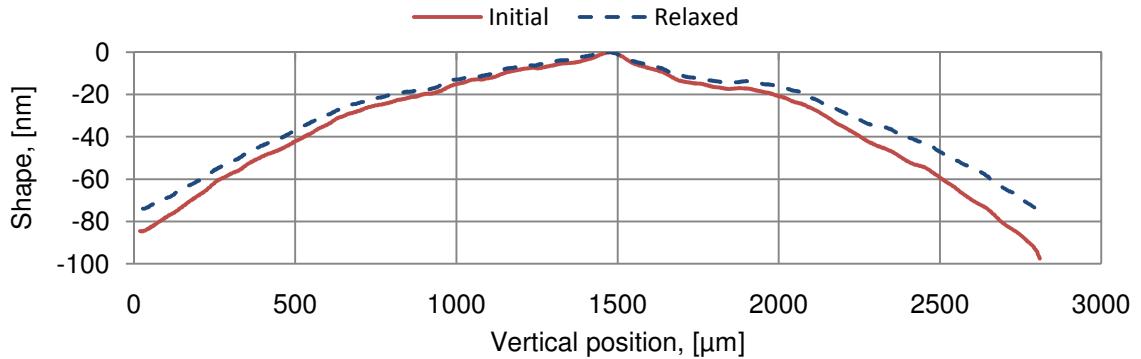
Fig. 108. Relaxation measurements made on TFG-3.1.1.
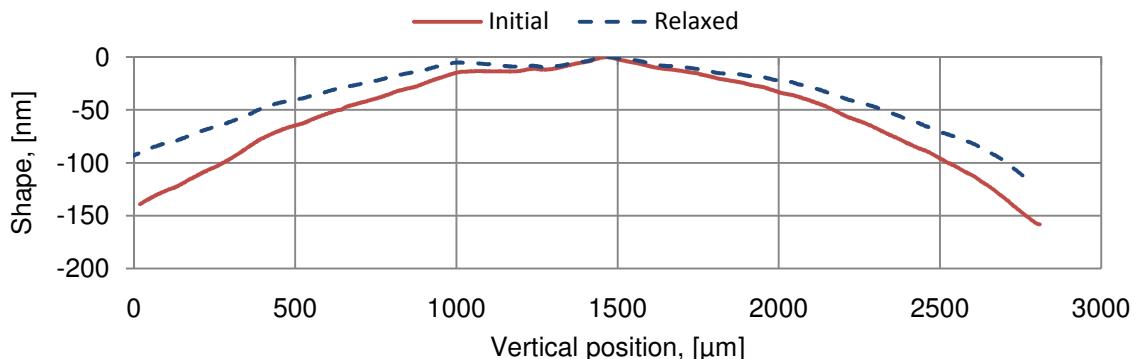


Fig. 109. Relaxation measurements made on TFG-3.2.1.

Both bump configurations show a change in the curvature over the 19 months of storage; however the magnitude of the curvature is of interest. Initially there is greater curvature in the spread-bump configuration, as expected. This is due to the greater length between the bumps exposed to the temperature change from bonded to ambient temperature. Also, the degree of relaxation appears to be greater in the spread configuration, which is due to higher shear stress in the gold bump.

The traces are used to calculate curvature by the second derivative of the quadratic fit for each of the six samples. The results of all components are summarized in Table 11.

Table 11.  Change in die curvature after 19 months of storage.

| Sample | $\kappa_{y,initial}$, [$\mu m^{-1}$] | $\kappa_{y, relaxed}$, [$\mu m^{-1}$] | %$\Delta\kappa_y$ |
|---|---|---|---|
| TFG-3.1.1 | -8.66E-08 | -7.29E-08 | -16% |
| TFG-3.1.2 | -8.71E-08 | -6.69E-08 | -23% |
| TFG-3.1.3 | -1.04E-07 | -8.50E-08 | -18% |
| TFG-3.2.1 | -1.47E-07 | -1.02E-07 | -31% |
| TFG-3.2.2 | -1.46E-07 | -1.11E-07 | -24% |
| TFG-3.2.3 | -1.33E-07 | -1.06E-07 | -20% |

The reduction of curvature shows the relaxation behavior of the gold bump bonds at typical (68ºC, 50% RH) storage conditions.  The changes in the curvature are similar (if not greater) in magnitude to those observed with a 40ºC temperature change shown in section 6.1.2.

Measurements made at different points in time may also be used to develop a mathematical model of the relaxation of the MEMS die as a function of time, as shown by Marinis et al. (2006, 2008a).

## 6.6.  Dynamic TFG measurements

Thus far all measurements shown on the TFG samples are of static components, investigating the curvature caused by die bonding, and exploring the changes in the curvature caused by thermal loading, inertial shock, or creep behavior.  In order to determine the influence that curvature, and its change, has on TFG components testing must be performed on functional samples.  The testing, presented in the subsequent sections, details the effect that temperature has on the performance by characterizing the TFG samples on a rate table.  The motion of the proof masses is then studied by using the

stroboscopic illumination feature of the interferometer in conjunction with scripting functionality to measure a dynamic cycle.

### 6.6.1. Rate table testing

In order to characterize the TFG dynamic performances, the gyroscopes were mounted on a rate table with custom heating element. The process described in section 3.6 was used to test the gyroscope behavior as a function of temperature.

The usable range for the gyroscope is approximately ±1500 °/sec. Output voltage recordings are made at 100 °/sec intervals. The entire range is covered at each temperature, and when plotted the results are as shown in Fig. 110.
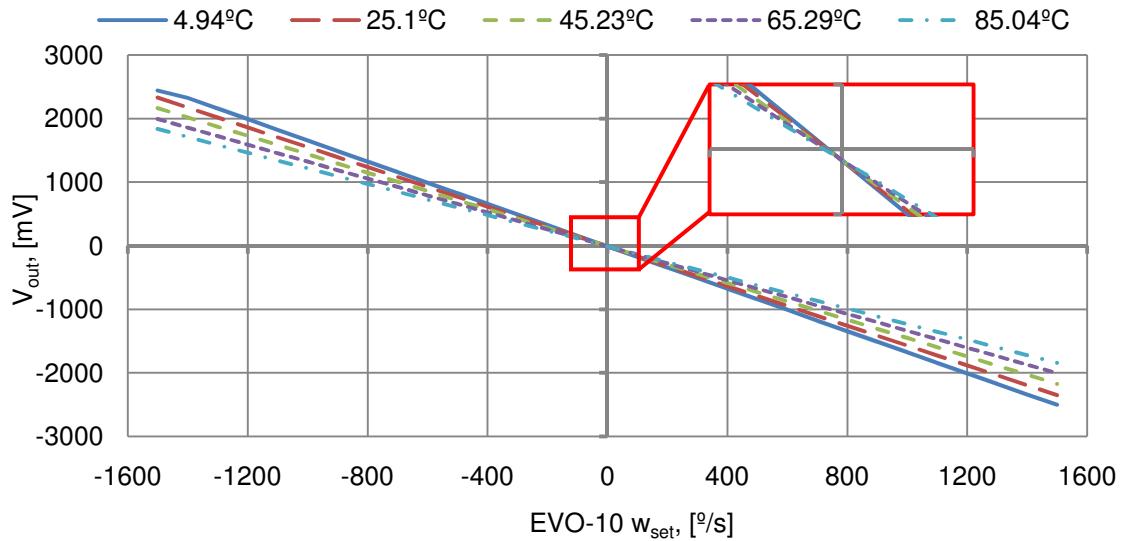


Fig. 110. Characterization of TFG-1.1.1 at various temperatures.

The gain, which is the slope of Fig. 110, clearly changes as a function of temperature; this is more vividly shown by plotting the gain voltage as a function of temperature, Fig. 111. It is noted that the slope is clearly negative in Fig. 110, however

143

all values in Fig. 111 are positive because they represent magnitudes of gain voltages. The directionality of the gain voltage only shows the agreement in orientation between the rate table and the TFG component, thus the magnitude is plotted.
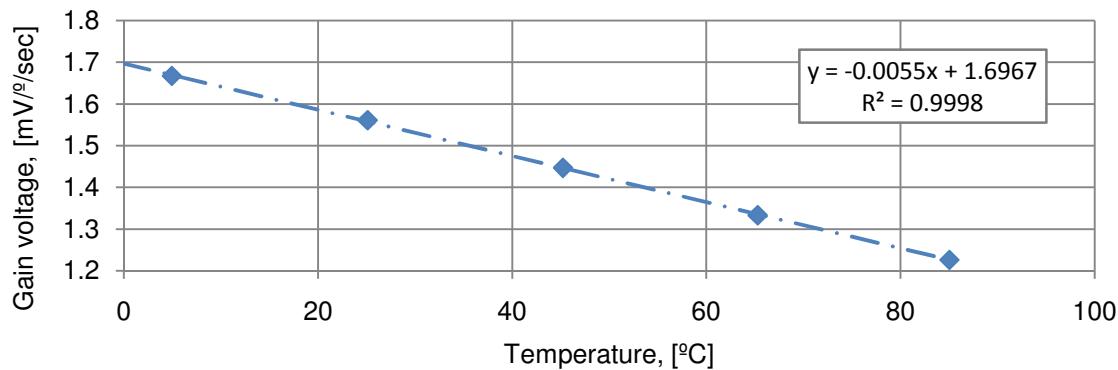


Fig. 111. Gain voltage as a function of temperature, TFG-1.1.1.

The gain voltage decreased by 26.4% over the 80ºC range while temperature increased, greatly affecting the performance. The effect of temperature on all three gyroscopes of this configuration is summarized in Table 12.

Table 12. Gain voltage change with temperature for TFG-1.1 configuration.

|  | TFG-1.1.1 | | TFG-1.1.2 | | TFG-1.1.3 | |
|---|---|---|---|---|---|---|
|  | $V_{gain}$, [mV] | %Δ | $V_{gain}$, [mV] | %Δ | $V_{gain}$, [mV] | %Δ |
| 5ºC | 1.67 | 0% | 1.93 | 0% | 1.76 | 0% |
| 25ºC | 1.56 | -6% | 1.82 | -6% | 1.67 | -5% |
| 45ºC | 1.45 | -13% | 1.71 | -11% | 1.58 | -11% |
| 65ºC | 1.33 | -20% | 1.60 | -17% | 1.49 | -15% |
| 85ºC | 1.23 | -26% | 1.51 | -22% | 1.41 | -20% |

The change in the gain might be caused by several factors, including temperature dependency of the material properties. Also, the bias voltage is not constant with

temperature, as shown in Fig. 112, where the bias voltage (ZRO) decreases as
temperature increases.
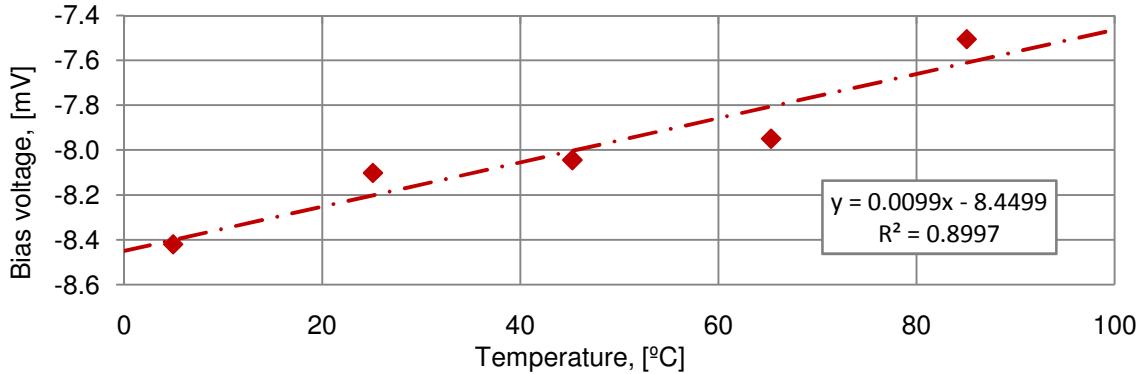


Fig. 112. Bias voltage as a function of temperature, TFG-1.1.1.

The changes in the bias voltage are shown for all TFG-1.1 configuration
components in Table 13, with the percentage reduction in bias also calculated.

Table 13. Bias voltage change with temperature for TFG-1.1 configuration.

|  | TFG-1.1.1 | | TFG-1.1.2 | | TFG-1.1.3 | |
|---|---|---|---|---|---|---|
|  | $V_{bias}$, [mV] | $\%\Delta V_{bias}$ | $V_{bias}$, [mV] | $\%\Delta V_{bias}$ | $V_{bias}$, [mV] | $\%\Delta V_{bias}$ |
| **5ºC** | -8.42 | 0% | 2.32 | 0% | -79.12 | 0% |
| **25ºC** | -8.10 | -4% | 2.25 | -3% | -76.24 | -4% |
| **45ºC** | -8.04 | -4% | 2.07 | -11% | -74.41 | -6% |
| **65ºC** | -7.95 | -6% | 1.98 | -15% | -72.23 | -9% |
| **85ºC** | -7.51 | -11% | 2.08 | -11% | -70.24 | -11% |

The bias voltage magnitude decreased as the temperature increased. The bias
voltage is related to the quadrature error in a gyroscope, giving the ZRO. The bias may
be accounted for by DC correction at a reference state. These results suggest that a single
DC correction may not be sufficient, but rather a temperature dependent compensation

might be required.  Furthermore, the ZRO appears to be caused by the curvature, not solely the temperature.

### 6.6.2. Dynamic shape measurements

A unique feature of the automated interferometer system is the ability to make in-situ measurements, while a MEMS device is excited, by utilizing stroboscopic illumination.  Representative measurements are presented for a TFG device, in which proof masses are excited in-plane (drive axis), while sensing is performed out-of-plane (sense axis).  In the case of no input rotation there should not be proof mass motion in the sense direction.  Any such motion in the sense axis is a quadrature error, limiting the resolution of the sensor.

The TFG-1 configuration gyroscopes are functional devices with the upper sense plate removed to allow for the measurement of the proof masses in either a static or dynamic state.  The device, powered by DC voltage, outputs a sinusoidal voltage of the drive resonance frequency.  The drive frequency signal is used as a trigger to the synthesizer, which generates a square wave to modulate LED driver.  The square wave, with a duty cycle of 8.5%, triggers the LED with a rise time of 100 ns.  The stroboscopic illumination allows for the shape measurement at a finite position along the proof mass stroke motion.  Adjustment of the phase of the square wave, relative to the trigger input signal, allow for measurement at various positions of the operational cycle.

By using the scripting capabilities of the interferometer it is possible to automate the data acquisition of a running gyroscope.  Phase stepped recordings are made at 19

discrete positions of the in-plane motion. The measurements are made at 20º increments

of the phase cycle, ranging from 0º through 360º. The first and last measurements are

made at the same position. The phase step of each measurement is verified before

accepting and saving the data.

Post processing allows for inspection of changes in the device during actuation.

In particular the rigid body displacements and deformations of the proof masses during

drive actuation are of interest. For the TFG-1.1.1 sample shape recordings have been

made throughout the drive cycle and analyzed. The left proof mass of the TFG is shown

at the left and right extremes of the motion in Fig. 113. The color map indicates changes

in the elevation of the proof mass, and possibly the shape of the proof mass, throughout

the cycle. The shape of the proof mass is approximated by the second order surface, as in

section 6.1.1, where the principal curvatures in $x$ and $y$ directions are found by applying

Eq. 35.
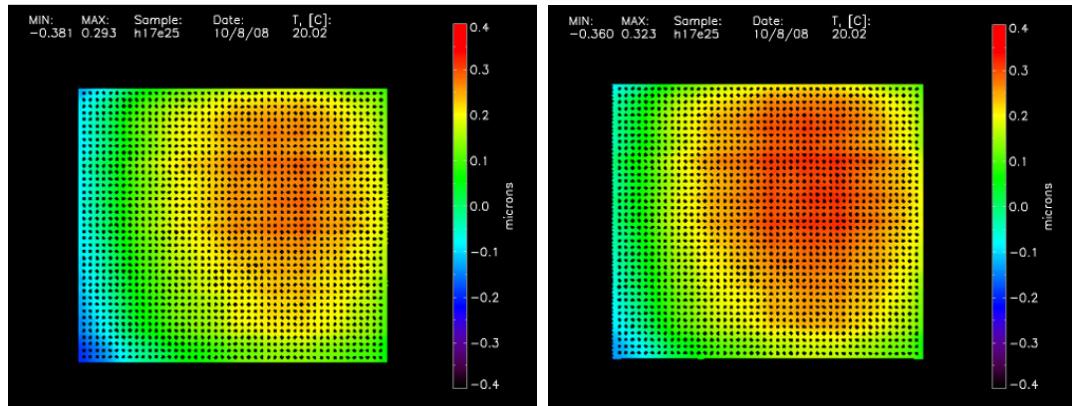


Fig. 113. Shape of the left proof mass during actuation: (a) extreme left position, (b)
extreme right position.

The amount of out-of-plane motion has been tracked by extracting the value at the center of the proof mass throughout the entire drive cycle. The in-plane position is normalized such that the magnitude of the stroke is 1.0, with the left mass traveling from -1.5 to -0.5, while the right mass travels from 0.5 to 1.5. This allows for an intuitive plot of shape (or other property of the proof mass) as a function of in-plane position. The pixel values of the center of the left and right proof masses are recorded, this process is repeated for five cycles. In each cycle, the first measurement, where the proof masses are at their innermost position, is treated as a reference and is subtracted from the subsequent measurements. Extracted values from each of the five cycles, along with the average for all five cycles, are plotted in Fig. 114.
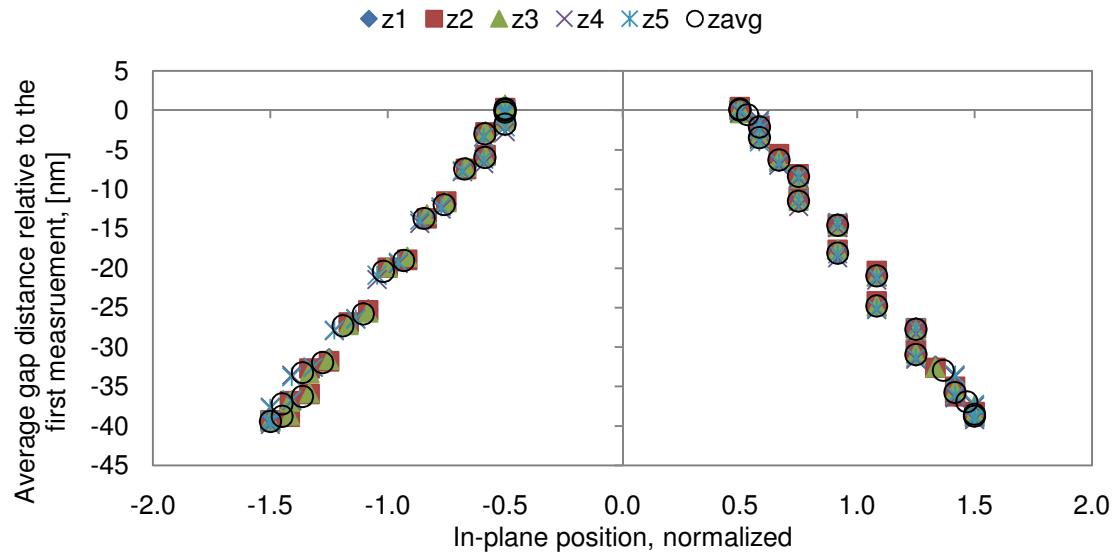


Fig. 114. Out-of-plane displacement of proof masses during TFG actuation, center point tracking on TFG-1.1.1.

There is clearly a repeatable, out-of-plane motion in the proof masses during actuation. Without further investigation it is still unclear if the gap distance change is due

148

to purely rigid body motion of the proof masses or if there is some degree of deformation as well. The analytical model of the second order surface for each of the proof masses allows for inspection into changes in the proof masses throughout the cycle. Specifically, the linear (*B* and *D*) terms of Eq. 37 are related to the tilt of proof masses, and the quadratic terms (*C* and *F*) are related to the curvature of the proof masses. The percent change in each of these surface fit coefficients provides insight into cyclical changes in the proof masses, perhaps affecting performance.

The proof masses tilt during actuation, which can be determined based on the linear coefficients of the surface model. The principal tilt is contained in the *B* (*y* axis) and *D* (*x* axis) terms. The percent change in the tilt, *m*, relative to the first measurement, is shown in Fig. 115. A total of five cycles were measured, with the tilt values averaged at each of the 19 measurement positions. The error bars represent the standard deviation of the five measurements.
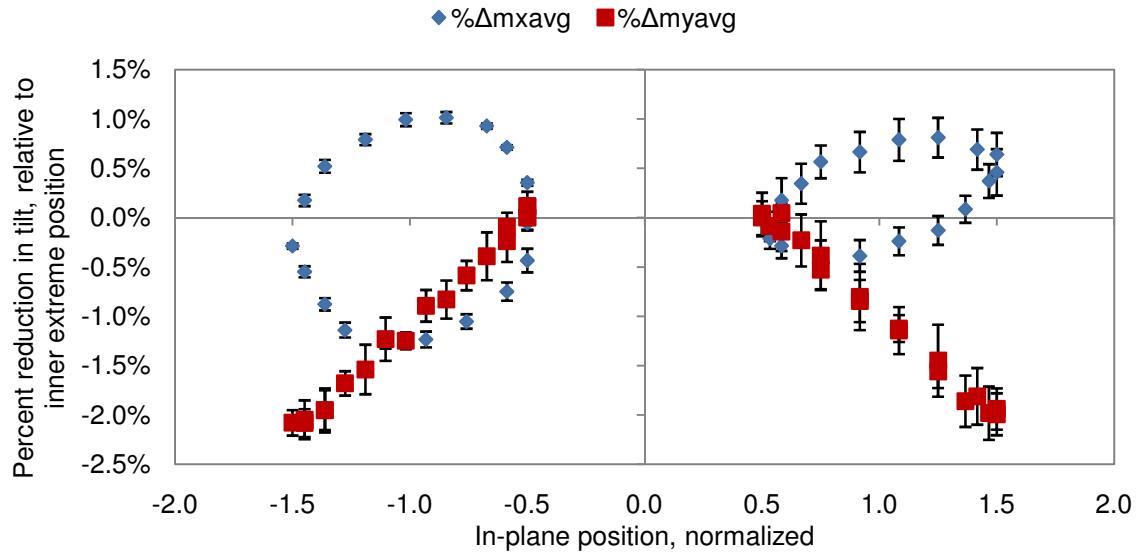


Fig. 115. Percent change in proof mass tilt during actuation, TFG-1.1.1.

The tilt changes in the proof masses in the *y* direction decrease as the masses move apart, showing some rotation during the cycle. The tilt in the *x* axis however is not as simple. The extreme inner and outer positions possess the same amount of tilt, yet there is a rocking behavior during the motion.

The principal curvatures are analyzed in the same manner, plotting relative change in curvature as a function of in-plane position. These results show the amount of deformation in the proof masses while running, summarized in Fig. 116.
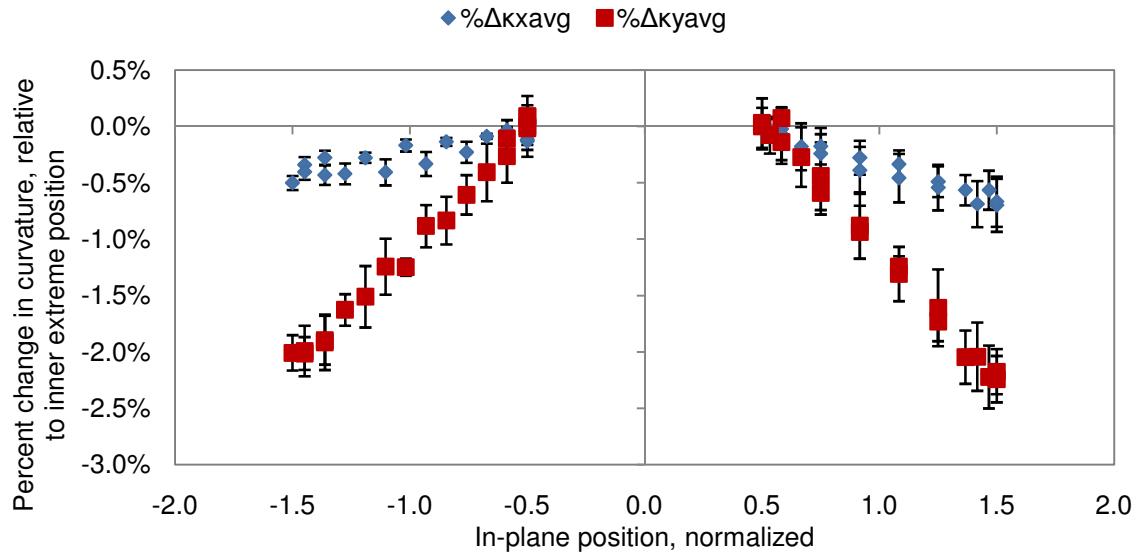


Fig. 116. Percent change in proof mass curvature during actuation, TFG-1.1.1.

The changes in curvature show that there is more than simple rigid body movement of the proof masses, there is also some degree of deformation present. This suggests that the operation frequency of the TFG is at, or near, a resonance frequency of the proof masses.

The overall change in average gap distance is determined by the method presented in Eq. 39 of section 6.1.1. Integration is performed between the surface of the proof mass

and the substrate for each position throughout the cycle. The volume is divided by the proof mass area to determine the average gap distance. Changes in the gap distance relative to the first measurement are plotted as a function of normalized in-plane position, Fig. 117. The standard deviation between the five measurements is shown as error bars. The standard deviation is small enough that in most cases the error bars are completely hidden by the data marker.
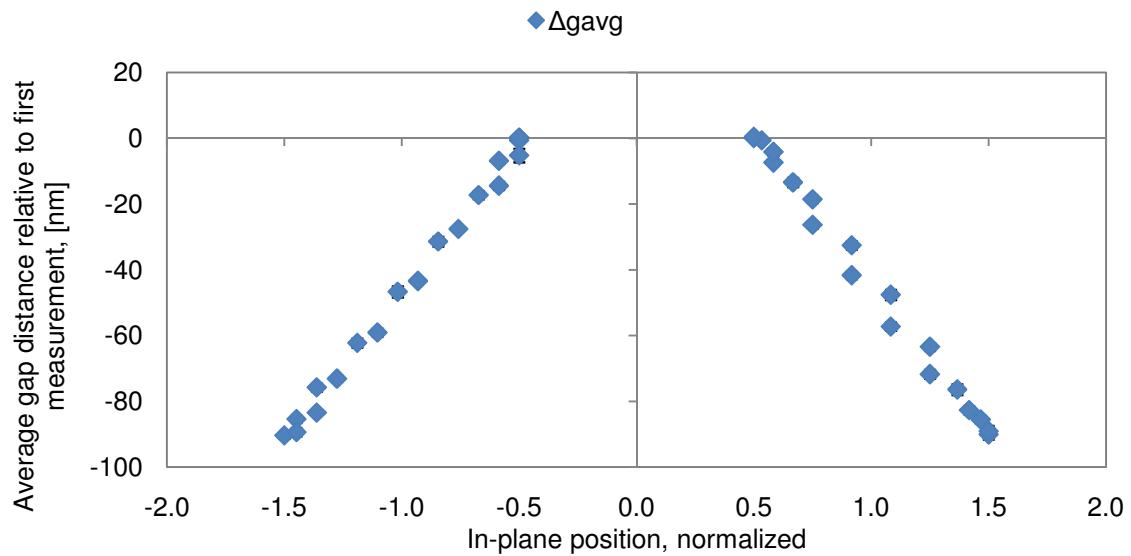


Fig. 117. Change in average gap distance calculated from surface integration between proof masses and substrate of TFG-1.1.1.

The trend of the change in the average gap distance is nearly identical to that when tracking the center point of the proof mass, Fig. 114, however the magnitude of the gap distance change is much greater when considering the full surfaces rather than a single point. The simple methodology of tracking the elevation of the proof mass during actuation by the center point is not valid for accurate determination of sense gap behavior during the TFG drive cycle. The changes in curvature and tilt affect the average gap

distance substantially.  An identical test procedure has been applied in the measurement

of samples TFG-1.1.2 and TFG-1.1.3.  These results are summarized in the data plots

located in Appendix D.

It's been previously shown in section 6.6.1 that the performance of the TFG-1

devices changes as a function of temperature.  Such changes in performance suggest that

the quadrature error of the device changes with temperature as well.  Dynamic

measurements are made on TFG-1.1.1 at temperatures of 5ºC and 85ºC.  As with the

previous dynamic measurements shown in this section, five cycles are measured at each

temperature, with the results of the five cycles averaged.  The substrate is measured

between each cycle and used to determine the average gap distance by integration

method.  The average gap distance change is plotted as a function of normalized in-plane

proof mass position, Fig. 118.
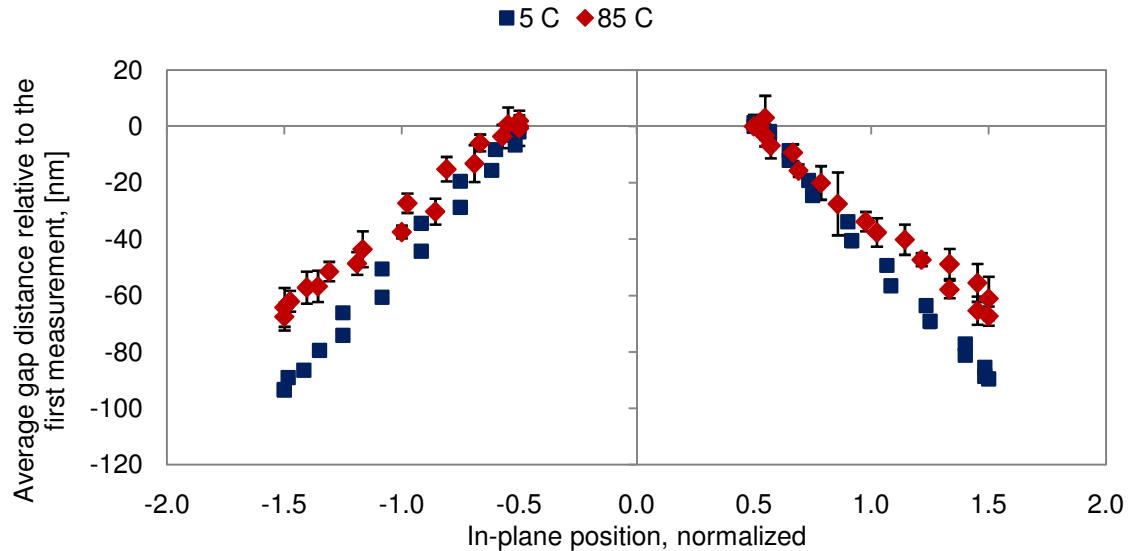


Fig. 118.  Average gap distance change at low and high temperature states, TFG-1.1.1.

There is a reduction in the relative gap distance throughout drive cycle, showing that temperature does affect the quadrature error. It was shown in section 6.1.1 that an increase in temperature reduces the curvature of the substrate by approaching the bond temperature for the TFG-1 configuration test articles. It was also shown that the magnitude of the ZRO of the gyroscope reduces with temperature. A major source of ZRO is quadrature error. These results suggest that the die curvature is a cause of quadrature error, as well as the known factors of mass imbalances and non-ideal spring flexures.

## 7. DISCUSSION

In order to perform in-depth analysis into MEMS components, including TFG samples, a new interferometer has been developed at the CHSLT facilities of WPI. The interferometric principles of the interferometer are based on PSI using a Twyman-Green interferometer, similar to previous measurement tools implemented at WPI or in commercial systems. The advances with the developed system are two-fold, first being the integration of a thermal loading with an enclosed chamber and optical window for data acquisition. Such chambers are not compatible with current commercially available systems due to the inability to compensate for the window.

The second major advance with the WPI developed interferometer is the implementation of a complete software interface, allowing for remote, autonomous, operation of the interferometer as well as scripted data acquisition. By interfacing nearly all of the components in the interferometer with a host PC a complete user interface has been developed based on LabView virtual instruments (VIs). LabView has proven to be a capable software package for interface development, allowing for a modular software design. Each hardware component is controlled by a single VI. This is particularly useful in upgrading the WPI system, where few changes to the overall architecture are required to implement a new piece of hardware.

The software control of the interferometer allows for automated data acquisition following a set of pre-defined scripts, or through the generation of a custom script following the user defined script interface. A number of common procedures have been compiled into a script library, consisting of procedures for investigating thermal loading,

thermal cycling, and dynamic analysis. Many of the scripts require automation for practicality. Interactive data acquisition is not ideal for experimental procedures which require constant monitoring of temperature, and triggering of shape measurements, over days or weeks at a time. Scripting the acquisition enables a single user to complete the experiment with minimal interaction during the experiment.

The remote control of the thermal loading chamber allows for thermal cycling experiments. Thermal cycling is a fundamental test for components, often with electrical properties monitored during the cycling to detect changes in performance, or instances of failure. Although this type of analysis provide insight into the effect of thermal cycling, the cause of failure is often unknown. Modification of a mechanical design is difficult if blind implementation and trial and error efforts are taken. With an interferometer which is able to perform thermal cycling the design process may be streamlined.

The capabilities of the automated interferometer have been demonstrated through various tests performed on MEMS TFG components. In particular, the effects of packaging and die bonding are explored with relation to TFG performance. It was shown that after die bonding residual thermomechanical stresses result in a distorted chip substrate. The CTE differences between the chip and the package cause a shear stress on the gold bump, bowing the chip. The TFG structure, consisting of the proof masses, along with the substrate are measured using the interferometer to determine the changes in the average gap distance in the capacitive sensor formed by the two surfaces. Integration between analytical models of the surfaces provides a method for determination of the average gap distance. It was shown that in all cases there is a

155

reduction in substrate curvature as temperature increases. This is consistent with a deformation that is caused by the decrease in system temperature after the die bonding.

Thermal cycling was demonstrated by two procedures, one designed to investigate hysteretic effects, with a second to study the overall drift of the sense gap. The analysis of both experiments is such that the die curvature is treated as the dependent parameter, with respect to the cycle number. In the *sense gap hysteresis* experiment three cycles were performed, with measurements made on the increasing and decreasing portions of the cycle. A t-test has been applied, between the increasing and decreasing measurements, for three different die bond configurations. Of the samples, only the 9-bump configuration (TFG-2.2.1) shows a statistically significant curvature difference between the increasing and decreasing samples. The test for each component required 24 hours of continuous operation and repeated measurements at predetermined points in time.

The *sense gap drift* experiment was performed on three samples, with a linear regression analysis made on the curvature as a function of cycle number. The expected result is a relaxation in the die bonds, causing a reduction in curvature, as a function of thermal cycle. A reduction was observed for the braze (TFG-2.1.1) and 25-bump (TFG-2.3.1) configurations. Although the behavior followed a linear model over the duration studied, a more representative model might be non-linear, in which curvature asymptotically approaches a steady state value. More cycles are needed to observe this behavior, and a greater number of samples should be tested under identical conditions to support any findings. More significant than the observed die relaxation however is the

ability to complete a scripted data acquisition process over the duration of five consecutive days, with constant adjustment of temperature.

In both the *hysteresis* and *gap drift* tests the ability to perform the procedures has been demonstrated, however careful experimental design should be followed to make conclusions. Very small effects are expected, which require a substantial amount of data to be recorded to show statistically relevant results. As shown for illustrative/descriptive purposes, only one sample of each die bond configuration has been tested. Furthermore, these samples were not initially intended for investigation into curvature as a function of cycle, and had previously been subjected to thermal and inertial loading, which might have compromised results by plastically deforming the chip and/or die bond medium before the *hysteresis* and *gap drift* tests were performed.

It was shown by comparing measurements made at different times, before and after a high-G loading, that inertial forces associated with launch are sufficient to cause plastic deformation in the die bonds. Results show that in each of the three die bond configurations the reduction of curvature is greater in the loaded sample than that of the control. These measurements show the capability to make comparative measurements before and after external loading, where rigid body compensation between the two measurements is performed during post processing.

A similar test of comparative measurements is presented with the shape measurements made on components which have been stored in well controlled laboratory conditions for a time of 19 months. A reduction of the die curvature was observed, caused by stress relaxation in the gold bump bonds. This experiment, along with the

157

previous tests, show that the shape of the MEMS die is not constant, and is variable with respect to time, temperature, inertial load, and thermal cycle. Once shown that the substrate distortion is not constant, efforts have been made to determine the effects on performance this might present.

The die curvature is known to be a function of temperature, and can be controlled by thermal means. A rate table has been customized with a TEC heating element, similar to that implemented in the interferometer, to measure TFG response at various temperature states. A reduction in ZRO was observed as temperature increased, decreasing by 11% over the 80ºC temperature range. Such a change might be due to the reduction in the die curvature, suggesting that the ZRO of a component will decrease with curvature reduction by any means. Implications of the ZRO acting as a function of die curvature are that the performance characteristics of a device are affected by a storage time that is within specifications for a given design, or even by the initial launching of a device, during which high inertial loads are applied.

Also determined through the rate table testing is that the TFG gain is a function of temperature, and perhaps die curvature. The gain decreased by upwards of 25% over the 80ºC temperature range studied. The changes in performance observed during the rate table testing might be exaggerated due to the custom TFG studied. In order to make measurements without obstruction of the TFG structure, the batch studied had been fabricated without a USP. The USP allows for differential capacitance measurements, potentially reducing some effects of curvature changes.

The dynamic shape of TFG samples was monitored by adopting stroboscopic illumination and a custom script which recorded shape at various positions during the drive cycle. The measurement cycle had been recorded five times, with a measurement of the die substrate made after each operation cycle. The change in the gap distance, as determined by integration between the proof masses and the substrate, was calculated for all 95 measurements (19 positions along the operation cycle for each of the five cycles). The results of the five cycles were averaged, and plotted with standard deviations, showing that measurements possess a clear trend. In the case of the TFG-1.1.1 sample the behavior of the gap distance change was that of a quadrature error, showing changes in the gap distance of 90 nm throughout the drive cycle. Based on the measurements it was shown that approximately 50% of this gap distance change was due to out of plane motion of the proof mass. The remaining error was caused by the non-planar substrate under the proof mass and changes in tilt and shape of the proof masses during actuation.

# 8. CONCLUSIONS

All experiments presented serve to demonstrate the capabilities of the autonomous interferometric measurement system. In addition to the ability to perform scripts which are not practical for manual data acquisition, repetition of an operation is improved by reducing an element of operator error. In order to obtain sufficient data to make statistical inferences many samples need to be tested in an identical manner. This is particularly true in cases where expected changes are near the limits of the measurement system, such as with the thermal cycling experiments presented in this dissertation. Although the ability to perform the measurement was demonstrated, more samples will lead to greater certainty regarding the degree of deformation associated with thermal cycling.

Many of the capabilities presented in this dissertation are not possible using commercially available interferometric measurement systems. The ability to automate thermal cycling while performing measurements through a chamber window is unique to this system developed at WPI. Also, the measurements regarding the change in sense gap distance throughout the drive cycle of a TFG were performed following a methodology not found in open-literature, at this time.

The unique abilities of the autonomous interferometer developed act as a design tool which has enabled mechanical characterization of TFG devices as well as other MEMS and complex micro-size test articles. This has been demonstrated by exploration into the effects that die bonding has on the mechanics of a component, specifically the introduction of a curvature as a result of CTE mismatch. This curvature was shown to be

a function of temperature, time, and external loading (in the form of inertial loading or thermal cycling).

The benefits of the autonomous interferometer are not limited to the study and optimization of TFG components, but rather any MEMS device. Die bonding, as discussed in this work, might be an issue for many designs. Also, reliability of MEMS devices is able to be studied by scripting a loading cycle and monitoring the device throughout the process.

The modular architecture of the software allows for rapid implementation of additional hardware. Such hardware may be an improvement over a current component or a new feature entirely. Of those that are possible, a PZT shaker for modal analysis of components, a broadband light source for VSI measurements, or a vacuum pump for the environmental chamber. Each of these features has been implemented on prior, manually operated, interferometers at WPI. The conclusion of this work is an invaluable tool for design, characterization, and testing of MEMS devices with abilities not currently available in similar measurement systems.

This research has culminated in the development of a metrology tool which has not been available until now. The ability to autonomously record shape throughout thermal loading cycles is unique to this system at WPI. These measurements provide substantial insight into the mechanical behavior of micro-sized devices, which was not possible until this work. The software interface allows for complex measurement scripts to be developed and executed in a manner that reduces human error.

There are potential advances for the automated interferometer measurement system. The integration of a VSI procedure is possible with existing hardware. Such an implementation would allow for the characterization of multiple surfaces in a single measurement. Also, the available temperature range can be expanded, e.g., to include military specifications of -55ºC to +150ºC range, with the installation of another custom vacuum chamber. With a vacuum chamber there are less convective instabilities, enabling stable measurements at elevated temperature, as well as the removal of humidity which produces frost when temperature is set below freezing.

# 9. REFERENCES

C. Ai and J. C. Wyant, 1987, "Effect of piezoelectric transducer nonlinearity on phase shift interferometry," *Applied Optics*, 26(6):1112-1116.

J. J. Allen, 2005, *Micro Electro Mechanical System Design*, CRC Press, Boca Raton, FL, pp. 323, 331.

N. Barbour, E. Brown, J. Connelly, J. Dowdle, G. Brand, J. Nelson, and J. O'Bannon, 1998, "Micromachined inertial sensors for vehicles," *IEEE ITSC '97,* Boston, MA, pp. 1058-1063.

N. Barbour and G. Schmidt, 1999,  "Inertial sensor technology trends," *The Draper Technology Digest*, Draper Laboratory, Cambridge, MA, 3:5-13.

J. Bernstein, S. Cho, A. T. King, A. Kourepenis, P. Maciel, and M. Weinberg, 1993, "A micromachined comb-drive tuning fork rate gyroscope," *Proc. MEMS 1993*, Ft. Lauderdale, FL, pp. 143-148.

J. J. Bernstein and S. Weinberg, 1998, "Comb-drive micromechanical tuning fork gyroscope with piezoelectric readout," U.S. Patent 5,767,405.

P. Carré, 1966, "Installation et utilization du comparateur photoelectrique et interferential du Bereau International des Poids et Mesures," *Metrologia*, 2:13-23.

D. Chen and Y. Wei, 2004, "Study of non-linearity control of a piezoelectric nanoactuator*," Proc. 5$^{th}$ World Congress on Intelligent Control and Automation*, June 15-19, Hangzhou, P. R. China.

Y. Y. Cheng and J. C. Wyant, 1985, "Phase shifter calibration in phase-shifting interferometry," *Applied Optics*, 24(18):3049-3052.

S. H. Choa, 2005, "Reliability of vacuum packaged MEMS gyroscopes," *Microelectronics Reliability*, 45(2005):361-369.

K. Creath, 1991, "Phase-measurement interferometry: beware these errors," *Proc. SPIE*, 1553:213-220.

K. Creath, 1993, Chapter 4 in D. W. Robinson and G. T. Reid, *Interferogram Analysis, Digital Fringe Pattern Measurement Techniques*, Institute of Physics Publishing, Bristol, England, pp. 122-140.

Elmer, 2008, "Elmer Overview," CSC http:www.nic.funet.fi/pub/sci/physics/elmer/doc/ElmerOverview.pdf, accessed 9/1/2008.

R. Feynman, 1992, "There's plenty of room at the bottom," *J. of Microelectromechanical systems*, 1(1):61-66.

K. J. Gåsvik, 2002, *Optical Metrology 3ʳᵈ Ed.*, Wiley, W. Sussex, England, pp. 37-41, 165-167.

Gmsh, 2008, "Gmsh reference manual," http://www.geuz.org/gmsh/doc/texinfo/gmsh.pdf, accessed 9/1/2008.

D. S. Hanson, T. F. Marinis, C. Furlong, and R. J. Pryputniewicz, 2001, "Advances in optimization of MEMS inertial sensor packaging," *Proc. Internat. Congress on Experimental and Applied Mechanics in Emerging Technologies*, Portland, OR, pp. 821-825.

A. Harasaki, J. Schmit, and J. C. Wyant, 2000, "Improved vertical-scanning interferometry," *Applied Optics*, 39(13):2107-2115.

P. Hariharan, B. F. Oreb, and T. Eiju, 1987, "Digital phase-shifting interferometry: a simple error-compensating phase calculation algorithm," *Applied Optics*, 26(13):2504-2506.

R. C. Hibbeler, 2000, *Mechanics of Materials 4ᵗʰ Ed.,* Prentice Hall, Upper Saddle River, New Jersey, p 573.

Y. Hu and S. Chen, 1997, "The noise sensitivity of the Carré fringe-analysis technique," *Measurement Science and Technology*, 8:871-874.

J. W. Joo and S. H. Choa, 2007, "Deformation behavior of MEMS gyroscope sensor package subject to temperature change," *IEEE Transactions on Components and Packaging Technologies*, 30(2):346-354.

D. Karnick, G. Ballas, L. Koland, M. Secord, T. Braman, and T. Kourepenis, 2004, "Honeywell gun-hard inertial measurement unit (IMU) development," *Position Location and Navigation Symposium, PLANS 04*, 49-55.

D. King, 1989, *Design and analysis of a micromechanical tuning fork gyroscope*, MS Thesis, Massachusetts Institute of Technology, Cambridge, MA.

A. R. Klempner, R. T. Marinis, P. Hefti, and R. J. Pryputniewicz, 2006, "Scanning white light interferometry for multilevel shape measurement of MEMS," *Proc. 2006 IMAPS-NE Symp. and Expo.*, Boxboro, MA.

A. R. Klempner, 2007, *Development of a modular interferometric microscopy system for characterization of MEMS*, MS Thesis, Worcester Polytechnic Institute, Worcester, MA.

A. R. Klempner, R. T. Marinis, P. Hefti, and R. J. Pryputniewicz, 2009, "Experimental determination of the Q-factors of microcantilevers coated with thin metal films," in press: *Strain Journal*, June.

T. Kreis, 1996, *Holographic Interferometry principles and methods*, Akademie Verlag GmbH, Berlin, Germany, pp. 21-26, 123-138, 201-207.

K. J. Kuhn, 1998, *Laser Engineering*, Prentice Hall, Upper Saddle River, NJ, pp. 15-18.

R. T. Marinis, A. R. Klempner, S. P. Mizar, P. Hefti, and R. J. Pryputniewicz, 2005, "Stroboscopic illumination using LED light source," *Proc. 2005 IMAPS-NE Symp. and Expo.*, Boxboro, MA.

R. T. Marinis, A. R. Klempner, P. Heft, R. J. Pryputniewics, T. F. Marinis, J. Soucy, 2006, "Time-lapse measurements of creep in AuSn die bonds," *Mater. Res. Soc. Proc. Vol. 968*, Boston, MA.

R. T. Marinis, R. J. Pryputniewicz, T. F. Marinis, and J. W. Soucy, 2008a, "Effects of thermo compression die bond residual stress on MEMS inertial sensor," *Proc. 2008 IMAPS 41$^{st}$ annual symposium on microelectronics*, Boston, MA.

T. F. Marinis and J. W. Soucy, 2003, "Vacuum packaging of MEMS inertial sensors," *Proc. 2003 Symp. on Microelectronics*, Boston, MA, pp. 386-391.

T. F. Marinis, 2007, "The future of MEMS," *Proc. 8$^{th}$ Internat. Symp on MEMS and Nanotechnology (8$^{th}$ –ISMAN)*, Springfield, MA, pp. 1-24.

T. F. Marinis, J. W. Soucy, J. G. Lawrence, R. T. Marinis, and R. J. Pryputniewicz, 2008b, "Vacuum sealed MEMS package with an optical window," *IEEE Electronics Components and Technology Conference (ECTC)*, Orlando, FL, pp. 804-810.

Opto Diode, 2008, "High Output Red LED, OD-620L", http://www.optodiode.com/pdf/OD620L.pdf, accessed 5/2008.

R. J. Pryputniewicz, 1995, "Quantitative determination of displacements and strains from holograms," Ch. 3 in *Holographic Interferometry*, Vol. 68 in Springer Series in Sciences, Springer-Verlag, Berlin, pp.33-72.

R. J. Pryputniewics, 2008, private communication.

R. J. Pryputniewicz, T. F. Marinis, J. W. Soucy, P. Hefti, A. R. Klempner, and C. Furlong, 2003, "Novel noninvasive methodology for characterization of packaging for MEMS inertial sensors," *Proc. 2003 Symp. on Microelectronics*, Boston, MA, pp. 392-397.

T. H. Ramsey, 1975, "Metallurgical behavior of gold wire in thermal compression bonding," *Solid State Technology*, 10(1975):43-47.

J. Schwider, R. Burow, K.-E. Elssner, J. Grzanna, R. Spolaczyk, and K. Merkel, 1983, "Digital wave-front measuring interferometry: some systematic error sources," *Applied Optics*, 22(21):3421-3432.

A. Sharma, F. M. Zaman, B. V. Amini and F. Ayazi, 2004, "A high-Q in-plane SOI tuning fork gyroscope," *Proc. IEEE Sensors*, pp 467-470.

M. S. Weinberg and A. Kourepenis, 2006, "Error sources in in-plane silicon tuning fork MEMS gyroscopes," *J. of MEMS*, 15(3):479-491.

O. J. Woodman, 2007, "An introduction to inertial navigation," University of Cambridge, Technical Report Number 696.

# APPENDIX A.   DERIVATION OF THE INTERFERENCE EQUATIONS

The methodology for derivation of the interference equation is outlined by Kreis (1996).  For the electromagnetic waves investigated we are able to neglect polarizing effects (assume plane polarized) such that the general equation is

$$\frac{\partial^2 E}{\partial z^2} - \frac{1}{c^2}\left(\frac{\partial^2 E}{\partial t^2}\right) = 0 \, , \tag{A-1}$$

where $E$ is the electromagnetic wave, $z$ is the direction of propagation, $c$ is the speed of light, and $t$ is time.  Of the possible solutions to the differential equation, a simple harmonic wave is the most useful, of the form defined by Eq. 5

$$E(z,t) = E_0\cos(\phi) \, , \tag{A-2}$$

where $\phi$ is the phase term.

Application of Euler's formula,

$$e^{i\theta} = \cos\theta + i\sin\theta \, , \text{ leads to} \tag{A-3}$$

$$\cos x = Re\left\{e^{ix}\right\} = \frac{e^{ix} + e^{-ix}}{2} \, , \tag{A-4}$$

which results in

$$E(z,t) = \frac{E_0}{2}\left[e^{i\phi} + e^{-i\phi}\right]. \tag{A-5}$$

We use the notation of Eq. A-5 for ease in performing the superposition of two waves.  It is recognized that the second term is the complex conjugate of the first.  The physical wave is only the real portion of Eq. A-5, i.e.,

$$E(z,t) = \frac{E_0}{2}\left[e^{i\phi}\right]. \tag{A-6}$$

Next, we look at the observed value, intensity, referred to as $I$. The relation of intensity to the electromagnetic field is defined by the Maxwell's equations

$$I = \epsilon_0 c_0 E^2, \qquad I \sim E^2, \tag{A-7}$$

where $\epsilon_0$ is permittivity of free space and $c_0$ is the speed of light. Measuring the intensity of light is performed by averaging over a finite time as there is currently no sensor available to function at the frequency of light. This finite time would be the exposure time in the case of a digital camera. We are able to neglect proportionality constants and define the intensity as the product of the complex conjugates of the electric field,

$$I = E_0 E_0^* = |E_0|^2. \tag{A-8}$$

The case of interference is now modeled by the superposition of two electric fields with different phase positions, $\phi + \Delta\phi_1$ and $\phi + \Delta\phi_2$.

$$E_1(z,t) = E_{01} e^{i(\phi + \Delta\phi_1)}, \text{ and} \tag{A-9}$$

$$E_2(z,t) = E_{02} e^{i(\phi + \Delta\phi_2)}. \tag{A-10}$$

Substitution of Eqs A-9 and A-10 into A-8 results in

$$I(z,t) = \left[E_{01} e^{i(\phi + \Delta\phi_1)} + E_{02} e^{i(\phi + \Delta\phi_2)}\right] \times$$
$$\times \left[E_{01} e^{-i(\phi + \Delta\phi_1)} + E_{02} e^{-i(\phi + \Delta\phi_2)}\right]. \tag{A-11}$$

Expansion of Eq. A-11 leads to

$$I = E_{01}^2 + E_{02}^2 + E_{01} E_{02}\left[e^{i(\phi + \Delta\phi_1 - \Delta\phi_2)} + e^{-i(\phi + \Delta\phi_1 - \Delta\phi_2)}\right]. \tag{A-12}$$

Substitution of A-8 and A-4 into A-12 leads to a solution in terms of measurable intensities, viz.,

$$I = I_1 + I_2 + 2\sqrt{I_1 I_2}\cos(\phi + \Delta\phi_1 - \Delta\phi_2). \tag{A-13}$$

We define the background intensity ($I_b$), modulation intensity ($I_m$), and phase difference ($\Delta\phi$) as

$$I_b = I_1 + I_2, \tag{A-14}$$

$$I_m = 2\sqrt{I_1 I_2}, \text{ and} \tag{A-15}$$

$$\Delta\phi = \Delta\phi_1 - \Delta\phi_2, \tag{A-16}$$

resulting in the form

$$I = I_b + I_m \cos(\phi + \Delta\phi), \tag{A-17}$$

which is shown as Eq. 6 in the text.

# APPENDIX B.    DERIVATION OF PHASE SHIFT FORMULA

In order to solve the over defined system of equations obtained at each pixel

through phase stepping we apply a least squares technique.   We begin with the solution

for interference between two light waves, as derived in Appendix A, given by Eq. A-17

as

$$I = I_b + I_m \cos(\phi + \Delta\phi).$$
(B-1)

We can apply the cosine sum formula,

$$\cos(A + B) = \cos(A)\cos(B) - \sin(A)\sin(B),$$
(B-2)

to obtain

$$I = I_b + I_m[\cos(\phi)\cos(\Delta\phi) - \sin(\phi)\sin(\Delta\phi)].$$
(B-3)

We now make the following substitutions,

$$u = I_m \cos(\phi), and$$
(B-4)

$$v = -I_m \sin(\phi),$$
(B-5)

which when combined with Eq. B-3 results in

$$I = I_b + u\cos(\Delta\phi) + v\sin(\Delta\phi).$$
(B-6)

The sum of the quadratic errors, *S,* for *m* phase steps is found by

$$\sum_{n=1}^{m} [I_b + u\cos(\Delta\phi_n) + v\sin(\Delta\phi_n) - I_n]^2 = S.$$
(B-7)

To minimize the errors the partial derivative is taken with respect to each variable, i.e.,

$$\frac{\partial S}{\partial I_b} = 0 = \sum_{n=1}^{m} 2[I_b + u\cos(\Delta\phi_n) + v\sin(\Delta\phi_n) - I_n],$$
(B-8)

$$\frac{\partial S}{\partial u} = 0 = \sum_{n=1}^{m} 2[I_b + u\cos(\Delta\phi_n) + v\sin(\Delta\phi_n) - I_n]\cos(\Delta\phi_n), \tag{B-9}$$

$$\frac{\partial S}{\partial v} = 0 = \sum_{n=1}^{m} 2[I_b + u\cos(\Delta\phi_n) + v\sin(\Delta\phi_n) - I_n]\sin(\Delta\phi_n). \tag{B-10}$$

By performing algebra on Eqs B-8 through B-10, we obtain

$$I_b m + u \sum_{n=1}^{m} \cos(\Delta\phi_n) + v \sum_{n=1}^{m} \sin(\Delta\phi_n) = \sum_{n=1}^{m} I_n , \tag{B-11}$$

$$I_b \sum_{n=1}^{m} \cos(\Delta\phi_n) + u \sum_{n=1}^{m} \cos^2(\Delta\phi_n) +$$

$$+v \sum_{n=1}^{m} \sin(\Delta\phi_n)\cos(\Delta\phi_n) = \sum_{n=1}^{m} I_n\cos(\Delta\phi_n) , \tag{B-12}$$

$$I_b \sum_{n=1}^{m} \sin(\Delta\phi_n) + u \sum_{n=1}^{m} \sin(\Delta\phi_n)\cos(\Delta\phi_n) +$$

$$+v \sum_{n=1}^{m} \sin^2(\Delta\phi_n) = \sum_{n=1}^{m} I_n\sin(\Delta\phi_n) . \tag{B-13}$$

The system of three equations B-11 through B-13 is written in single matrix form as

$$\begin{bmatrix} m & \sum_{n=1}^{m}\cos(\Delta\phi_n) & \sum_{n=1}^{m}\sin(\Delta\phi_n) \\ \sum_{n=1}^{m}\cos(\Delta\phi_n) & \sum_{n=1}^{m}\cos^2(\Delta\Phi_n) & \sum_{n=1}^{m}\sin(\Delta\phi_n)\cos(\Delta\phi_n) \\ \sum_{n-1}^{m}\sin(\Delta\phi_n) & \sum_{n=1}^{m}\sin(\Delta\phi_n)\cos(\Delta\phi_n) & \sum_{n=1}^{m}\sin^2(\Delta\Phi_n) \end{bmatrix} \begin{Bmatrix} I_b \\ u \\ v \end{Bmatrix} = \begin{Bmatrix} \sum_{n=1}^{m}I_n \\ \sum_{n=1}^{m}I_n\cos(\Delta\phi_n) \\ \sum_{n=1}^{m}I_n\sin(\Delta\phi_n) \end{Bmatrix}. \tag{B-14}$$

To this point the number of phase steps has not been important, thus Eq. B-14 is a general

solution. However, it is possible to use Table B-1to fill in the summation totals for a

given set of phase stepped images. For the remainder of this example five phase steps

will be considered, each of magnitude 90º, starting at 0º.

Table B-1. Values for solution of 5-step algorithm.

| $n$ | $\Delta\phi_n$ | $\sin(\Delta\phi_n)$ | $\cos(\Delta\phi_n)$ | $\sin^2(\Delta\phi_n)$ | $\cos^2(\Delta\phi_n)$ | $\sin(\Delta\phi_n)\cos(\Delta\phi_n)$ |
|---|---|---|---|---|---|---|
| 1 | 0 | 0 | 1 | 0 | 1 | 0 |
| 2 | 90 | 1 | 0 | 1 | 0 | 0 |
| 3 | 180 | 0 | -1 | 0 | 1 | 0 |
| 4 | 270 | -1 | 0 | 1 | 0 | 0 |
| 5 | 360 | 0 | 1 | 0 | 1 | 0 |
| $\Sigma$ | | **0** | **1** | **2** | **3** | **0** |

When the values of Table B-1 are inserted into Eq. B-14 the resulting matrix equation is

$$\begin{bmatrix} 5 & 1 & 0 \\ 1 & 3 & 0 \\ 0 & 0 & 2 \end{bmatrix}\begin{bmatrix} I_b \\ u \\ v \end{bmatrix} = \begin{bmatrix} I_1 + I_2 + I_3 + I_4 + I_5 \\ I_1 - I_3 + I_5 \\ I_2 - I_4 \end{bmatrix}. \tag{B-15}$$

The matrix of Eq. B-15 is reduced because the $v$ term is independent of the other

solutions, thus

$$v = \frac{I_2 - I_4}{2}, and \tag{B-16}$$

$$\begin{bmatrix} 5 & 1 \\ 1 & 3 \end{bmatrix}\begin{bmatrix} I_b \\ u \end{bmatrix} = \begin{bmatrix} I_1 + I_2 + I_3 + I_4 + I_5 \\ I_1 - I_3 + I_5 \end{bmatrix}. \tag{B-17}$$

Next, we are able solve for $u$,

$$\begin{bmatrix} I_b \\ u \end{bmatrix} = \frac{1}{14}\begin{bmatrix} 3 & -1 \\ -1 & 5 \end{bmatrix}\begin{bmatrix} I_1 + I_2 + I_3 + I_4 + I_5 \\ I_1 - I_3 + I_5 \end{bmatrix}, \tag{B-18}$$

$$\begin{bmatrix} I_b \\ u \end{bmatrix} = \frac{1}{14}\begin{bmatrix} 2I_2 + 3I_2 + 4I_3 + 3I_4 + 2I_5 \\ 4I_1 - I_2 - 6I_3 - I_4 + 4I_5 \end{bmatrix}. \tag{B-19}$$

To solve for the phase term, $\phi$, we divide Eq. B-5 by B-4 to get
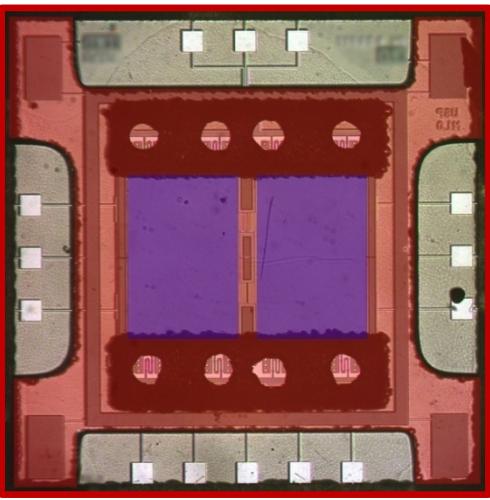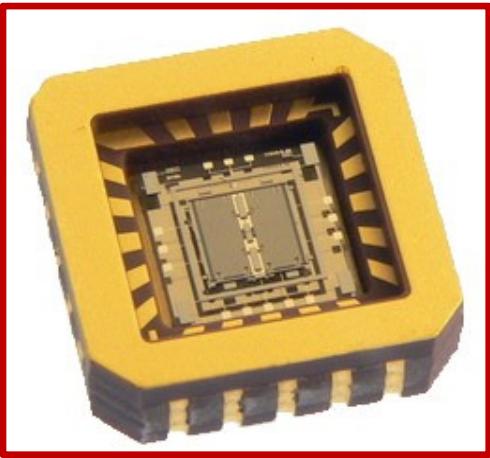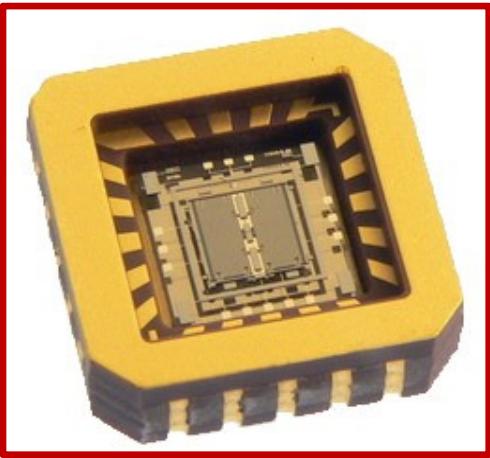
$$\phi = \tan^{-1}\left(-\frac{v}{u}\right),$$  (B-20)

which, when used in conjunction with B-16 and B-19, gives

$$\phi = \tan^{-1}\left[\frac{7(I_4 - I_2)}{4I_1 - I_2 - 6I_3 - I_4 + 4I_5}\right].$$  (B-21)

This methodology may be followed for deriving the phase term as a function of any

number of phase stepped images. Equation B-21 is included in the text as Eq. 16.

# APPENDIX C.    SAMPLE IDENTIFICATION TABLE







| | | |
|---|---|---|
| **TFG-1**<br>Live Gyro | TFG-1.1. | TFG-1.1.1 |
| | | TFG-1.1.2 |
| | | TFG-1.1.3 |
| **TFG-2.**<br>High-G | TFG-2.1.<br>(braze) | TFG-2.1.1 |
| | | TFG-2.1.2 |
| | | TFG-2.1.3 |
| | | TFG-2.1.4 |
| | | TFG-2.1.5 |
| | | TFG-2.1.6 |
| | TFG-2.2.<br>(9-bump) | TFG-2.2.1 |
| | | TFG-2.2.2 |
| | | TFG-2.2.3 |
| | | TFG-2.2.4 |
| | | TFG-2.2.5 |
| | | TFG-2.2.6 |
| | TFG-2.3.<br>(25-bump) | TFG-2.3.1 |
| | | TFG-2.3.2 |
| | | TFG-2.3.3 |
| | | TFG-2.3.4 |
| | | TFG-2.3.5 |
| | | TFG-2.3.6 |
| **TFG-3.**<br>relax test | TFG-3.1.<br>(4-bump<br>close) | TFG-3.1.1 |
| | | TFG-3.1.2 |
| | | TFG-3.1.3 |
| | TFG-3.2.<br>(4-bump<br>spread) | TFG-3.2.1 |
| | | TFG-3.2.2 |
| | | TFG-3.2.3 |

# APPENDIX D.  DYNAMIC SHAPE OF ADDITIONAL TFG-1 SAMPLES

Only a single test article (TFG-1.1.1) was presented during the text of this dissertation for the illustration of procedures developed.  The plots obtained on additional TFG samples are presented within this appendix.  All measurements have been made following an identical test and analysis procedure as that described in section 6.6.2, with the exception of the effect of temperature on dynamic shape and gap distance.

In general the results presented in this section show that the TFG-1.1.1 test article performs more uniformly, and with less out of plane motion, than the two remaining live TGF samples.  This also shows that the performance of a device might be very unique, thus generalizations into the nature of errors encountered while driving should be withheld.

The test article TFG-1.1.2 has been measured during dynamic operation, with the percent changes in tilt and curvature as a function of in-plane position shown in Figs 119-120, and the change in the sense gap as a function of the in-plane position shown in Fig. 121.  Identical analysis has been performed on TFG-1.1.3, with the percent changes in tilt and curvature as a function of in-plane position shown in Figs 112-123, and the change in the sense gap as a function of the in-plane position shown in Fig. 124.
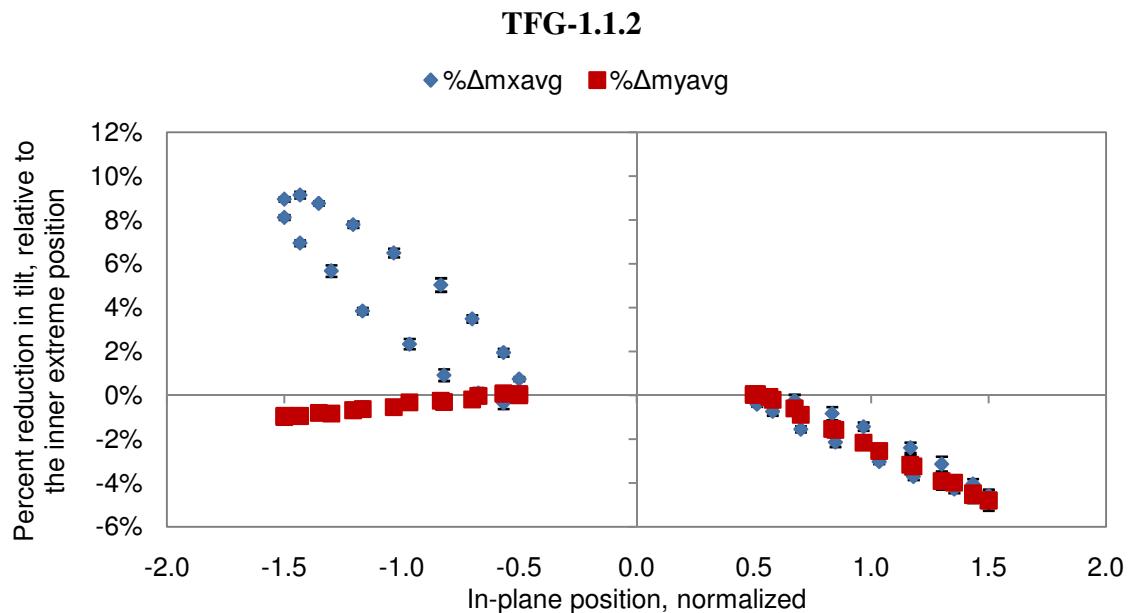
**TFG-1.1.2**



Fig. 119.  Percent change in proof mass tilt during actuation, TFG-1.1.2.
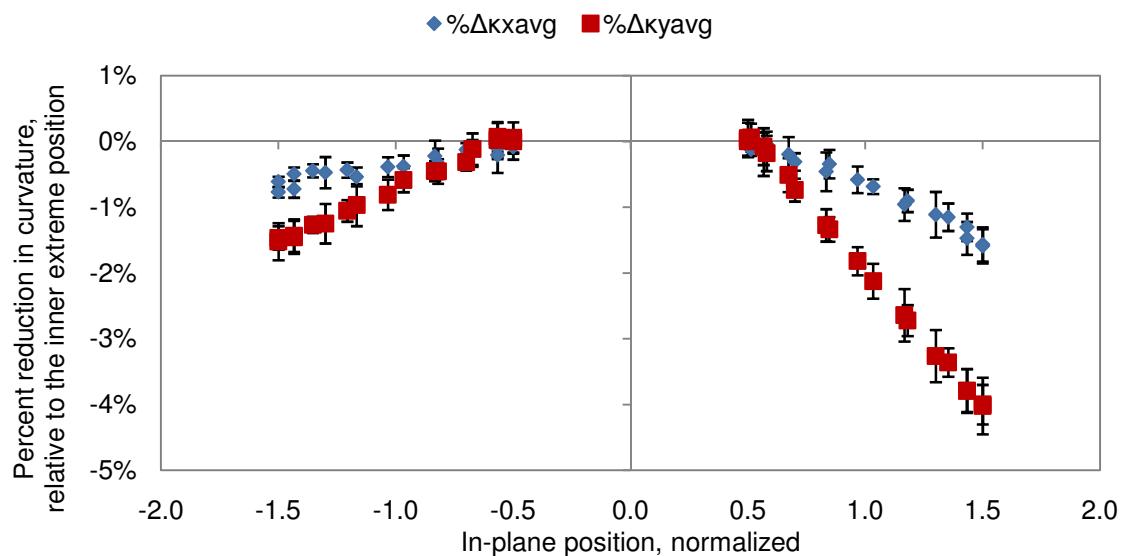


Fig. 120.  Percent change in proof mass curvature during actuation, TFG-1.1.2.
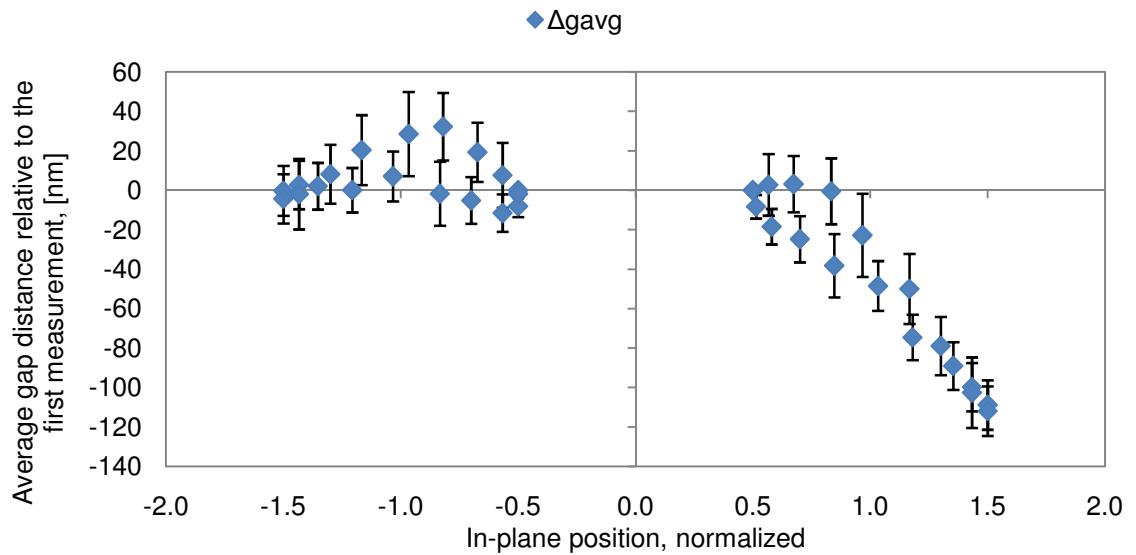
Fig. 121. Change in average gap distance calculated from surface integration TFG-1.1.2.
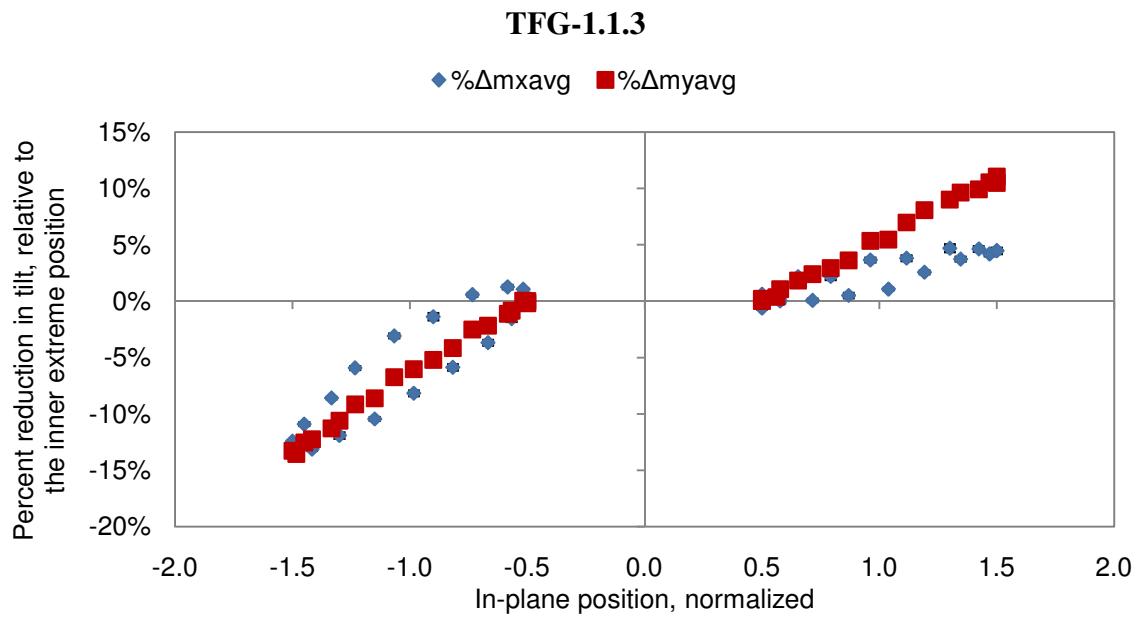
**TFG-1.1.3**



Fig. 122. Percent change in proof mass tilt during actuation, TFG-1.1.3.
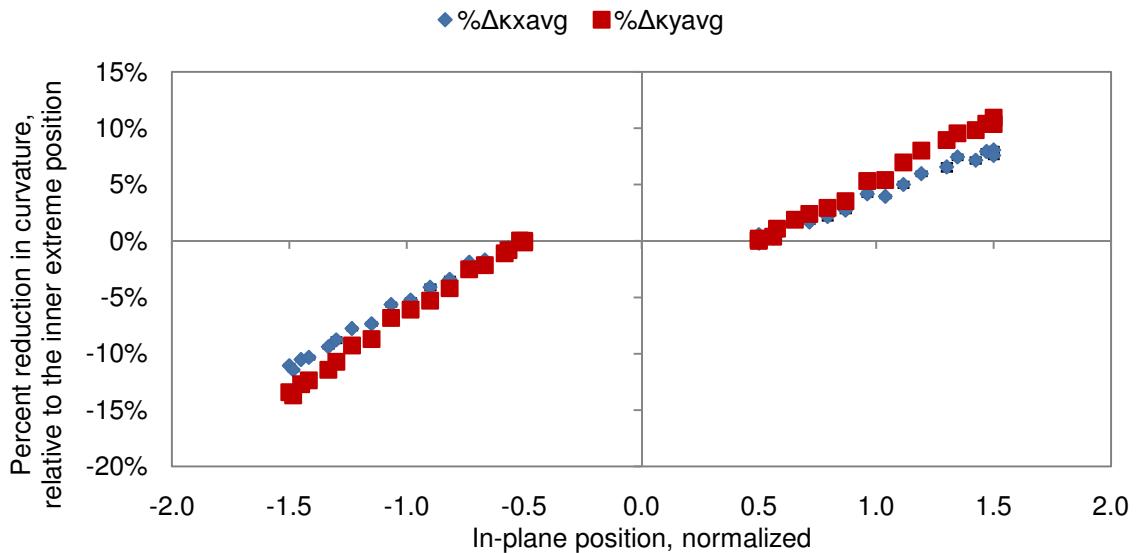
Fig. 123. Percent change in proof mass curvature during actuation, TFG-1.1.3.
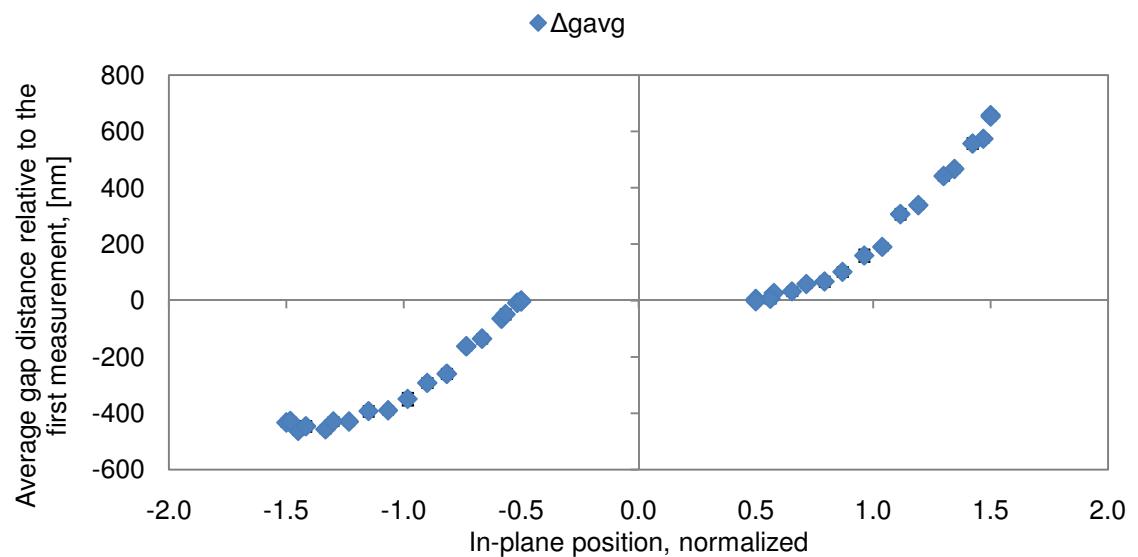


Fig. 124. Change in average gap distance calculated from surface integration TFG-1.1.3.